UNIVERSITY OF CALIFORNIA
RIVERSIDE

Anthropogenic Impacts on Air Pollution - From Primary Marine Emissions to Secondary Organic Aerosol Formation

A Dissertation submitted in partial satisfaction
of the requirements for the degree of

Doctor of Philosophy

in

Chemical and Environmental Engineering

by

Weihan Peng

September 2020

Dissertation Committee:
Dr. David R. Cocker III, Chairperson
Dr. Kelley Barsanti
Dr. Roya Bahreini

The Dissertation of Weihan Peng is approved:

Committee Chairperson

University of California, Riverside

Acknowledgements

There are many who guided, encouraged, supported and helped me through these five years graduate study. Without those individuals, I would not have accomplished so much and be able to finish this dissertation. I would like to take a moment to thank them.

I must acknowledge my advisor, Dr. David Cocker, who has been a tremendous mentor for me. Dr. Cocker led me into the atmospheric pollution research world when I was an undergraduate student and provided me the opportunity to pursue my Ph.D. degree in this field. I could not have found a better advisor, who can be more dedicated and patient to his/her students. His invaluable expertise, insightful guidance and enthusiasm has not only helped me improve on my critical thinking and problem-solving skills as a researcher and engineer but also helped me become a better person.

I would also like to thank Dr. J. Wayne Miller, who has imparted his wisdom to me in different aspects including research and career. His extensive experience and expertise on field measurements has helped me develop and improve the skills on project planning, organizing and coordinating. As an excellent communicator, he taught me how to communicate and collaborate with people from different backgrounds. In addition, his work ethics have inspired and will keep inspiring me to work hard for my career.

I would also like to acknowledge my dissertation committee, Dr. Kelley Barsanti and Dr. Roya Bahreini for the valuable feedback and suggestions on this dissertation. I would like to thank Dr. William Carter for his insightful guidance on SAPRC modelling, Dr. William Porter for the GEOS-Chem modeling and discussions, Dr. Georgios

Karavalakis for the guidance on vehicle emission research and Dr. Haofei Zhang for the AMS data analysis training.

It has been a pleasure to be a part of the chamber research team. I appreciate all the help and support from my colleagues. Special thanks to Dr. Lijie Li and Dr. Mary Kacarab for their hands-on guidance and training on chamber research during my undergraduate study and the initial stage of my Ph.D. program. I would also like to thank Dr. Weihua Li, Dr. Chia-Li (Candice) Chen, Dr. Xinze Peng, Dr. Paul Van Rooy, Dr. Patrick Roth and Dr. Jiacheng Yang for all the support and collaboration for my research projects. I am also thankful for all the assistance and help from Chen Le, Qi Li, Jia Jiang, Sahar Ghadimi, Isaac Afreh and Christos Stamatis. I would also like to thank Kurt Bumiller for the chamber maintenance support and Kathy Cocker on gas chromatography analysis support.

I must also acknowledge my collaborators, Dr. Joel Corbin, Dr. Stéphanie Gagné, Dr. Prem Lobo from National Research Council (Canada) and Dr. Steven Rogak, Una Trivanovic and Dr. Patrick Kirchen from University of British Columbia (Canada) on the marine emission campaign in Canada. It was a successful campaign and a pleasure to collaborate with them.

I would also like to thank the funding support from Coordinating Research Council, William R. Pierson/Ford Award and Colin E. Hackett Award for my Ph.D. research. Without the funding support, I would not be able to accomplish my research projects.

Last but certainly not the least, I must acknowledge my parents, Shangguan Yuanfeng and Peng Jianzhong – thank you for your unconditional love and endless support. There are no words that can express my gratitude to my mother for all the sacrifices that she has made on my behalf. She is the embodiment of the values of independence and perseverance of hard work. She has inspired and will always inspire me to work hard and stay strong under any circumstance. I would also like to thank my other family members for their emotional support and my friends in the US and China for all the fun times.

The text of chapter 2 of this dissertation, in full, is a reprint of the material as is appearing in Peng et al. (Environ. Pollut., doi.org/10.1016/j.envpol.2020.115404, 2020).

ABSTRACT OF THE DISSERTATION

Anthropogenic Impacts on Air Pollution - From Primary Marine Emissions to Secondary Organic Aerosol Formation

by

Weihan Peng

Doctor of Philosophy, Graduate Program in Chemical and Environmental Engineering
University of California, Riverside, September 2020
Dr. David R. Cocker III, Chairperson

Anthropogenic air pollution consists of primary and secondary pollutants resulted from human activities. It is related to different environmental and health issues such as climate change, visibility and respiratory diseases.

The maritime transport is an important source of anthropogenic primary air pollution. Natural gas (NG) vessels have become more widely used due to the more stringent emission regulations; however, emission data from NG maritime operations is still limited. This thesis conducted a comprehensive analysis on the air quality, health effects and climate change impacts of switching from diesel to NG. Results showed that $PM_{2.5}$, NO_x, CO_2 were reduced by about 93%, 92% and 18%, respectively. However, HCHO and CH_4 increased several-fold. A health risk assessment showed the diesel plume increased long-term health risk and the NG plume increased short-term health risk. A global warming potential (GWP) analysis was performed and revealed that the average NG exhaust GWP was increased by 38%. Mitigation strategies for further reducing pollutants

from NG exhaust are discussed and showed potential for reducing short-term health and climate impacts.

Anthropogenic secondary organic aerosol (SOA) is formed from the oxidation of volatile organic compounds (VOCs) such as aromatics and is critically impacted by NO_x. Global transport models use the SOA parameters from the two major chemical pathways, RO_2+NO and RO_2+HO_2 and the branching ratio of RO_2+NO pathway (β), to predict SOA formation. This thesis improved the model prediction by experimentally investigating the SOA formation from those pathways with a novel approach of maintaining β constant throughout chamber experiments. At low-NO_x conditions, multiple SOA yield curves were observed. The yield increased with HO_2/RO_2, indicating the contribution of RO_2+RO_2 pathway. The GEOS-Chem model showed that for the regions with high aromatic emissions but lower HO_2/RO_2, aromatic SOA was overestimated by up to 100%. At high-NO_x conditions, SOA parameters were developed when controlling β at one during the chamber experiments to simulate the RO_2+NO pathway without significant contribution from the other pathways. The global surface β was modelled using GEOS-Chem and four β scenarios were observed. SOA formation was investigated when simulating the daytime β profiles for those scenarios.

Table of Contents

List of Tables

List of Figures

Chapter 1 : Introduction

1.1 Introduction

Air pollution is a major global issue that is detrimental to human health and the environment. The different types of air pollutants are the major sources that cause adverse impacts on air quality, human health, climate change and atmospheric visibility (Comer et al., 2018; Giechaskiel et al., 2014; Jimenez et al., 2009; Pope III, 2002). The ambient and household air pollution was estimated to cause about seven million premature deaths every year according to the World Health Organization. The ambient air pollution alone was estimated to contribute to about 8% of all deaths in 2016 (WHO, 2016). Anthropogenic air pollution refers to air pollutants from human-activities, specifically, particulate matter (PM), nitrogen oxides (NO_x), sulfur oxides (SO_x), carbon dioxide (CO_2), carbon monoxide (CO) from fossil fuel combustion for power plants or transportation and methane (CH_4) and hydrogen sulfide (H_2S) from agricultural activities.

Air pollutants are often categorized into primary and secondary pollutants. Primary pollutants are those directly emitted into the atmosphere from emission sources such as engine combustion in vehicles or marine vessels. Secondary pollutants, on the other hand, are those formed in the atmosphere from the chemical reactions of volatile organic compounds (VOC) suspended in the atmosphere.

Maritime transport is an important source for primary pollutant. The International Maritime Organization data shows maritime transport emits 940 million tonnes of CO_2 and is responsible for about 2.5% of global greenhouse gases (GHG) (IMO, 2015). It was also

estimated that the emissions of NO_x and SO_x from maritime transport around Europe would be equal or larger than the total emission from stationary and land-based mobile sources by 2020 (Komar and Lalić, 2015). As new environmental regulations are mandating cleaner fuels and lower emissions from all maritime operations, natural gas (NG) became the fuel that enabled mariners to meet regulations. However, emission data from maritime operations using natural gas is limited. As the number of natural gas vessels and NG refueling infrastructures is increasing (Burel et al., 2013; Le Fevre, 2018; Pavlenko et al., 2020; Sharafian et al., 2019), it is necessary to have a comprehensive understanding on the environmental impacts of switching from traditional marine fuels to natural gas and is also important to provide guidance on mitigation measures for NG vessels owners.

Organic aerosol (OA) accounts for up to 90% of global sub-micro aerosol budget (Jimenez et al., 2009). Secondary organic aerosol (SOA), as an important category of secondary pollutants, is formed through VOC oxidation initiated by hydroxyl radical (OH), nitrate radical (NO_3) or ozone (O_3) in the atmosphere. SOA comprises about 70% of OA (Hallquist et al., 2009; Tsigaridis and Kanakidou, 2003) in atmosphere. It was found that SOA from aromatic compounds, which are the major anthropogenic SOA precursors, accounted for 50% to 70% of SOA in urban areas. Studies suggested the SOA from anthropogenic VOCs more important than previous reported (Farina et al., 2010; Henze et al., 2010), raising the interests of further investigations on the anthropogenic SOA formation mechanisms.

SOA yield (Y) is a measure of the amount of SOA formation from consuming a certain amount of the precursor hydrocarbons, represented by **Equation 1.1** where ΔM_o

is the formed SOA mass and ΔHC is the consumed hydrocarbon (Odum et al., 1996a, 1997). A gas/particle absorptive partitioning model was developed to represent the SOA formation (Odum et al., 1996b). The absorption equilibrium constant ($K_{om,i}$) is defined as **Equation 1.2**, where $A_{i,om}$ is the concentration of compound i in absorbing organic material (particle) phase (ng/m^3), G_i is the concentration of compound i in gas phase (ng/m^3), M_o is the concentration of total absorbing organic aerosol (μg/m^3), R is the ideal gas constant (8.206×10^{-5} m^3 atm mol^{-1} K^{-1}), T is the temperature (K), MW_{om} is the average molecular weight of organic material (g/mol), ξ_i is the activity coefficient of compound *i* in organic material phase and $p^o_{L,i}$ is the saturation liquid vapor pressure (torr) of compound *i*. Combing the SOA yield and gas/particle partitioning, it was derived that SOA yield could be calculated by **Equation 1.3**, where α_i is the mass-based stoichiometric coefficient of product *i* formed (Odum et al., 1997, 1996b).

$$Y = \frac{\Delta M_o}{\Delta HC} \qquad \textbf{Equation 1.1}$$

$$K_{om,i} = \frac{A_{i,om}}{G_i * M_o} = \frac{760 * R * T}{MW_{om} * 10^6 * \xi_i * p^o_{L,i}} \qquad \textbf{Equation 1.2}$$

$$Y = M_o \sum\left(\frac{\alpha_i K_{om,i}}{1 + K_{om,i} M_o}\right) \qquad \textbf{Equation 1.3}$$

Different models have been developed and used based on the gas/particle partitioning theory to estimate the gas- and particle- distribution of a mixture of products formed from SOA precursors. A two-product model was developed by assuming there are two types of semi-volatile products that partition to the absorbing organic material

phase formed from SOA precursors (Odum et al., 1996a). The parameters of α_1, $K_{om,1}$, α_2 and $K_{om,2}$ were used to represent the stoichiometric coefficient and absorption equilibrium constant of those two types of products. Later on, a volatility-basis set (VBS) framework was developed by categorizing the semi-volatile products into a wide range of products represented by the effective saturation pressure of each product (C^*) (Donahue et al., 2006). The concentration of condensed-phase organic materials C_{OA} (ug/m^3) can be calculated using **Equation 1.4** and **1.5**, where C_i is the total concentration of product i, C_i^* is the effective saturation pressure of product i and α_i is the mass-based stoichiometric coefficient of product *i*. A basis set of parameters α_i with the corresponding C^* were used to represent the products and their gas-particle partitioning from a certain SOA precursor.

$$C_{OA} = \sum_i C_i * \left(1 + \frac{C_i^*}{C_{OA}}\right)^{-1} \qquad \textbf{Equation 1.4}$$

$$C_i = \alpha_i * \Delta HC \qquad \textbf{Equation 1.5}$$

Different parameters such as NO_x level, temperature and relative humidity impact the anthropogenic SOA formation (Cocker et al., 2001b; Ng et al., 2007; Song et al., 2005; Svendby et al., 2008). It was shown that SOA formation from photo-oxidation of aromatic compounds was highly dependent on NO_x, one of the major anthropogenic emissions in atmosphere. Higher SOA yield was observed in lower NO_x conditions and lower SOA yield was observed in higher NO_x conditions (Henze et al., 2010; Li et al., 2015; Ng et al., 2007; Song et al., 2005). In order to understand the impacts of NO_x on aromatic SOA formation, different indicators have been used for different NO_x conditions in previous studies. Song *et al*. observed two SOA yield trends from *m*-xylene from

experiments with different ratios of initial hydrocarbon (HC) to NO_x (higher yield when $HC/NO_x > 8$ and lower yield when $HC/NO_x < 5.5$). Ng *et al*. simulated high- and low-NO_x conditions in chamber with the injection of HONO and H_2O_2, respectively, then reported SOA yield parameters from aromatics using two-product model. It was suggested that the more volatile products such as $RONO_2$ (organic nitrates) of RO_2+NO and the less volatile products such as ROOH (organic hydroperoxides) of RO_2+HO_2 be related with SOA yield trend at high- and low-NO_x conditions, respectively (Kroll and Seinfeld, 2008). The ratio of [NO] to [HO_2] was used as the indicator of NO_x conditions and proposed that aromatic compounds have higher SOA yield in the areas with lower [NO]/[HO_2] (Henze et al., 2010). However, the branching ratio of RO_2+NO pathway compared with RO_2+HO_2 pathway explicitly represents the contribution of each pathway resulted from NO_x and should be used to represent the NO_x conditions (Presto and Donahue, 2006; Pye et al., 2010). The branching ratio of RO_2+NO pathway (β) is represented with **Equation 1.6**, where k_{RO_2+NO} and $k_{RO_2+HO_2}$ are the reaction constants of RO_2 with NO and HO_2, respectively.

$$\beta = \frac{k_{RO_2+NO}[NO]}{k_{RO_2+HO_2}[HO_2]+k_{RO_2+NO}[NO]} \qquad \textbf{Equation 1.6}$$

Current global transport models such as GEOS-Chem and CMAQ use β coupled with SOA yield parameters (GEOS-Chem: VBS; CMAQ: two-product model) from RO_2+NO and RO_2+HO_2 pathways to predict global SOA concentrations. A large range of global anthropogenic SOA (0.05 to 9.7 Tg/yr) prediction was reported (Farina et al., 2010; Guillaume et al., 2007; Tsigaridis and Kanakidou, 2003), indicating the importance of

investigating what drives the large difference on model predictions and the contribution those SOA yield parameters to the prediction uncertainties. The SOA yield parameters for RO_2+NO and RO_2+HO_2 pathways were obtained from high- and low-NO_x chamber experiments, which were represented by different NO_x indicators as discussed earlier. Those traditional high-NO_x experiments where the initial HC/NO_x was below 5.5 or HONO was used may not accurately simulate the RO_2+NO pathway when β is equal to 1. Similarly, traditional low-NO_x may not represent RO_2+HO_2 pathway. The branching ratio β needs to be evaluated in those experiments to verify the accuracy of the obtained SOA yield parameters. The ratio also needs to be controlled constantly at an intermediate β value (0 to 1) to better represent the SOA formation from RO_2+ HO_2 and RO_2+ NO pathways, respectively.

This thesis is seeking to expand the understanding of the release and formation of anthropogenic air pollution and its environmental impacts from primary marine vessel emissions to secondary organic aerosol formation from anthropogenic VOC emissions. The comprehensive impact analysis of switching a marine vessel from diesel to natural gas was conducted by field emission measurements of a marine vessel with a dual-fuel engine. The test matrix was designed considering different engine loads, fuels and combustion optimization methods. The corresponding data and analysis were provided. The other important goal of this thesis is to expand the understanding of SOA formation under the influences of NO_x. While the SOA parameters of RO_2+ HO_2 and RO_2+ NO pathways are normally derived from chamber experiments, more parameters need to be considered. Three SOA yield curves were observed from *m*-xylene at low NO_x

conditions, but the SOA parameters currently used in global transport models can only represent one of those yield curves. The ratio of HO_2/RO_2 increased SOA yield, indicating the contribution of RO_2+RO_2 pathway with the lower SOA forming potential compared with the RO_2+HO_2 pathway. In addition, a novel approach of investigating the NO_x impacts on SOA formation was developed by keeping the branching ratio (β) of the RO_2+ NO pathway constant in chamber. Using this approach constrains the contribution of RO_2+ NO pathway with a constant and known fraction during the course of a chamber experiment, compared with the traditional experiments where the branching ratio changes drastically. Two SOA yield curves were observed from *m*-xylene when β was controlled at 1. A higher SOA yield curve where less NO was injected while still maintaining β at 1 suggests the auto-oxidation of RO_2. The SOA formation at constant intermediate β was characterized in the first time. While it was generally believed that the SOA parameters at an intermediate β could be extrapolated linearly from the parameters at β=0 and β=1, experimental data suggested that the linear extrapolation might not accurately represent the SOA condition for an intermediate β and they needed to be obtained from chamber experiments.

Chapter 2 presents the comprehensive analysis of the impacts of switching a marine vessel from a traditional diesel fuel to natural gas, in the aspects of air quality, health risks and climate change, for the first time. Criteria pollutants such as NO_x, SO_x and CO, PM (including black carbon, elemental carbon and organic carbon), greenhouse gases such as CO_2 and CH_4 and a toxic gas, formaldehyde (HCHO), were measured when the vessels engine was operated at the engine load from idling to 90% and powered with

diesel or NG. The routine activity of the engine on the vessel was obtained to calculate the overall activity-weighted emission factors, coupled with the modal emission data. It was found that $PM_{2.5}$, BC, NO_x, CO_2 were decreased by 93%, 97%, 92% and 20%, respectively, however, increased CO and HCHO by >4 and >6 times and CH_4 to >11 g/kWh. In order to estimate the overall impact of the emission changes, a worst-case scenario health risk assessment and global warming potential (GWP) analysis were conducted for the diesel and NG emissions. The switch to NG reduces the cancer risk and long-term health effects due to the large PM reduction but significantly increases the shorter-term health risks due to the HCHO increase. The engine-activity weighted average GWP on a 100-year basis (GWP100) from engine emissions was increased by 38% when switching from diesel to NG, however, it was comparable for both fuels for the scenarios when engine was operated at >70% load. Three mitigation measures were proposed and analyzed and suggested the potential of much lower health risks and comparable GWP when switching diesel to NG with appropriate mitigate measures.

Chapter 3 discusses the driving forces of the large variance of SOA formation from *m*-xylene at low NO_x conditions while current chemical transport models such as GEOS-Chem and CMAQ use a constant SOA yield to represent SOA formation potential from aromatic compounds at low NO_x conditions. A strong dependence of SOA potential on HO_2/RO_2 ratio was observed: SOA formation potential increases with the HO_2/RO_2 ratio when the ratio is smaller, then it levels off when the ratio increases to a certain level. Three different SOA yield curves were observed at different HO_2/RO_2 conditions and the HO_2/RO_2-dependent volatility basis set (VBS) parameters were developed. The

RO_2+RO_2 pathway was found to be important at low NO_x and low HO_2/RO_2 conditions and it shows a lower SOA forming potential compared to the RO_2+HO_2 pathway. A series of SOA experiments, with the addition of a reactive organic gas (ROG) surrogate mixture to represent the atmosphere in urban conditions showed the measured SOA was consistent with the lowest HO_2/RO_2 yield curve generated in this work. As H_2O_2 and SOA precursor are popularly used for very low NO_x SOA studies, it is recommended to control the initial aromatic and H_2O_2 ratio, thus controlling the HO_2/RO_2 ratio for chamber experiment design. A global surface HO_2/RO_2 ratio dataset obtained from GEOS-Chem showed lower HO_2/RO_2 ratios in regions such as east coast of America, east China and India with more human activities and more aromatic emissions. The SOA formation from *m*-xylene in such regions could be overestimated by up to 100%, indicating an overestimation of SOA form other aromatic compounds and possibly biogenic compounds depending on the volatility of RO_2+RO_2 pathway products. The effects of light intensity and NO_x off-gassing from chamber wall were also investigated and found not significant on affecting aromatic SOA potential at low NO_x conditions.

Chapter 4 evaluates the *m*-xylene SOA formation at high-NO_x conditions when the branching ratio (β) was controlled at ~1 or other constant intermediate values between 0 and 1. A novel approach was developed to control β at a relative constant value by continuously injecting NO with customized injection rates. A constant β during chamber experiment simulates the SOA formation from RO_2+NO pathway without the significant contribution from other pathways and enables the development of SOA parameters of RO_2+NO pathway. When maintaining β at ~1, multiple SOA yield curves were observed

and the runs of β = ~1 with higher NO injection rates showed lower yields. This is consistent with the NO impacts on RO_2 auto-oxidation observed in atmosphere that existence of NO reduces the extent of RO_2 auto-oxidation. When NO is sufficient (β = ~1), less highly oxygenated RO_2 from auto-oxidation is expected with more NO present, leading to less heavy products and lower SOA formation. Since β is an important indicator of NO_x conditions, the global surface β was modelled using GEOS-Chem and four β scenarios were observed. The global β during daytime is relatively constant. The SOA formation potential at constant intermediate β which represent each global surface β scenario was also investigated. It was shown that the current approach of estimating SOA yield parameters for intermediate β might not be accurate as the measured SOA yield was lower than those from the linear extrapolation between the two pathways (β=0 and β=1). Those parameters at intermediate β need to be obtained experimentally to be used in global transport models.

Reference

Burel, F., Taccani, R., Zuliani, N., 2013. Improving sustainability of maritime transport through utilization of Liquefied Natural Gas (LNG) for propulsion. Energy 57, 412–420. https://doi.org/10.1016/j.energy.2013.05.002

Cocker, D.R., Mader, B.T., Kalberer, M., Flagan, R.C., Seinfeld, J.H., 2001. The effect of water on gas-particle partitioning of secondary organic aerosol: II. m-xylene and 1,3,5-trimethylbenzene photooxidation systems. Atmos. Environ. 35, 6073–6085. https://doi.org/10.1016/S1352-2310(01)00405-8

Comer, A.B., Chen, C., Rutherford, D., 2018. Relating short-term measures to IMO's minimum 2050 emissions reduction target. https://www.theicct.org/sites/default/files/publications/IMO_Short_term_potential_20181011.pdf, INTERNATIONAL COUNCIL ON CLEAN TRANSPORTATION.

Donahue, N.M., Robinson, A.L., Stanier, C.O., Pandis, S.N., 2006. Coupled partitioning, dilution, and chemical aging of semivolatile organics. Environ. Sci. Technol. 40, 2635–2643. https://doi.org/10.1021/es052297c

Farina, S.C., Adams, P.J., Pandis, S.N., 2010. Modeling global secondary organic aerosol formation and processing with the volatility basis set: Implications for anthropogenic secondary organic aerosol. J. Geophys. Res. Atmos. 115. https://doi.org/10.1029/2009JD013046

Giechaskiel, B., Maricq, M., Ntziachristos, L., Dardiotis, C., Wang, X., Axmann, H., Bergmann, A., Schindler, W., 2014. Review of motor vehicle particulate emissions sampling and measurement: From smoke and filter mass to particle number. J. Aerosol Sci. 67, 48–86. https://doi.org/10.1016/j.jaerosci.2013.09.003

Guillaume, B., Liousse, C., Rosset, R., Cachier, H., Van Velthoven, P., Bessagnet, B., Poisson, N., 2007. ORISAM-TM4: A new global sectional multi-component aerosol model including SOA formation - Focus on carbonaceous BC and OC aerosols, in: Tellus, Series B: Chemical and Physical Meteorology. https://doi.org/10.1111/j.1600-0889.2006.00246.x

Hallquist, M., Wenger, J.C., Baltensperger, U., Rudich, Y., Simpson, D., Claeys, M., Dommen, J., Donahue, N.M., George, C., Goldstein, A.H., Hamilton, J.F., Herrmann, H., Hoffmann, T., Iinuma, Y., Jang, M., Jenkin, M.E., Jimenez, J.L., Kiendler-Scharr, A., Maenhaut, W., McFiggans, G., Mentel, T.F., Monod, A., Prévôt, A.S.H.H., Seinfeld, J.H., Surratt, J.D., Szmigielski, R., Wildt, J., 2009. The formation, properties and impact of secondary organic aerosol: Current and emerging issues. Atmos. Chem. Phys. 9, 5155–5236. https://doi.org/10.5194/acp-9-5155-2009

Henze, D.K., Fu, T.-M., Jacob, D.J., Heald, C.L., Ng, N.L., Seinfeld, J.H., Kroll, J.H., 2010. Global modeling of secondary organic aerosol formation from aromatic hydrocarbons: high- vs low-yield pathways. Atmos. Chem. Phys. Discuss. 7, 14569–14601. https://doi.org/10.5194/acpd-7-14569-2007

IMO, 2015. Third IMO Greenhouse Gas Study 2014, Smith, Tristan & P. Jalkanen, J & A. Anderson, B & Corbett, James & Faber, J & Hanayama, S & O'Keeffe, E & Parker, S & Johansson, Lasse & Aldous, L & Raucci, Carlo & Traut, Michael & Ettinger, S & Nelissen, D & Lee, David & Ng, S & Agrawal, A & Winebrake,.

Jimenez, J.L., Canagaratna, M.R., Donahue, N.M., Prevot, A.S.H.H., Zhang, Q., Kroll, J.H., DeCarlo, P.F., Allan, J.D., Coe, H., Ng, N.L., Aiken, A.C., Docherty, K.S., Ulbrich, I.M., Grieshop, A.P., Robinson, A.L., Duplissy, J., Smith, J.D., Wilson, K.R., Lanz, V.A., Hueglin, C., Sun, Y.L., Tian, J., Laaksonen, A., Raatikainen, T., Rautiainen, J., Vaattovaara, P., Ehn, M., Kulmala, M., Tomlinson, J.M., Collins, D.R., Cubison, M.J., Dunlea, J., Huffman, J.A., Onasch, T.B., Alfarra, M.R., Williams, P.I., Bower, K., Kondo, Y., Schneider, J., Drewnick, F., Borrmann, S., Weimer, S., Demerjian, K., Salcedo, D., Cottrell, L., Griffin, R., Takami, A., Miyoshi, T., Hatakeyama, S., Shimono, A., Sun, J.Y., Zhang, Y.M., Dzepina, K., Kimmel, J.R., Sueper, D., Jayne, J.T., Herndon, S.C., Trimborn, A.M., Williams, L.R., Wood, E.C., Middlebrook, A.M., Kolb, C.E., Baltensperger, U., Worsnop, D.R., Dunlea, E.J., Huffman, J.A., Onasch, T.B., Alfarra, M.R., Williams, P.I., Bower, K., Kondo, Y., Schneider, J., Drewnick, F., Borrmann, S., Weimer, S., Demerjian, K., Salcedo, D., Cottrell, L., Griffin, R., Takami, A., Miyoshi, T., Hatakeyama, S., Shimono, A., Sun, J.Y., Zhang, Y.M., Dzepina, K., Kimmel, J.R., Sueper, D., Jayne, J.T., Herndon, S.C., Trimborn, A.M., Williams, L.R., Wood, E.C., Middlebrook, A.M., Kolb, C.E., Baltensperger, U., Worsnop, D.R., 2009. Evolution of Organic Aerosols in the Atmosphere. Science (80-.). 326, 1525–1529. https://doi.org/10.1126/science.1180353

Komar, I., Lalić, B., 2015. Sea Transport Air Pollution, in: Current Air Quality Issues. InTech. https://doi.org/10.5772/59720

Kroll, J.H., Seinfeld, J.H., 2008. Chemistry of secondary organic aerosol: Formation and evolution of low-volatility organics in the atmosphere. Atmos. Environ. 42, 3593–3624. https://doi.org/10.1016/j.atmosenv.2008.01.003

Le Fevre, C., 2018. A review of demand prospects for LNG as a marine transport fuel. Oxford, United Kingdom. https://doi.org/10.26889/9781784671143

Li, L., Tang, P., Cocker, D.R., 2015. Instantaneous nitric oxide effect on secondary organic aerosol formation from m-xylene photooxidation. Atmos. Environ. 119, 144–155. https://doi.org/10.1016/j.atmosenv.2015.08.010

Ng, N.L., Kroll, J.H., Chan, A.W.H., Chhabra, P.S., Flagan, R., Seinfeld, J.H., 2007. Secondary organic aerosol formation from m-xylene, toluene, and benzene. Atmos. Chem. Phys. 7, 3909–3922. https://doi.org/10.5194/acp-7-3909-2007

Odum, J.R., Hoffmann, T., Bowman, F., Collins, D., Flagan, R.C., Seinfeld, J.H., 1996a. Gas/particle partitioning and secondary organic aerosol yields. Environ. Sci. Technol. https://doi.org/10.1021/es950943+

Odum, J.R., Hoffmann, T., Bowman, F., Collins, D., Flagan, R.C., Seinfeld, J.H., 1996b. Gas/particle partitioning and secondary organic aerosol yields. Environ. Sci. Technol. 30, 2580–2585. https://doi.org/10.1021/es950943+

Odum, J.R., Jungkamp, T.P.W., Griffin, R.J., Forstner, H.J.L., Flagan, R.C., Seinfeld, J.H., Aromatics, 1997. Aromatics, Reformulated Gasoline, and Atmospheric Organic Aerosol Formation. Environ.Sci.Technol. 31, 1890. https://doi.org/10.1021/es960535l

Pavlenko, N., Comer, B., Zhou, Y., Clark, N., Rutherford, D., 2020. The climate implications of using LNG as a marine fuel. https://theicct.org/sites/default/files/publications/Climate_implications_LNG_marinefuel_01282020.pdf, ICCT Working Paper 2020-02.

Pope III, C.A., 2002. Lung Cancer, Cardiopulmonary Mortality, and Long-term Exposure to Fine Particulate Air Pollution. JAMA. https://doi.org/10.1001/jama.287.9.1132

Presto, A.A., Donahue, N.M., 2006. Investigation of α-pinene + ozone secondary organic aerosol formation at low total aerosol mass. Environ. Sci. Technol. 40, 3536–3543. https://doi.org/10.1021/es052203z

Pye, H.O.T., Chan, A.W.H., Barkley, M.P., Seinfeld, J.H., 2010. Global modeling of organic aerosol: The importance of reactive nitrogen (NOx and NO3). Atmos. Chem. Phys. 10, 11261–11276. https://doi.org/10.5194/acp-10-11261-2010

Sharafian, A., Blomerus, P., Mérida, W., 2019. Natural gas as a ship fuel: Assessment of greenhouse gas and air pollutant reduction potential. Energy Policy 131, 332–346. https://doi.org/10.1016/j.enpol.2019.05.015

Song, C., Na, K., Cocker, D.R., 2005. Impact of the hydrocarbon to NOx ratio on secondary organic aerosol formation. Environ. Sci. Technol. 39, 3143–3149. https://doi.org/10.1021/es0493244

Svendby, T.M., Lazaridis, M., Tørseth, K., 2008. Temperature dependent secondary organic aerosol formation from terpenes and aromatics. J. Atmos. Chem. 59, 25–46. https://doi.org/10.1007/s10874-007-9093-7

Thomson, H., Corbett, J.J., Winebrake, J.J., 2015. Natural gas as a marine fuel. Energy Policy 87, 153–167. https://doi.org/10.1016/j.enpol.2015.08.027

Tsigaridis, K., Kanakidou, M., 2003. Global modelling of secondary organic aerosol in the troposphere: A sensitivity analysis. Atmos. Chem. Phys. Discuss. https://doi.org/10.5194/acpd-3-2879-2003

WHO, 2016. Air Pollution [WWW Document]. URL https://www.who.int/health-topics/air-pollution#tab=tab_1

Chapter 2 : Comprehensive Analysis of the Air Quality Impacts of Switching a Marine Vessel from Diesel Fuel to Natural Gas

2.1 Introduction

The global seaborne trade accounts for 80% volume of international trade and is continually growing (UNCTAD, 2019). This activity results in air pollution both at sea and in coastal regions. Emissions from shipping were estimated to be responsible for 14% nitric oxides (NO_x), 16% sulfur oxides (SO_x) and 5% particulate matter ($PM_{2.5}$) in coastal areas (European Environment Agency, 2013) and leading to environmental, health and climate impacts (Corbett et al., 2007; Huang et al., 2018; Liu et al., 2016; Matthias et al., 2010; Monteiro et al., 2018; Sharafian et al., 2019). It was estimated that around 60,000 cardiopulmonary and lung cancer deaths were caused by ship PM emissions every year and predicted that mortalities would increase by 40% from 2007 to 2012 (Corbett et al., 2007). Greenhouse gases (GHGs) such as CO_2 and CH_4, and aerosols from shipping emissions also play an important role in climate change (Lashof and Ahuja, 1990). Without increasingly stringent controls on emissions, marine-transport pollutants will lead to further degradation of air quality and human health, and exacerbation of global warming.

In order to control and limit emissions from marine vessels, the International Convention for the Prevention of Pollution from Ships (MARPOL) was adopted at the International Maritime Organization (IMO) to set emission standards and designate sulfur emission control areas (ECAs) where marine vessels must operate on fuels with sulfur content limited to 0.1%. Various control options are being used by marine vessel operators

to meet the increasingly stringent standards, including exhaust aftertreatment technologies, or switching to cleaner fuels such as natural gas (Anderson et al., 2015; Khan et al., 2012).

Natural gas (NG) is widely used in trucks and buses due to its availability and often lower cost and lower emissions of $PM_{2.5}$ and NO_x (Ayala et al., 2002; Yang et al., 2013). However, NG only represented less than 3% of global shipping fuel through 2013 to 2015 (Olmer et al., 2017). The major challenge has been the lack of NG refueling infrastructure and the associated costs. Now with many vessels on order, larger scale facilities are being built (Thomson et al., 2015), thus creating availability of NG refueling at a lower cost. The number of NG-fueled vessels in operation has grown from 34 in 2013 to 121 in 2018, with 135 vessels under construction in addition to more than 400 LNG carriers that are largely fueled by natural gas. This growth has been driven by orders placed for vessels such as cruise ships, containers and oil tankers, and was estimated to reach to about 600 in 2021. (Burel et al., 2013; Le Fevre, 2018; Pavlenko et al., 2020; Sharafian et al., 2019; Thomson et al., 2015).

There are limited measurement data on emissions from NG fueled marine engines. To the best of our knowledge, only one study previously reported on-board measurements of particle and gaseous emissions from an NG powered ship (Anderson et al., 2015). Anderson *et al*. shows that NG combustion in a marine engine results in a significant decrease in PM, particle number (PN), NO_x and CO_2 emissions, and increase in total hydrocarbon, CH_4 and CO emissions. However, the overall environmental, climate and health impacts require further investigation. Further, the paper does not report the major incomplete combustion product formaldehyde (HCHO). HCHO is defined as a

carcinogenic substance (International Agency for Research and Cancer (IARC)) and contributes to other severe health effects, including asthma and nasopharyngeal cancer (Krzyzanowski et al., 1990; McGwin et al., 2010; Nielsen and Wolkoff, 2010; Zhang et al., 2018). In addition, HCHO contributes to photochemical smog and ground-level ozone in atmosphere (Finlayson-Pitts and Pitts, 2000) which are also related to adverse health effects. Earlier results with on-road vehicles showed an increase in formaldehyde (HCHO) from NG (Ayala et al., 2003, 2002; Hesterberg et al., 2008), however, no carbonyl data from NG marine vessels has been reported thus far.

Given the limited number of reports comparing on-board marine-engine emissions from diesel and NG fuels, this study aims to provide a comprehensive analysis of the comparative emissions of criteria pollutants (NO_x, CO, SO_2, $PM_{2.5}$ mass, elemental carbon (EC) and organic carbon (OC)), greenhouse pollutants (CO_2, CH_4, black carbon (BC)) and toxic air pollutant (HCHO) from a large modern commercial vessel operating at sea during normal revenue service in the Vancouver, BC, Canada area in April 2018. In particular, combining the measured real-world dual-fuel engine activity or E2 cycle from ISO 8178 and modal emissions, this study provides an assessment on the impacts on local air quality, human health risks and global climate change when switching from diesel to NG. This chapter discussed trade-offs in health risks for lower PM with increased HCHO and the effect on the global climate when BC and CO_2 emissions are decreased but CH_4 emissions are increased.

2.2 Materials and Methods

2.2.1 Test Platform: Vessel and Propulsion System

The 6,750-deadweight-tonnage (DWT) test vessel was the first LNG-battery hybrid roll-on/roll-off (RO/RO) cargo ferry operating in North America. The heart of the propulsion system was the twin NG-diesel dual fuel engines coupled to constant-speed generators. The engines employ direct injection of liquid fuel and indirect injection of NG fuel. The 4-stroke, 9-cylinder, turbocharged dual-fuel engines have a maximum power output and speed of 4,320 kW and 720 rpm, respectively and can be operated in either NG or diesel mode. In NG mode, the diesel pilot fuel supplies less than 10% of the total fuel energy at 10% engine load and much less at higher loads (1% at 75% load).

2.2.2 Engine Operating Conditions

Emissions were measured while the vessel operated as closely as possible to the four certification loads specified in the ISO 8178 E2 cycle (International Organization for Standardization, 1996). Measurements at the certification loads allowed a check of the performance of this engine compared to certification values. Some deviation from the E2 cycle loads occurred as the vessel had to maintain published schedules. Operating at 100% was impractical hence the highest load was 90%. In addition to measurements at the four E2 cycle modes, tests were carried out at idle where the vessel spent considerable time during the loading and unloading of cargo. Usually idle emissions are not discussed in most studies because this type of operation is avoided; however, it is relevant to coastal vessel

operations and is considered here. One to three repeat measurements at the same loads were carried out when possible.

The vessel used liquefied natural gas (LNG) with 92% mole fraction of methane. The boil-off gas was routed to engine and burned in the gas mode. The fuel used in diesel mode or as pilot fuel in gas mode was a regular Canadian on-road use ultra-low sulfur diesel fuel (ULSD) with <15 ppm sulfur. The typical fuel used by this specific engine was NG. The vessel was first tested on NG and then on diesel.

2.2.3 Emission Measurements

The emission measurements were conducted following ISO 8178-2 protocol (International Organization for Standardization, 1996). A summary of test points is shown in **Table 2.1**. The exhaust was sampled from a partial flow venturi dilution system as described by Agrawal *et al*. (Agrawal et al., 2008). A key feature in the experimental design was for all diagnostic instruments to measure from the same dilution tunnel during the campaign to eliminate dilution ratio as a variable for instrument comparison.

The exhaust emissions were measured using various gaseous- and particulate-, on-line and off-line instruments (**Figure 2.1**). For gas-phase species, a HORIBA portable gas analyzer (PG-350) was used to measure NO_x, CO and CO_2 with and a J.U.M. total hydrocarbon analyzer HFID 3-200 with 100 ppb detection limit, was used for total hydrocarbon (THC) and methane (CH_4) measurement. FID and PG350 were sampling from either dilution tunnel or exhaust, alternately, controlled by a three-way valve. 2,4 - Dinitrophenylhydrazine (DNPH) coated silica cartridges (Waters Corp., Milford, MA)

were used to collect carbonyl gases with a critical flow orifice restricting flow at 1 LPM. Sampled cartridges were extracted using acetonitrile and injected into an Agilent high performance liquid chromatograph (HPLC) equipped with a diode array detector and a variable wavelength detector. For the particle-phase, real-time black carbon concentrations were measured by an AVL 483 Micro Soot Sensor. The PM sample collection was conducted by passing samples through Pall Gellman Teflon and 2500 QAT-UP Tissuquartz (quartz) Pall 47 mm filters at a flow rate of 15 LPM. Teflon filters were weighted to quantify PM mass and quartz filters were analyzed by Sunset Laboratory OCEC carbon aerosol analyzer model 3 with NIOSH 5040 method to quantify elemental carbon (EC) and organic carbon (OC) (Ashley et al., 2017; Bautista et al., 2014).

2.2.4 Data Analysis

The exhaust flow rate was calculated with the differential pressure measurements of static pressure (tube facing away from the flow) and stagnation pressure (tube facing the flow) as well as the stack temperature, following EPA Method 2 (United States Environmental Protection Agency, 2011). There are three major sources of the uncertainties of this method: probe coefficient, temperature and differential pressure measurements (Bryant et al., 2014). The type-S Pitot tube used in this study was calibrated annually to assure the accuracy of probe coefficient. At each test point, pressure and temperature measurements were averaged from three replicated measurements to minimize the measurement error. The less than 10% uncertainties flow measurement were observed when engine was at idle and 2% to 7% at other engine loads

while a few studies shows a less than 5% flow measurement uncertainties (Bryant et al., 2014; Johnson et al., 2016). An excellent agreement (**Figure 2.2**) was observed when comparing with measured exhaust flowrate with those from manufacturer manual and calculated with carbon balance method (only data at 50%, 75% and 100% engine load were available) (WÄRTSILÄ Engines, 2016).

The modal emission factors (g/kWh) of each species at each engine load were calculated with concentration (g/m^3), exhaust flow rate (m^3/hr) and engine power (kW) using **Equation 2.1** where EF_i is the emission factors of species i in g/kWh, $c_{i,j}$ is the concentration of species i at engine load j in g/m^3, $\dot{V}_j$ is the exhaust volumetric flowrate at engine load j in m^3/hr and P_j is the power measured at engine load j. In order to avoid instrument drift from invalidating the measurement results, a drift correction was applied by applying drift correction factors obtained from the instruments response to reference zero and span gases before and after each test interval, following guidelines from CFR 1065.672 drift correction (United States Environmental Protection Agency, 2010).

$$\mathrm{EF_i} = \frac{\mathrm{c_{i,j}} \times \dot{\mathrm{V}}_\mathrm{j}}{\mathrm{P_j}} \qquad \textbf{Equation 2.1}$$

Real-world activity profiles of the vessel were collected for two weeks of routine operation from the vessel on-board control and data acquisition software and categorized into 0-25%, 25-50%, 50-75% and 75-100% engine load ranges. The engine modal activity was used as weighting factor to calculate average weighted emission factors using **Equation 2.2** where EF_{WM} is the weighted mass emission level (CO, CO_2, $PM_{2.5}$, NO_x, etc.) in g/kWh, g_i is the emission rate in g/hr, P_i is the power measured during each mode

in kWh and WF_i is the weighting factor (the fraction of time that a vessel operates at, or close to, the corresponding engine load). Average weighted emission factors were also calculated with certification weighting factors specified in ISO 8178- E2 cycle as comparison.

$$EF_{WM} = \frac{\sum_{i=1}^{i=n}(g_i \times WF_i)}{\sum_{i=1}^{i=n}(P_i \times WF_i)} \quad \textbf{Equation 2.2}$$

A health risk assessment of exhaust emissions for diesel and NG combustion was conducted following the guidelines from California Office of Environmental Health Hazard Assessment (OEHHA) and South Coast Air Quality Management District (SCAQMD) (California Office of Environmental Health Hazard Assessment, 2015; South Coast Air Quality Management District, 2017) for specifying operational and compliance requirements for a stationary air pollutant source by considering hazard identification, exposure assessment, dose-response assessment and risk characterization. Emission factors when a vessel is at berth and assuming Gaussian dispersion from a stationary stack were used. The health risk assessment uses a complex model and the calculated health indices are highly dependent on the meteorological location and target population of the emissions. However, our study focuses on the impact of switching from diesel to NG; thus, the relative change of health index from diesel to NG exhaust was calculated, which allows the elimination of effects from meteorological and population factors. The carcinogenic and non-carcinogenic, acute and chronic health risks, including maximum individual cancer risk (MICR), chronic hazard index (HIC), 8-hr chronic hazard index (HIC8) as well as acute hazard index (HIA) were calculated. HIC, HIC8 and HIA indicate the cumulative

health impacts from multiple substances on the target organ in the long term, 8-hr exposure and short term, respectively.

The cancer risk (MICR) was calculated with the pollutant concentration, exposure factor and unit cancer potency of the pollutant. The concentration was calculated from emission rate and χ/Q factor which is obtained from a pre-calculated table using Gaussian dispersion model with input parameters including stack height, downwind distance and other meteorological location parameters such as wind speed, terrain and surrounding land use (South Coast Air Quality Management District, 2017). The exposure factor represents the exposure situation of the target population, considering the age distribution, daily breathing rate, exposure frequency and duration, etc. This factor is also obtained from SCAQMD health risk assessment package. Cancer potency is a pollutant-dependent factor.

As explained in the previous section, the health impacts relative differences from NG exhaust to diesel exhaust were calculated. Exposure factor is a product of combined exposure factor, worker adjustment factor and multi-pathway adjustment factor (MP) (**Equation 2.6**). The first two terms are not pollutant-dependent, and MP is 1 for both formaldehyde and PM because inhalation is the only major cancer-related pathway for formaldehyde and PM, therefore the exposure factor is the same for both NG and diesel exhaust. In the concentration term, only the emission rate depends on the pollutants and χ/Q and MWAF are the same for both NG and diesel exhaust (**Equation 2.4**). Only emission rate and cancer potency, MP and MWAF (**Table 2.2**) are pollutant-dependent,

and MP and MWAF are 1 for both PM and formaldehyde, thus only emission rate and cancer potency are needed to calculate the relative difference of MICR (**Equation 2.9**).

$$\text{MICR} = \text{Concentration} \times \text{Exposure Factor} \times \text{Cancer Potency (CP)} \times 10^{-6}$$

Equation 2.3

$$\text{Concentration} = \text{GCL} = \text{Q}_{\text{tpy}} \times {}^{\chi}/_{\text{Q}} \times \text{MWAF}$$ **Equation 2.4**

$$\text{Q}_{\text{tpy}} = \text{EF} * \text{Power}$$ **Equation 2.5**

$$\text{Exposure Factor} = \text{CEF} \times \text{MP} \times \text{WAF}$$ **Equation 2.6**

$$\text{MICR} = \text{EF} * \text{Power} \times {}^{\chi}/_{\text{Q}} \times \text{MWAF} \times \text{CEF} \times \text{MP} \times \text{WAF} \times \text{Cancer Potency (CP)} \times 10^{-6}$$

Equation 2.7

$$\text{MICR}_{\text{fuel}} = \text{MICR}_{\text{HCHO}} + \text{MICR}_{\text{PM}} = (\text{EF}_{\text{HCHO}} \times \text{CP}_{\text{HCHO}} \times \text{MWAF}_{\text{HCHO}} \times \text{MP}_{\text{HCHO}} + \text{EF}_{\text{PM}} \times \text{CP}_{\text{PM}} \times \text{MWAF}_{\text{PM}} \times \text{MP}_{\text{PM}}) \times \text{Power} \times {}^{\chi}/_{\text{Q}} \times \text{CEF} \times \text{WAF} \times 10^{-6}$$

Equation 2.8

$$\text{MICR}_{\%} = \frac{\text{MICR}_{\text{NG}} - \text{MICR}_{\text{Diesel}}}{\text{MICR}_{\text{Diesel}}}$$

$$= \frac{(\text{EF}_{\text{NG}_{\text{HCHO}}} \times \text{CP}_{\text{NG}_{\text{HCHO}}} + \text{EF}_{\text{NG}_{\text{PM}}} \times \text{CP}_{\text{NG}_{\text{PM}}}) - (\text{EF}_{\text{Diesel}_{\text{HCHO}}} \times \text{CP}_{\text{Diesel}_{\text{HCHO}}} + \text{EF}_{\text{Diesel}_{\text{PM}}} \times \text{CP}_{\text{Diesel}_{\text{PM}}})}{\text{EF}_{\text{Diesel}_{\text{HCHO}}} \times \text{CP}_{\text{Diesel}_{\text{HCHO}}} + \text{EF}_{\text{Diesel}_{\text{PM}}} \times \text{CP}_{\text{Diesel}_{\text{PM}}}}$$

Equation 2.9

For the above equations (**Equation 2.3 – 2.9**), CP is the cancer potency $(\text{mg/kg-day})^{-1}$ of a compound, GLC is the ground level concentration (ug/m^3), Q_{tpy} is the emission rate

(tons/yr), EF is the emission factor (g/kWh), Power is the annual power usage (kW/year), MWAF is the molecular weight adjustment factor (used to correct metal amount from compounds with various elements along with toxic metal atom. 1 for both PM and formaldehyde), 10^{-6} is the unit conversion factor, CEF is the combined exposure factor (target-population-dependent), MP is the cancer multi-pathway factor (1 for both PM and formaldehyde), WAF is worker adjustment factor (target-population-dependent), χ/Q is the concentration at a receptor distance/Emission rate [(ug/m^3)/(tons/yr)] (location-dependent) and exposure factor is the exposure situation for target population to a pollutant.

Cumulative effects of formaldehyde and PM on all affected organ systems (**Table 2.3**) are considered when calculating the chronic, 8-hour-chronic and acute health indices. Similar to MICR, the relative difference of HIC, HIC8, HIA were calculated using **Equation 2.11**, **2.13** and **2.15**, respectively.

$$\text{Total HIC}_{\text{target organ}} = \{[Q_{tpy} \times (\chi/Q) \times MP_{TAC1} \times MWAF]/\text{Chronic REL}_{TAC1}\}_{\text{target organ}} + \{[Q_{tpy} \times (\chi/Q) \times MP_{TAC2} \times MWAF]/\text{Chronic REL}_{TAC2}\}_{\text{target organ}} \quad \textbf{Equation 2.10}$$

$$HIC_{\%} = (HIC_{NG} - HIC_{Diesel}) / HIC_{diesel} = \frac{\{EF_{NG_{HCHO}} / \text{Chronic REL}_{HCHO} + EF_{NG_{PM}} / \text{Chronic REL}_{PM}\}_{respiratory} - \{EF_{Diesel_{HCHO}} / \text{Chronic REL}_{HCHO} + EF_{Diesel_{PM}} / \text{Chronic REL}_{PM}\}_{respiratory}}{\{EF_{Diesel_{HCHO}} / \text{Chronic REL}_{HCHO} + EF_{Diesel_{PM}} / \text{Chronic REL}_{PM}\}_{respiratory}}$$

Equation 2.11

$$\text{Total HIC8}_{\text{target organ}} = \{[Q_{tpy} \times (\chi/Q) \times WAF \times MWAF]/8 - \text{Hour REL}_{TAC1}\}_{\text{target organ}} + \{[Q_{tpy} \times (\chi/Q) \times WAF \times MWAF]/8 - \text{Hour REL}_{TAC2}\}_{\text{target organ}} \quad \textbf{Equation 2.12}$$

$$HIC8_{\%} = (HIC8_{NG} - HIC8_{Diesel}) / HIC8_{diesel} = \frac{\{EF_{NG_{HCHO}} / 8hr\text{-}REL_{HCHO}\}_{respiratory} - \{EF_{Diesel_{HCHO}} / 8hr\text{-}REL_{HCHO}\}_{respiratory}}{\{EF_{Diesel_{HCHO}} / 8hr\text{-}REL_{HCHO}\}_{respiratory}}$$ **Equation 2.13**

$$\text{Total } HIA_{target\ organ} = \{[Q_{tpy} \times (\chi/Q) \times MWAF]/\text{Acute } REL_{TAC1}\}_{target\ organ} + \{[Q_{tpy} \times (\chi/Q) \times MWAF]/\text{Acute } REL_{TAC2}\}_{target\ organ}$$ **Equation 2.14**

$$HIA_{\%} = (HIA_{NG} - HIA_{Diesel}) / HIA_{diesel} = \frac{\{EF_{NG_{HCHO}} / \text{Acute } REL_{HCHO}\}_{eye} - \{EF_{Diesel_{HCHO}} / \text{Acute } REL_{HCHO}\}_{eye}}{\{EF_{Diesel_{HCHO}} / \text{Acute } REL_{HCHO}\}_{eye}}$$

Equation 2.15

For the above equations (**Equation 2.10 – 2.15**), MP is chronic multi-pathway factor (1 for both formaldehyde and PM), REL is reference exposure level (ug/m^3) and TAC is toxic air contaminant (1: $PM_{2.5}$ and 2: formaldehyde).

The GWP for 20- and for 100-years were calculated: for CH_4, the GWP (CO_2 equivalent g/kWh) of 84 and 34 were used (Myhre et al., 2013) and for BC, the GWP of 3200 and 900 were used (Bond et al., 2013), respectively. Global temperature change potential (GTP) (Shine et al., 2005), indicating the potential of global surface temperature change, is also calculated using the values **Table 2.4** and the average emission factors of CO_2, CH_4 and black carbon.

2.3 Results and Discussion

2.3.1 Real-world Engine Activity

To accurately calculate the emission contribution to an air mass, it is essential to know both the emissions at each engine load and the fraction of time that the vessel operates at the corresponding load. A concern in applying the weighting factors of ISO 8178 E2

Cycle (International Organization for Standardization, 1996) is that this vessel operated in harbor service; not the open sea. The actual ship weighting factors (**Table 2.5**) are significantly different from the standard E2 weighting factors due to the fraction of time when engine was at idle.

2.3.2 Modal and Weighted Average Emission Rates and Factors

The modal emission rates (g/hr) and emission factors (g/kWh) for NO_x, CO_2, HCHO, CO, CH_4, total hydrocarbon (THC) and $PM_{2.5}$ as well as BC, EC and OC emissions at five engine modes are shown in **Table 2.5**. Measurement uncertainties were analyzed by considering duplicate measurement of exhaust flow, sample measurement and instrument uncertainties (Farrance and Frenkel, 2012).

The average weighted emissions factors (EF) are listed in **Table 2.5-b** for both real-world operation and standard E2 cycle. Although **Table 2.5-a** showed that the percentage of time at each load was significantly different for these two cycles, the average weighted emission factors for most pollutants were similar. However, EF_{THC} and EF_{CH_4} calculated from the E2 cycle were about 40% lower than those calculated from the actual vessel activity due to the high emissions at idle where the vessel spent 32% of operation time. Unless specified, the average weighted emission factors discussed here were calculated from the real-world cycle of this vessel. The switch from diesel to NG resulted in reductions in NO_x, $PM_{2.5}$, BC, OC and CO_2 by 92%, 93%, 97%, 92% and 18%, respectively, along with increases in CO and HCHO by 424% and 615%, respectively. An average methane

emission factor of 11.5 g/kWh was measured when the engine was in NG mode, while it was under limit of detection (< 0.002 g/kWh) in diesel mode.

The EF_{NO_x} for diesel was 9.6 ± 0.3 g/kWh, similar to the IMO Tier II certification value (9.7 g/kWh) and for NG was 0.76 ± 0.02g/kWh, much lower than the Tier III standard (2.4 g/kWh) (Shallcross et al., 2012). The reductions of both NO_x and $PM_{2.5}$ provide immediate benefit in terms of air quality in non-attainment areas if a significant number of harbor craft and ocean-going vessels switched to NG. The EF_{CO_2} for NG was 521 ± 10 g/kWh, with an 18% reduction compared to diesel. This reduction shows the potential of reducing global CO_2 emission inventory from shipping, while still far from the IMO CO_2 reduction goal of 70% by 2050 (Comer et al., 2018). The greatest reductions of NO_x (92-94%) and CO_2 (20-24%) were observed at >50% loads (**Figure 2.3**), where more than half of engine operating time was spent. However, these emissions reduction benefits must be considered together with the HCHO and CH_4 emissions of NG, as discussed below.

Simultaneously observed with reduced NO_x and $PM_{2.5}$ were increased levels of CO, HCHO and CH_4. The higher emission factors of two major incomplete combustion products, CO and HCHO, are believed to be caused by imperfect flame propagation in uneven-temperature regions of combustion chamber from NG engines (CIMAC, 2014; Liu et al., 2013). EF_{CO} and EF_{HCHO} increased from 0.67 ± 0.01 g/kWh and 34 ± 2 mg/kWh to 3.5 ± 0.1 g/kWh and 244 ± 24 mg/kWh, respectively when switching from diesel to NG. This observation is consistent with earlier results for on-road applications for NG (Ayala et al., 2003, 2002). With respect to modal emission factors (**Figure 2.3**), the CO and HCHO emissions for both NG and diesel modes becomes smaller as engine load increases but are

still considerably higher in NG mode. With a similar trend to CO, HCHO modal emission factor data show more variability, which is caused by the more complex sampling and analysis process for HCHO (chemical capture followed by transport to a laboratory for analysis) (Delgado et al., 2008; Sebaei et al., 2018).

Between 10^3 and 10^4 ppm of methane was measured from NG exhaust for engine loads from 90% to idle loads. This slip of unburned NG fuel is characteristic of pre-mixed natural gas combustion systems and results from similar sources as that for CO and HCHO. It was calculated a coefficient of determination of 99% and 98% (**Figure 2.4**) between HCHO, CH_4 and CO concentrations at all test points, suggesting that these three incomplete combustion products share similar origins, unlike other emissions (**Table 2.6**). Near-zero methane emissions (<100 ppb) were detected from diesel exhaust since diesel contains no methane. Unlike the emission factor profiles of NO_x, CO_2 and $PM_{2.5}$ where EF is higher at idle and decreases and stabilizes at >20% engine load, EF_{CH_4} decreases as engine load increases and combustion becomes less lean. This is due to an improved flame propagation with reduced excess air in combustion, leading to less unburnt methane emitted (Sommer et al., 2019; Woodyard, 2009). This observation indicates a potential for limiting CH_4 and other incomplete combustion products (CO and HCHO) from NG exhaust by advanced combustion techniques.

The average weighted emission factors of the $PM_{2.5}$ mass, EC and OC are shown in **Figure 2.5**. The gravimetric PM mass measurements show a good agreement with OC/EC results. The results show that OC is about and 80% of the mass emitted from diesel fuel and 95% with NG and the lubrication oil has been argued as the major source of the

OC in NG exhaust (Anderson et al., 2015; Corbin et al., 2020). The average weighted $EF_{PM_{2.5}}$ from NG is 13.5 ± 0.6 mg/kWh, 93% lower than that from diesel and well under the 100 mg/kWh Tier 4 emission standards for non-road engines. Comparing these results with a previous study (Anderson et al., 2015) shows that their $PM_{2.5}$ emission factors in NG mode from a different model of dual-fuel engine with maximum output of 7600 kW, were 1-2 orders of magnitude lower that those presented here. This difference can be explained by the difference between the engines and the approach used to measure $PM_{2.5}$ mass. This study used a standard $PM_{2.5}$ gravimetric analysis method (United States Environmental Protection Agency, 1998) and an Engine Exhaust Particle Sizer (EEPS) was used in the other study (Anderson et al., 2015) to measure particle number and $PM_{2.5}$ mass was calculated with particle size distribution and an assumed effective density. As stated by those authors and discussed previously (Corbin et al., 2020; Trivanovic et al., 2019), this approach is of limited accuracy. It was noted that the trends in $PM_{2.5}$ characteristics with load agree between the two studies. In addition, (Lehtoranta et al., 2019) reported a PM emission factor of ~20 mg/kWh for a smaller marine engine (1.4 MW output) powered by NG, which is consistent with the $PM_{2.5}$ emission factor measured in this study.

2.3.3 Health Risks of Exhaust

Exhaust from internal combustion engines contains constituents that can harm human health and for that reason, pollutant levels in exhausts are regulated. For example, when burning NG, HCHO is the primary concern, therefore the US Environmental Protection Agency (EPA) has a HCHO exhaust limit for clean-fuel fleet for heavy duty engines of 0.067 g/kWh (United States Environmental Protection Agency, 1994) and the

Occupational Safety and Health Administration (OSHA) established an 8-hour maximum permissible exposure level (PEL) for HCHO (OSHA, 2003) for workers. Furthermore, IARC has classified diesel $PM_{2.5}$ as a carcinogen (Hesterberg et al., 2012; Nielsen and Wolkoff, 2010) resulting in limits on engine exhaust concentrations of $PM_{2.5}$ becoming more stringent. Both pollutants are carcinogenic and linked with a number of health effects related to eyes, skin, lung and other human organ systems (Krzyzanowski et al., 1990; Lin et al., 2018; Nielsen and Wolkoff, 2010; Pope et al., 2002).

Assessing health issues for both fuels over the whole voyage of a vessel is complex given that for a considerable portion of time, the vessel is stationary at berth and near communities. Ship emissions at harbor have a significant impact on local pollutants level and subsequent health impacts (Alastuey et al., 2007; Xiao et al., 2018). Therefore, the comparative analysis of local health risks for both fuels was limited to the time when the vessel was stationary and at-berth as that is when personal exposure would be the highest. When the vessel was at-berth, the engines operated at <10% load. At low loads, fuel combustion efficiency is the poorest and emissions of partial oxidation products like PM and HCHO are the highest as evidenced in the modal data from this study (**Table 2.5-b**). The health risk assessment results in **Table 2.6** show the maximum individual cancer risk (MICR) and chronic non-carcinogenic health index are reduced by 92% and 35%, respectively when switching from diesel to NG, due to the PM reduction. However, when the non-carcinogenic shorter-term health risks were estimated, the acute hazard index (HIA) and 8-hr chronic hazard index (HIC8) increased more than 6-fold with NG due to increased HCHO levels. A difference not captured in the risk analysis is that though

diluted, the aged diesel PM will remain in the atmosphere for a few days to a few weeks (Seinfeld, 2015). However, the lifetime of HCHO in atmosphere is only a few hours (Miller et al., 2008; Pamler et al., 2003) during daytime due to the reactions with OH radicals and photolysis in atmosphere, causing it to both dilute and get consumed.

2.3.4 Health Risk Mitigation/Control Strategies

Given that harmful constituents are emitted in the engine exhaust from burning either NG or diesel, the original vessel design included mitigation/control measures to ensure that the exhaust plume was diluted before reaching public areas. For this vessel, the engineering control technology used a tall stack to move the hot, high-velocity plume away from the vessel, and reduce concentration and exposure in public areas. This chapter discuss three mitigation strategies: 1) use of shore power at berth; 2) cylinder-deactivation; and 3) oxidation catalysts.

Following the measurements reported here, the vessel operator decided to use shore power while at-berth to eliminate the emissions from the internal combustion engines, thus eliminating the health risks associated with exhaust emissions.

For facilities where shore power is not an option, changing the engine operation, such as the use of cylinder deactivation, which improves fuel economy and reduces emissions by deactivating the fuel injection to a sub-set of cylinders (Kutlar et al., 2005; Vos et al., 2019), will reduce formaldehyde emissions at idle. During this study, the manufacturer reprogramming reduced CO by 30% and 44% respectively when two and three cylinders were deactivated at idle (**Figure 2.6**). While no HCHO measurements were

performed during cylinder deactivation, it was assumed the same reduction (44%) according to the correlation between CO and HCHO. With the HCHO reduction from cylinder deactivation technology, it was estimated that between NG and diesel, the reduction of the longer-term health risks such as MICR and HIC from NG would increase to 93% and 61%, respectively, and the shorter-term risks such as HIC8 and HIA would reduce from 6-fold to 3-fold (**Table 2.7**).

The use of an oxidation catalyst has been employed as a control measure to reduce HCHO emissions from NG engines. While there is no available data on the oxidation catalyst HCHO removal efficiency of emissions from a marine vessel, one study reported a 95% reduction of HCHO on NG buses with oxidation catalyst under different drive conditions and another study on NG engines (2 to 5 MW) with similar power to this study, found 40% to 95% HCHO removal efficiency with oxidation catalysts from various manufacturers. (Ayala et al., 2003; Kristensen, 2007). While the removal efficiency depends on the manufacturers and catalyst operation time, it was assumed the maximum of reported value range (95%) HCHO removal to investigate the largest health benefit potential of using NG as a marine fuel. The health risk assessment estimated that, with catalyst installed on exhaust, all four health risk indexes from NG exhaust were 63% to 94% lower compared to diesel exhaust (**Table 2.7**). This indicates the potential of short-term health benefits from NG when HCHO is properly controlled in the exhaust.

2.3.5 Climate Impacts

In addition to the local and regional impacts of switching from diesel to NG, there are global climate impacts associated with an increase in CH_4 emissions and the reduction of CO_2 and BC emissions from shipping. These impacts result from the direct and indirect effects of radiative forcing (Chung and Seinfeld, 2002; Lashof and Ahuja, 1990) in the atmosphere for the long-term climate pollutant, CO_2, and the short-lived climate pollutants, CH_4 and BC. Although the atmospheric lifetime of black carbon is about 5-8 days (Cape et al., 2012), its climate effects may persist after deposition onto surfaces such as ice and snow (Bond et al., 2013) as the deposited BC continues to absorb solar radiation by changing the albedo of highly reflective and white surfaces. Bond *et al*. suggested a CO_2 equivalent global warming potential (GWP) – the amount of CO_2 equivalent climate forcing – for BC based on total climate forcing of 3200 for 20 years and 900 for 100 years with high uncertainties of -90%, +100% due to the large difficulties in BC lifetime and distribution estimation (Bond et al., 2013). Using these GWPs, it was found that the BC GWP was reduced by 97% by switching from diesel fuel to NG. Such a reduction would make a significant difference for vessels sailing near snow or ice-covered surfaces, such as in the Arctic (Gong et al., 2018). It should be emphasized that the climate impacts of BC are more complex than GWP alone may capture (Bond et al., 2013).

Methane emissions are also of concern since their warming potential is many times that of CO_2. To describe the climate effects of methane emissions, this chapter again use the GWP (IPCC, 2007), which is widely accepted for comparing the impact

from greenhouse pollutant emissions relative to CO_2. The detailed exhaust-pollutant-based GWP modal analysis using values from **Table 2.4**, for both diesel fuel and NG at 20- and 100-years, are presented in **Figure 2.7**. The GWP is greatest for both NG and diesel at idle with the GWP of NG being a factor of 7 that of diesel over 20 years (GWP20), and a factor of 4.8 over 100 years (GWP100), with the difference being largely attributable to the additional CH_4 emissions of the NG mode.

The additional GWP from CH_4 emissions largely outweighs the expected GWP benefit from the 18% reduction in CO_2 emissions from NG. While CH_4 accounts for the greatest fraction of GWP at lower engine loads, its contribution decreases significantly as engine load increases. The modal data shows that at loads above 75%, the GWP of NG exhaust is largely reduced. It is only 1.5 times that of diesel at 20-years, and the two fuels are equivalent at 100-years. The analysis shows the importance of NG emissions on GWP and the need to reduce the time spent at low engine loads, especially at idle.

The average GWP20 (**Figure 2.7**) from NG exhaust is 1515 CO_2 equivalent g/kWh, about 109% higher than that from diesel exhaust, 725 CO_2 equivalent g/kWh. Due to the shorter lifetime of CH_4 in the atmosphere (Myhre et al., 2013) compared to CO_2, while still 38% higher than that of diesel, NG GWP100 (914 CO_2 equivalent g/kWh) decreases 40% relative to GWP20, reflecting the atmospheric oxidation of methane effects to CO_2.

In order to understand the comprehensive climate change impacts of switching from diesel to NG for the whole fuel cycle, it was estimated that GWP from well-to-tank (WTT) emissions including emissions from production, purification, and distribution, using WTT

emission values of NG (6.9 g CO_2 eq/MJ) and diesel (10.9 g CO_2 eq/MJ) from Global Transport Model of energy and emissions of shipping (MAN B&W, 2019). NG shows a GHG emission benefit from well to tank compared to diesel due to its lower WTT carbon emissions. The 100-year GWP from WTT emissions in **Figure 2.7** was added. It was found that when considering impacts of the whole fuel cycle, NG provides further GWP benefits when engine load was 75% or higher and the GWP gap between NG and diesel for smaller engine load was reduced.

Although Global warming potential (GWP) is widely used for studying global warming effects, a one-step down metric from climate change cause-effect chain, global temperature change potential (GTP) was estimated (Shine et al., 2005) in order to understand the impact directly on global surface temperature when switching from diesel to NG. Since GTP is an end-point metric and GWP is a time-integrated metric, these metrics provide different implications on climate change, especially for short-lived compounds such as CH_4 and black carbon. **Figure 2.8** shows that, compared with GWP, the GTP of CH_4 and black carbon tend to become much less from 20-year to 100-year since GTP focuses on end-point temperature change after 100 years and CH_4 is a short-lived compound; for example, CH_4 GTP reduced by 94% (67 to 4) when moving from an 20-year-basis to an 100-year-basis but its GWP only reduces by 60% (86 to 34). When considering the overall impacts from exhaust of all three compounds, the ratio of NG GWP20 to diesel is 2.10 and that of GTP20 is slightly lower (1.96), and the NG GWP 100 to diesel drops to 1.38 and that of GTP further drops to 0.89 (**Figure 2.8**). The lower GTP ratio compared to the GWP ratio indicates that the increased climate impacts when

switching to NG from diesel may be less or even negative when considering global temperature change than that indicated by GWP. For 100-year term, the end-point metric GTP shows that the global temperature change potential from the switch to NG is about 11% less than that of diesel mainly because CH_4 GTP becomes significantly less after 100 years, while GWP indicates the time-integrated climate effects in 100 years are about 38% higher when switching to NG. While GWP results show switching to NG for a marine vessel increases time-integrated climate warming effects within 100 years, little to no difference on the global temperature change potential after 100 years is indicated from GTP results.

2.3.6 Climate Change Mitigation/Control Strategies

While the CO_2 emissions are unavoidable when the engine is operating, reducing CH_4 emissions is possible via different strategies such as using shore power or cylinder deactivation. **Table 2.8** shows that with these mitigation methods, the GWP increase from NG is reduced due to lower methane emissions.

As stated previously for health effects, use of shore power when at-berth is the simplest and most efficient control measure. With shore power, the average weighted emission factors of CO_2, CH_4 and BC were estimated to decrease by 6%, 50%, and 22% to 489 g/kWh, 5.82 g/kWh, and 7 mg/kWh, respectively. By reducing emissions of greenhouse pollutants, the use of shore power reduces the GWP20 and GWP100 from NG exhaust, leading to a comparable GWP100 between NG and diesel.

Cylinder deactivation technology is an option for vessels when no shore power is available. When the engine was at idle and three cylinders were deactivated, CH_4 emissions were reduced by ~ 56% to 60% (Sommer et al., 2019), leading to the decrease of GWP20 and GWP100 from NG exhaust while still 67% and 20% larger compared to the GWP of diesel.

In addition, blending hydrogen in NG or using renewable NG (RNG) are also options to reduce carbon emissions and the corresponding climate impacts. While the emissions from RNG or NG and hydrogen blends were not measured and directly compared in this study, other studies have showed that blending 20% hydrogen in natural gas reduced brake-specific CO_2 emission factor by 5 to 15% (Akansu et al., 2004; Navarro et al., 2013), which reduces the corresponding GWP from CO_2, and liquefied biogas reduced ~70% life-cycle GWP100 (CO_2 equivalent g/km) compared to LNG (Bengtsson et al., 2012, 2014), indicating the potential climate benefits from NG.

2.4 Conclusion

Switching a dual-fuel marine vessel from diesel fuel to natural gas reduced emissions of NO_x, $PM_{2.5}$, CO_2, and BC by 92%, 93%, 18% and 97%, respectively, whereas CO and HCHO emissions increased by factors of 4 and 6, respectively, and CH_4 increased from < 0.002 g/kWh to 11.5 g/kWh. The reductions in criteria pollutants such as PM and NO_x are significant and would have a notable effect on local air quality near coastal areas where a great fraction of these pollutants come from shipping. Over the long term, the reduction in PM from NG leads to a 92% lower cancer risk but the short-term effects of

high levels of formaldehyde were of concern. However, mitigation measures are available to significantly reduce formaldehyde emission rates below that of diesel. The global warming analysis showed that NG increased 100-year fuel cycle GWP by 29%. However, when the engine operated at higher loads (>75%), the impact of the reduction of CO_2 outweighed that of CH_4 emissions, making GWP of NG comparable to diesel for these loads. In the long term, the global climate risks associated with unburned CH_4 and substantial CO_2 suggest the necessity of transitioning from fossil NG to renewable NG.

Tables & Figures

Table 2.1: Summary of test points. The rightmost column 'Filter Sample' represents the number of PM sample pairs (Teflo® + Quartz) taken.

Test Point	Fuel	Engine Load (%)	Dilution Ratio	Duration (min)	Filter Sample
1	NG	5	5.99	69	1
2	NG	30	5.09	36	1
3	NG	32	5.85	38	1
4	NG	47	5.79	40	1
5	NG	50	5.21	84	1
6	NG	75	5.23	43	1
7	NG	90	5.74	38	1
8	NG	90	5.55	58	1
9	Diesel	5	7.77	42	3
10	Diesel	26	6.51	45	3
11	Diesel	50	6.60	51	3
12	Diesel	75	6.03	55	3

Table 2.2: Health risk parameters

Parameters	EF		MWAF	MP		Cancer Potency (CP)	REL		
	NG	Diesel		Cancer	Chronic		Acute	8-hr	Chronic
Compounds	g/kWh					$(mg/kg\text{-}day)^{-1}$	ug/m^3	ug/m^3	ug/m^3
Formaldehyde	2.52	0.34	1	1	1	0.02	5.50	9.00	9.00
$PM_{2.5}$	0.13	2.17	1	1	1	1.10	/	/	5.00

Table 2.3: OEHHA Approved Target Organs

(South Coast Air Quality Management District, 2017) ("+" indicates an organ is affected by a pollutant and needed to be considered in a health index)

Type	Substance	Alimentary	Cardiovascular	Bone & Teeth	Reproductive Development	Endocrine	Eye	Hematologic	Immune	Kidney	Nervous	Respiratory	Skin
Chronic	Formaldehyde											+	
	$PM_{2.5}$											+	
8-Hour Chronic	Formaldehyde											+	
	$PM_{2.5}$												
Acute	Formaldehyde						+						
	$PM_{2.5}$												

Table 2.4: GWP and GTP CO_2 equivalent of methane and black carbon (Bond et al., 2013; Myhre et al., 2013)

	GWP		GTP	
Time (Year)	20	100	20	100
CO_2	1	1	1	1
CH_4	86	34	67	4
Black Carbon	3200	900	920	130

Table 2.5: a: Engine activity: real-world and certification cycle. b: Modal and average weighted emission factors

a	Engine Load				
	Idle	25%	50%	75%	100%
Actual Vessel Cycle	0.32	0.09	0.06	0.31	0.22
Standard E2 Cycle	0.00	0.15	0.15	0.50	0.20

Table 2.5: a: Engine activity: real-world and certification cycle. b: Modal and average weighted emission factors (continue.)

b		Engine Load [a]					Weighted	
Pollutant	Fuel Type	Idle	25%	50%	75%	100%	Actual Vessel Cycle	Standard E2 Cycle
NO_x (g/kWh)	NG	3.68 ± 0.30	1.12 ± 0.03	0.64 ± 0.02	0.52 ± 0.03	0.73 ± 0.03	0.76 ± 0.02	0.63 ± 0.02
	Diesel	15.7 ± 1.0	10.6 ± 0.5	10.9 ± 0.4	9.2 ± 0.4	9.2 ± 0.4	9.6 ± 0.2	9.4 ± 0.2
CO (g/kWh)	NG	36.3 ± 0.5	7 ± 0.1	4.7 ± 0.1	2.1 ± 0.1	1.5 ± 0.1	3.5 ± 0.1	2.5 ± 0.1
	Diesel	7.79 ± 0.17	0.83 ± 0.02	0.6 ± 0.01	0.36 ± 0.01	0.36 ± 0.01	0.67 ± 0.01	0.41 ± 0.01
CO_2 (g/kWh)	NG	1380 ± 90	572 ± 19	567 ± 18	490 ± 17	468 ± 12	521 ± 10	497 ± 10
	Diesel	1180 ± 60	588 ± 14	657 ± 11	613 ± 11	613 ± 11	635 ± 7	617 ± 7
THC[b] (g/kWh)	NG	188 ± 18	31 ± 1	15.6 ± 0.6	6 ± 0.3	4.4 ± 0.2	13.6 ± 0.7	8.0 ± 0.2
	Diesel	n/a	n/a	n/a	n/a	n/a	n/a	n/a
CH_4 [c] (g/kWh)	NG	162 ± 16	25.5 ± 0.9	12.8 ± 0.5	5 ± 0.3	3.7 ± 0.2	11.5 ± 0.6	6.6 ± 0.2
	Diesel	<LOD	<LOD	<LOD	<LOD	<LOD	<LOD	<LOD
HCHO (mg/kWh)	NG	2520 ± 520	466 ± 61	303 ± 41	139 ± 26	124 ± 17	244 ± 24	171 ± 16
	Diesel	337 ± 40	32 ± 4	16 ± 2	23 ± 2	23 ± 2	34 ± 2	22 ± 2
$PM_{2.5}$ (mg/kWh)	NG	126 ± 14[d]	9 ± 0.3	7.1 ± 0.2	13.9 ± 0.7	4.5 ± 0.3	13.5 ± 0.6	10.2 ± 0.4
	Diesel	2170 ± 120	212 ± 9	131 ± 4	119 ± 4	119 ± 4	199 ± 5	125 ± 3
OC (mg/kWh)	NG	110 ± 13[d]	13.9 ± 0.7	7.8 ± 0.4	12.6 ± 1.0	6.1 ± 0.4	13.2 ± 0.7	10.3 ± 0.6
	Diesel	2360 ± 160	151 ± 8	99 ± 4	85 ± 4	85 ± 4	172 ± 6	108 ± 3
EC (mg/kWh)	NG	6 ± 1[d]	1.0 ± 0.1	0.7 ± 0.1	0.7 ± 0.1	0.5 ± 0.1	0.8 ± 0.1	0.7 ± 0.1
	Diesel	277 ± 17	38 ± 2	28 ± 1	14.9 ± 0.8	14.9 ± 0.8	26.2 ± 0.8	17.6 ± 0.5
BC (mg/kWh)	NG	5.6 ± 2.4	1.0 ± 0.1	0.7 ± 0.1	0.8 ± 0.1	0.6 ± 0.1	0.9 ± 0.1	0.7 ± 0.1
	Diesel	296 ± 18	41 ± 2	27 ± 1	16 ± 1	16.2 ± 1	28 ± 1	19 ± 1

[a] Due to the practical limitations associated with measuring these emissions during commercial operation of the vessel, the exact engine loads for idle, 25%, 50%, 75% and 100% on this vessel were 6%, 29 – 31%, 47-50%, 75% and 90% for LNG mode and 5%, 26%, 50%, 75% and 75% for diesel mode.

[b] Total hydrocarbon emission factors from diesel exhaust were not reported here since a heated line was not used for the hydrocarbon analyzer.

[c] CH_4 concentration was under LOD (100 ppb) in diesel mode.

[d] Due to that only BC measurement was available at this test point, EC, OC and $PM_{2.5}$ were estimated from BC and average OC/EC ratio.

Table 2.6: Correlation statistical analysis between measured concentrations of HCHO, CO, CH_4, NO_x and CO_2: Determination coefficients.

	HCHO	CO	CH_4	NO_x	CO_2
HCHO	-				
CO	**99.6%**	-			
CH_4	**99.9%**	**98.8%**	-		
NO_x	-67.1%	-72.5%	23.1%	-	
CO_2	-38.5%	-44.8%	-93.5%	59.2%	-

Table 2.7: Differences in hazards risk index and climate impacts of NG compared to diesel.

	Health Risk Index	Actual	Shore Power[a]	Cylinder Deactivation	Oxidation Catalyst
Carcinogenic	MICR	-92%	/	-93%	-94%
Non-Carcinogenic	HIC	-35%	/	-61%	-92%
	HIC8	649%	/	320%	-63%
	HIA	649%	/	320%	-63%

[a] With the use of shore power, emissions from exhaust were eliminated when vessel was at berth.

Table 2.8: Differences in global warming potential of NG exhaust emissions compared to diesel.

(Calculated as $[GWP_{NG} – GWP_{diesel}] / GWP_{diesel}$).

GWP	Actual	Shore Power	Cylinder Deactivation
20-year	109%	37%	67%
100-year	38%	4%	20%

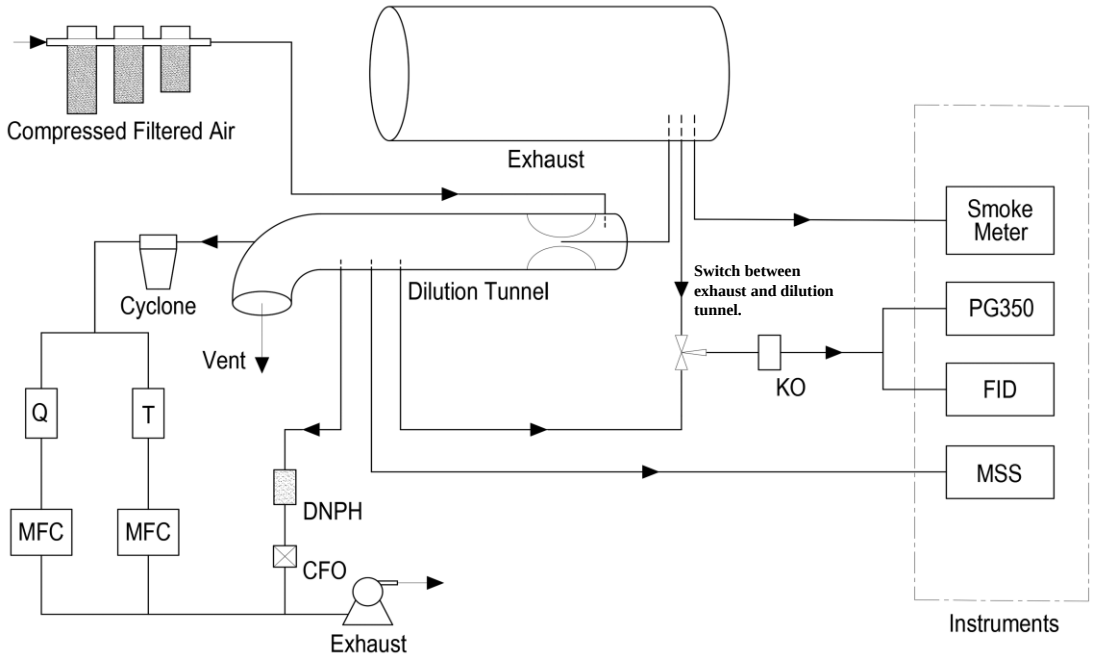

Figure 2.1: Schematic of Measurement Setup

(**Smoke Meter:** AVL Smoke Meter; **PG350:** Horiba Portable Gas Analyzer; **FID:** J.U.M. Flame Ion detector ; **MSS:** AVL Micro Soot Sensor; **KO:** Water Knock-out; **Q:** Quartz filter; **T:** Teflon filter; **MFC:** Mass flow control; **CFO:** Critical Flow Orifice; **DNPH:** Waters 2,4-Dinitrophenylhydrazine cartridges.)

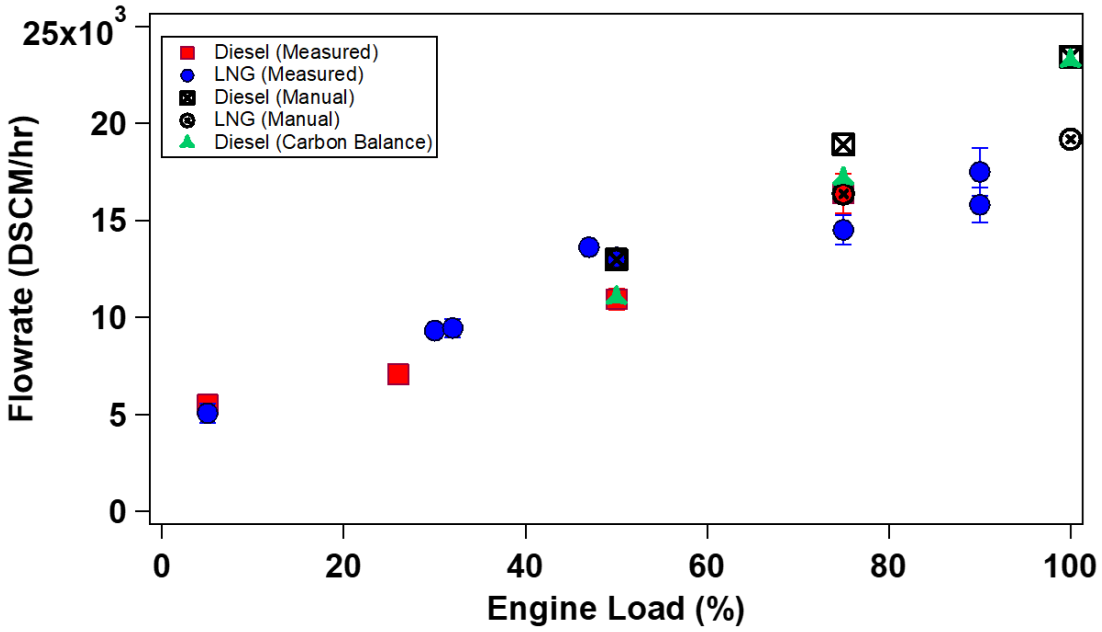

Figure 2.2: Exhaust volumetric flow rate: measured values, values from engine's manual (WÄRTSILÄ Engines, 2016) and calculated values using carbon-balance method

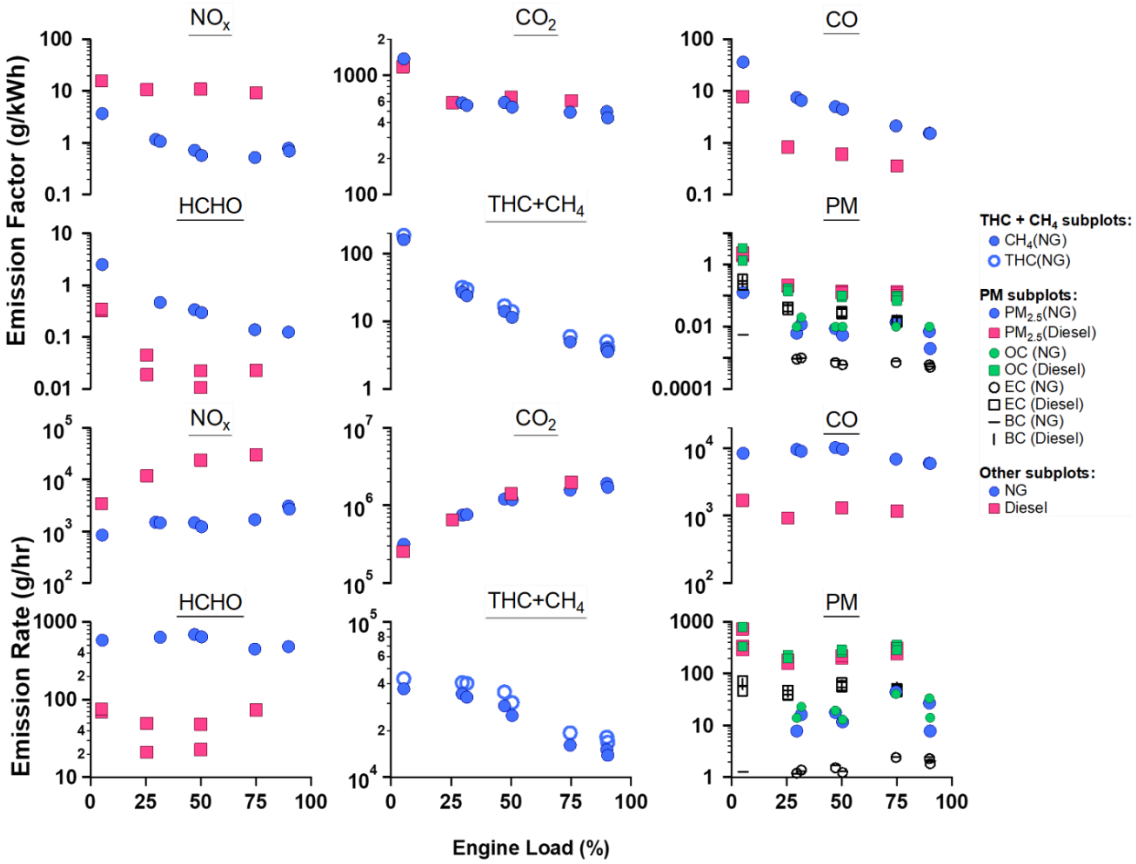

Figure 2.3: Modal Emission Rates and Factors for NO_x, CO_2, CO, HCHO, CH_4, Total hydrocarbon (THC) and $PM_{2.5}$ as well as BC, EC and OC emissions

(Square symbols represent diesel emissions and circle symbols represent NG emissions. In the "THC and CH_4" sub-figure, open and solid circles represent THC and CH_4 emissions from NG, respectively. CH_4 from diesel exhaust was below the detection limit (100 ppb) and THC from diesel was not measured. The "PM" sub-figure shows total PM mass, EC, OC and BC.)

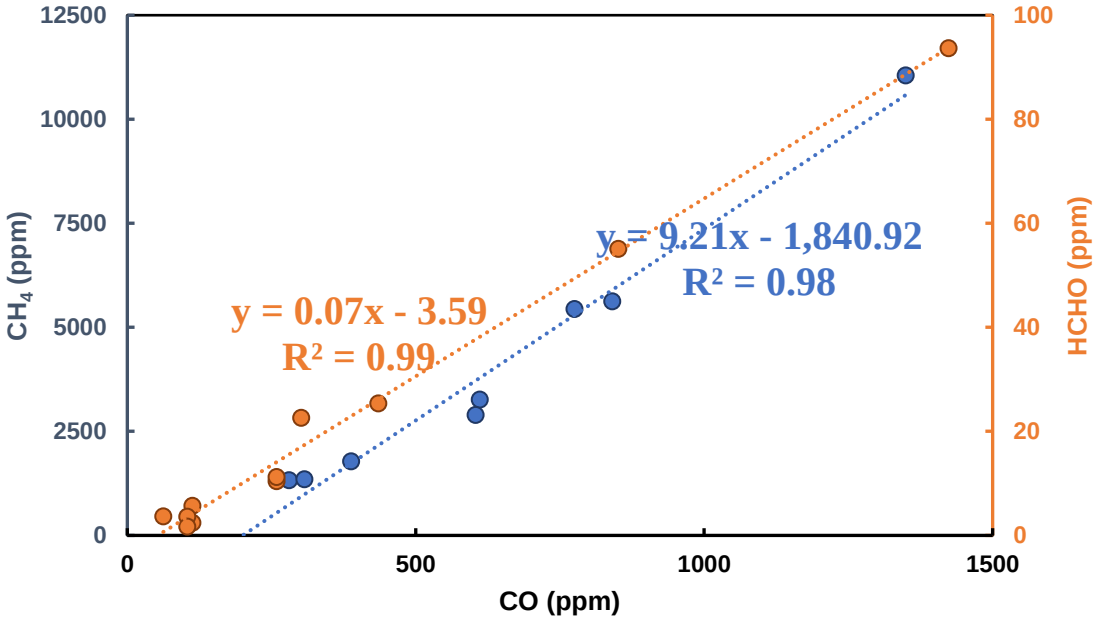

Figure 2.4: Correlation of methane and formaldehyde with CO

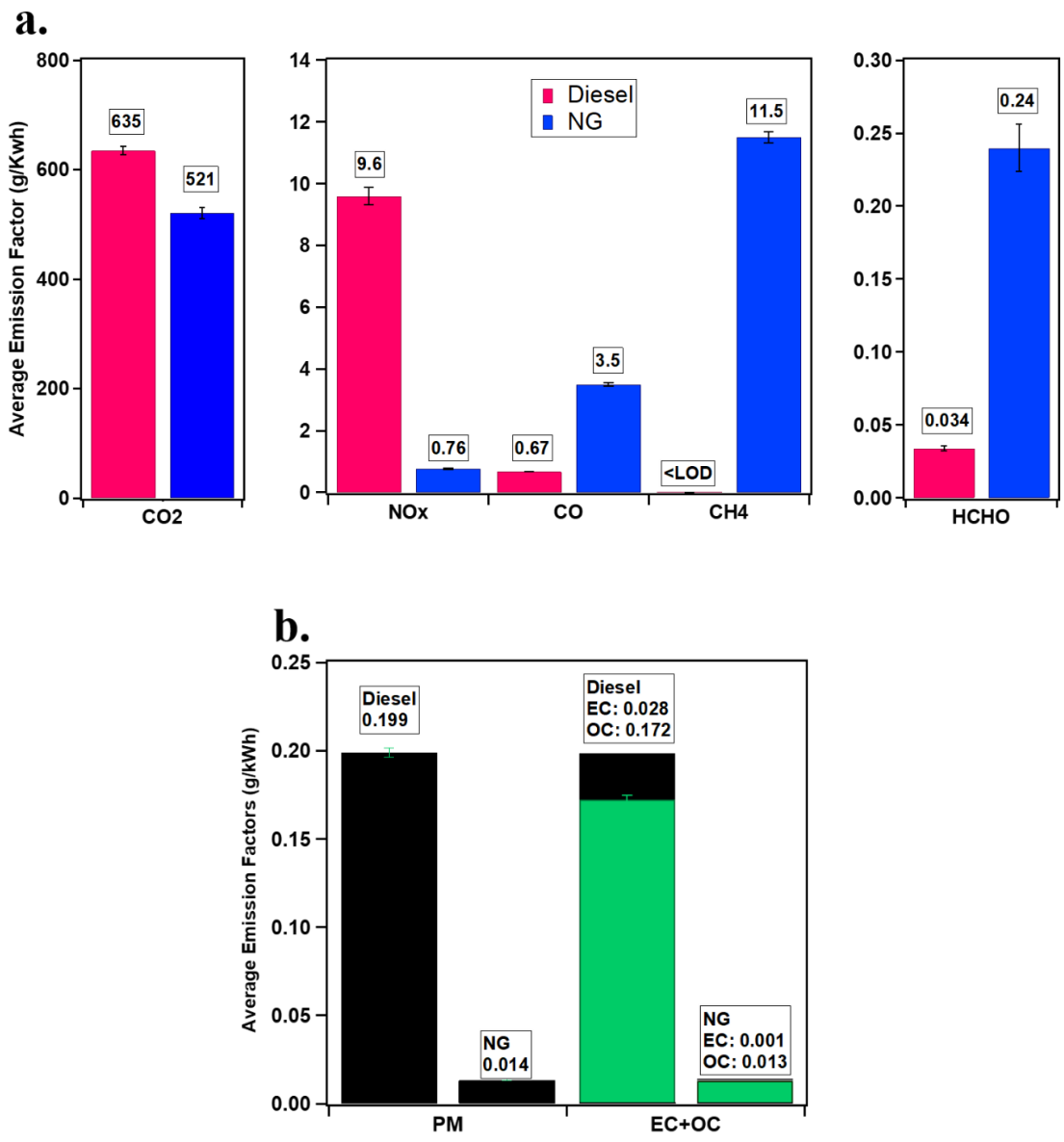

Figure 2.5: Actual-ship-cycle-weighted emission factors for both fuel modes. a: gaseous emissions (g/kWh); b: particle emissions (g/kWh). EC and OC are represented by black and green color, respectively

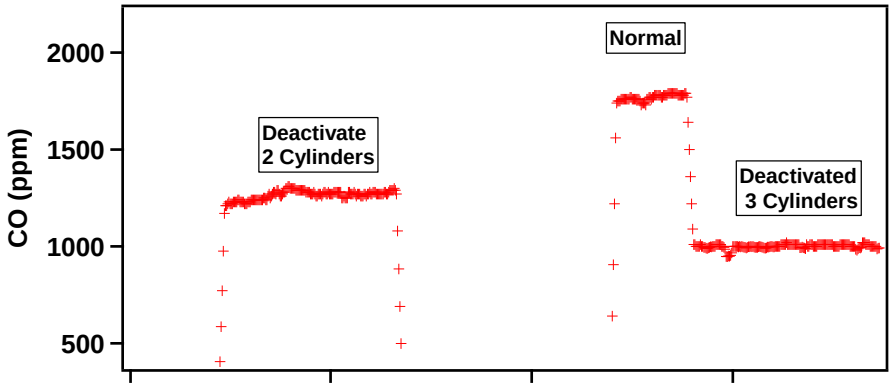

Figure 2.6: Exhaust CO concentration profile when engine was at idle with various numbers of cylinders deactivated (0, 2 and 3 cylinders deactivated)

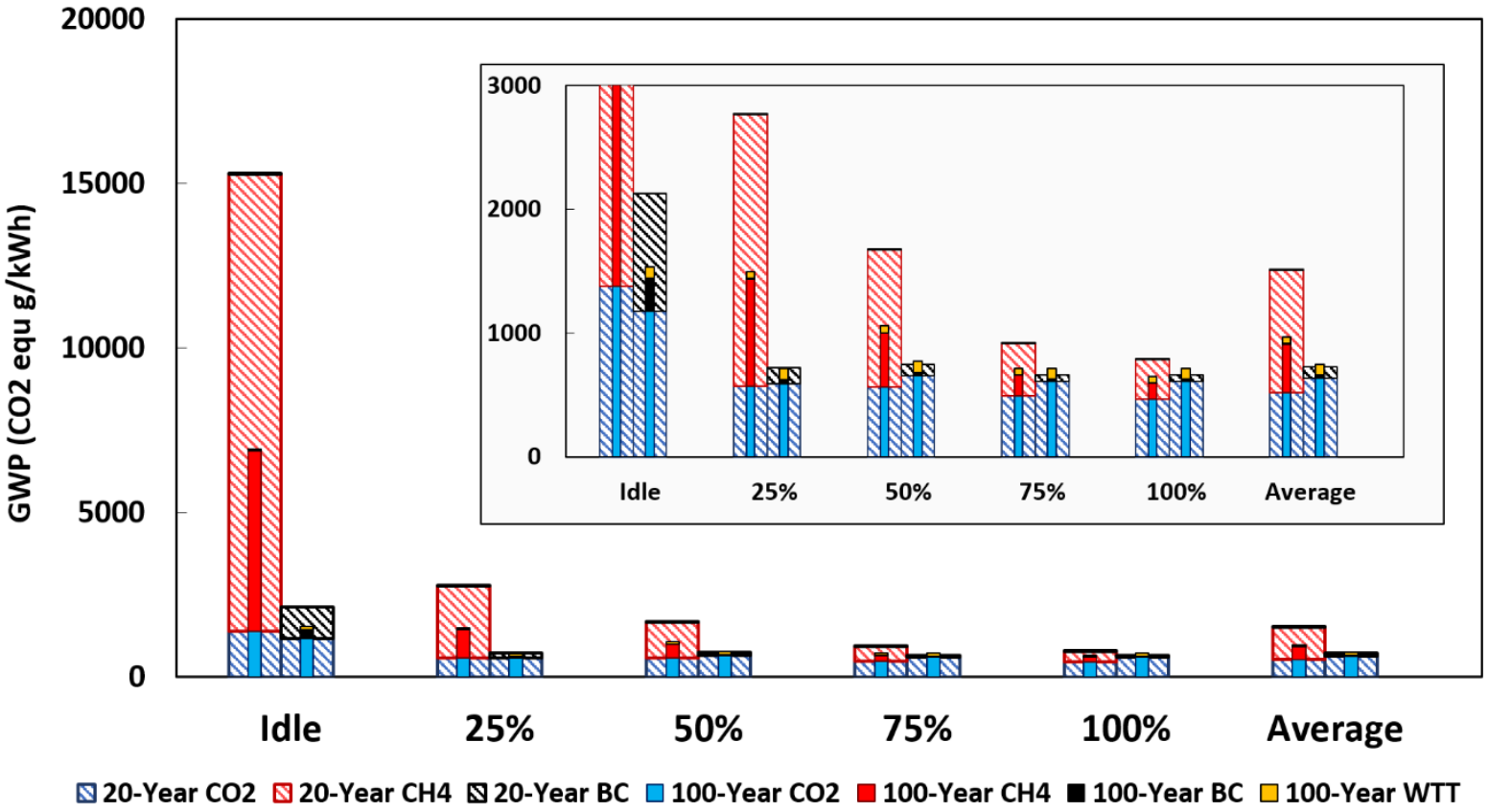

Figure 2.7: Modal and average weighted CO_2 equivalent GWP with zoomed-in view (0 to 3000 CO_2 equivalent g/kWh zoomed-in subfigure) from NG and diesel fuel exhaust using 20-year and 100-year timeframe at different engine loads

Well-to-tank (WTT) GWP were estimated using emission values from GloTraM (MAN B&W, 2019) and shown in 100-year GWP only

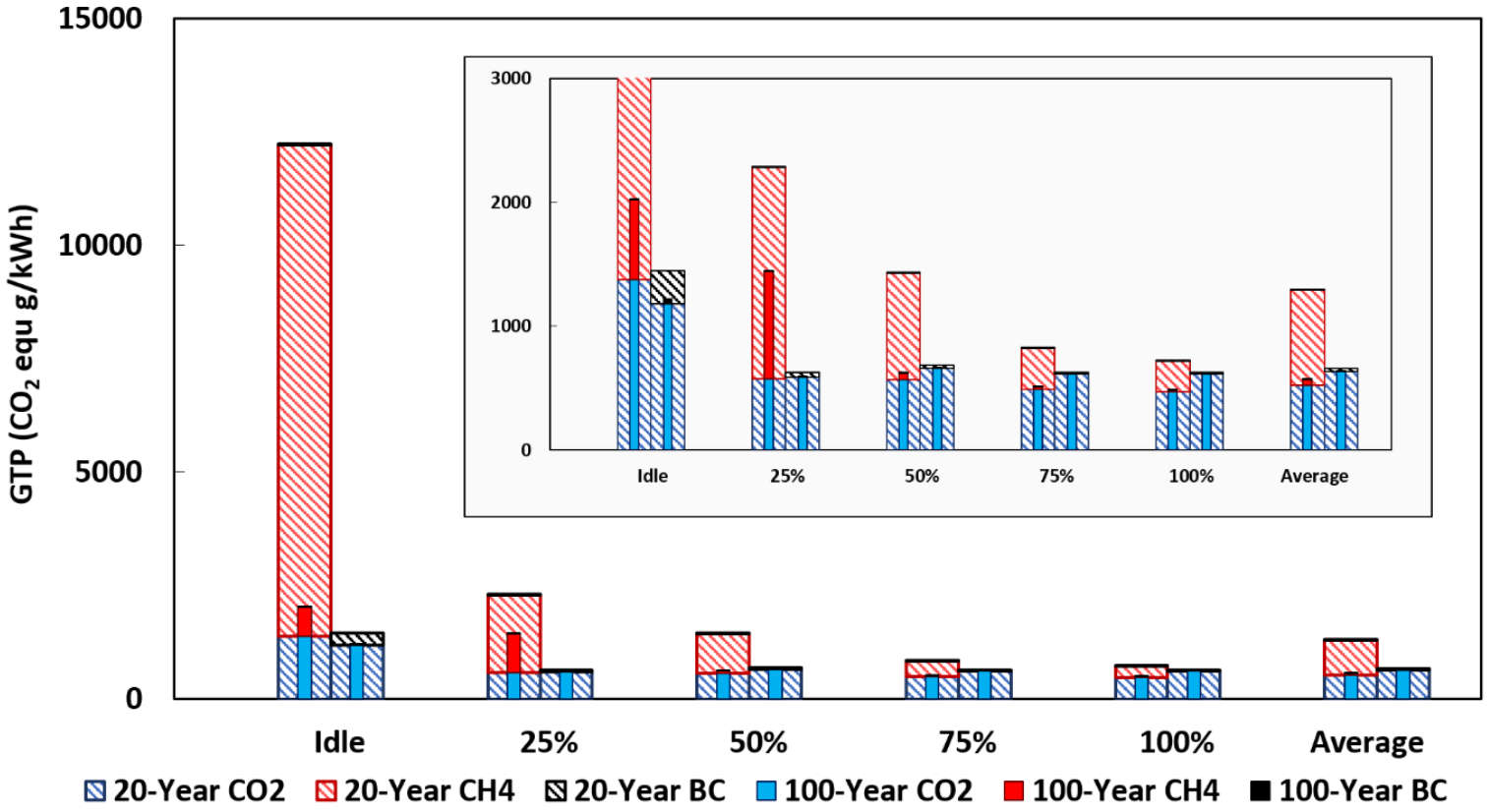

Figure 2.8: CO_2 equivalent GTP from NG and diesel fuel exhaust using 20-year and 100-year timeframe at different engine loads

Reference

Agrawal, H., Malloy, Q.G.J., Welch, W.A., Wayne Miller, J., Cocker, D.R., 2008. In-use gaseous and particulate matter emissions from a modern ocean going container vessel. Atmos. Environ. https://doi.org/10.1016/j.atmosenv.2008.02.053

Akansu, S.O., Dulger, Z., Kahraman, N., Veziroğlu, T.N., 2004. Internal combustion engines fueled by natural gas - Hydrogen mixtures. Int. J. Hydrogen Energy. https://doi.org/10.1016/j.ijhydene.2004.01.018

Alastuey, A., Moreno, N., Querol, X., Viana, M., Artíñano, B., Luaces, J.A., Basora, J., Guerra, A., 2007. Contribution of harbour activities to levels of particulate matter in a harbour area: Hada Project-Tarragona Spain. Atmos. Environ. 41, 6366–6378. https://doi.org/10.1016/j.atmosenv.2007.03.015

Anderson, M., Salo, K., Fridell, E., 2015. Particle- and Gaseous Emissions from an LNG Powered Ship. Environ. Sci. Technol. 49, 12568–12575. https://doi.org/10.1021/acs.est.5b02678

Ashley, E.K., Ph, D., Connor, P.F.O., 2017. NIOSH Manual of Analytical Methods (NMAM), 5th Edition Foreword. NIOSH Man. Anal. Methods 1–860.

Ayala, A., Gebel, M.E., Okamoto, R.A., Rieger, P.L., Kado, N.Y., Cotter, C., Verma, N., 2003. Oxidation Catalyst Effect on CNG Transit Bus Emissions. SAE Tech. Pap. Ser. https://doi.org/10.4271/2003-01-1900

Ayala, A., Kado, N.Y., Okamoto, R.A., Holmén, B.A., Kuzmicky, P.A., Kobayashi, R., Stiglitz, K.E., 2002. Diesel and CNG Heavy-duty Transit Bus Emissions over Multiple Driving Schedules: Regulated Pollutants and Project Overview. SAE Tech. Pap. Ser. 1. https://doi.org/10.4271/2002-01-1722

Bautista, A.T., Pabroa, P.C.B., Santos, F.L., Quirit, L.L., Asis, J.L.B., Dy, M.A.K., Martinez, J.P.G., 2014. Intercomparison between NIOSH, IMPROVE_A, and EUSAAR_2 protocols: Finding an optimal thermal–optical protocol for Philippines OC/EC samples. Atmos. Pollut. Res. 6, 334–342. https://doi.org/10.5094/apr.2015.037

Bengtsson, S., Fridell, E., Andersson, K., 2012. Environmental assessment of two pathways towards the use of biofuels in shipping. Energy Policy 44, 451–463. https://doi.org/10.1016/j.enpol.2012.02.030

Bengtsson, S.K., Fridell, E., Andersson, K.E., 2014. Fuels for short sea shipping: A comparative assessment with focus on environmental impact. Proc. Inst. Mech. Eng. Part M J. Eng. Marit. Environ. 228, 44–54. https://doi.org/10.1177/1475090213480349

Bond, T.C., Doherty, S.J., Fahey, D.W., Forster, P.M., Berntsen, T., Deangelo, B.J., Flanner, M.G., Ghan, S., Kärcher, B., Koch, D., Kinne, S., Kondo, Y., Quinn, P.K., Sarofim, M.C., Schultz, M.G., Schulz, M., Venkataraman, C., Zhang, H., Zhang, S., Bellouin, N., Guttikunda, S.K., Hopke, P.K., Jacobson, M.Z., Kaiser, J.W., Klimont, Z., Lohmann, U., Schwarz, J.P., Shindell, D., Storelvmo, T., Warren, S.G., Zender, C.S., 2013. Bounding the role of black carbon in the climate system: A scientific assessment. J. Geophys. Res. Atmos. 118, 5380–5552. https://doi.org/10.1002/jgrd.50171

Bryant, R., Sanni, O., Moore, E., Bundy, M., Johnson, A., 2014. An uncertainty analysis of mean flow velocity measurements used to quantify emissions from stationary sources. J. Air Waste Manag. Assoc. 64, 679–689. https://doi.org/10.1080/10962247.2014.881437

Burel, F., Taccani, R., Zuliani, N., 2013. Improving sustainability of maritime transport through utilization of Liquefied Natural Gas (LNG) for propulsion. Energy 57, 412–420. https://doi.org/10.1016/j.energy.2013.05.002

California Office of Environmental Health Hazard Assessment, 2015. Air toxics Hot Spots Program. Risk Assessment Guidelines. https://oehha.ca.gov/media/downloads/crnr/2015guidancemanual.pdf.

Cape, J.N., Coyle, M., Dumitrean, P., 2012. The atmospheric lifetime of black carbon. Atmos. Environ. https://doi.org/10.1016/j.atmosenv.2012.05.030

Chung, S.H., Seinfeld, J.H., 2002. Global distribution and climate forcing of carbonaceous aerosols. J. Geophys. Res. Atmos. 107. https://doi.org/10.1029/2001JD001397

CIMAC, 2014. Methane and Formaldehyde Emissions of Gas Engines. https://www.cimac.com/cms/upload/workinggroups/WG17/CIMAC_Position_Paper_WG17_Methane_and_Formaldehyde_Emissions_2014_04.pdf. Cimac WG17 17.

Comer, A.B., Chen, C., Rutherford, D., 2018. Relating short-term measures to IMO's minimum 2050 emissions reduction target. https://www.theicct.org/sites/default/files/publications/IMO_Short_term_potential_20181011.pdf, INTERNATIONAL COUNCIL ON CLEAN TRANSPORTATION.

Corbett, J.J., Winebrake, J.J., Green, E.H., Kasibhatla, P., Eyring, V., Lauer, A., 2007. Mortality from ship emissions: A global assessment. Environ. Sci. Technol. https://doi.org/10.1021/es071686z

Corbin, J.C., Peng, W., Yang, J., Sommer, D.E., Trivanovic, U., Kirchen, P., Miller, J.W., Rogak, S., Cocker, D.R., Smallwood, G.J., Lobo, P., Gagné, S., 2020. Characterization of particulate matter emitted by a marine engine operated with liquefied natural gas and diesel fuels. Atmos. Environ. 220. https://doi.org/10.1016/j.atmosenv.2019.117030

Delgado, B., Ayala, J.H., González, V., Afonso, A.M., 2008. Estimation of uncertainty in the analysis of carbonyl compounds by HPLC-UV using DNPH derivatization. J. Liq. Chromatogr. Relat. Technol. https://doi.org/10.1080/10826070701780664

European Environment Agency, 2013. The impact of international shipping on European air quality and climate forcing. Technical report No 4/2013. https://doi.org/10.2800/75763

Farrance, I., Frenkel, R., 2012. Uncertainty of measurement: A review of the rules for calculating Uncertainty components through functional relationships. https://www.ncbi.nlm.nih.gov/pmc/articles/PMC3387884/. Clin. Biochem. Rev.

Finlayson-Pitts, B.J., Pitts, J.N., 2000. Kinetics and Atmospheric Chemistry, in: Chemistry of the Upper and Lower Atmosphere. https://doi.org/10.1016/b978-012257060-5/50007-1

Gong, W., Beagley, S.R., Cousineau, S., Sassi, M., Munoz-Alpizar, R., Ménard, S., Racine, J., Zhang, J., Chen, J., Morrison, H., Sharma, S., Huang, L., Bellavance, P., Ly, J., Izdebski, P., Lyons, L., Holt, R., 2018. Assessing the impact of shipping emissions on air pollution in the Canadian Arctic and northern regions: Current and future modelled scenarios. Atmos. Chem. Phys. https://doi.org/10.5194/acp-18-16653-2018

Hesterberg, T.W., Lapin, C.A., Bunn, W.B., 2008. A comparison of emissions from vehicles fueled with diesel or compressed natural gas. Environ. Sci. Technol. 42, 6437–6445. https://doi.org/10.1021/es071718i

Hesterberg, T.W., Long, C.M., Bunn, W.B., Lapin, C.A., McClellan, R.O., Valberg, P.A., 2012. Health effects research and regulation of diesel exhaust: An historical overview focused on lung cancer risk. Inhal. Toxicol. https://doi.org/10.3109/08958378.2012.691913

Huang, C., Hu, Q., Wang, Hanyu, Qiao, L., Jing, S., Wang, Hongli, Zhou, M., Zhu, S., Ma, Y., Lou, S., Li, L., Tao, S., Li, Y., Lou, D., 2018. Emission factors of particulate and gaseous compounds from a large cargo vessel operated under real-world conditions. Environ. Pollut. https://doi.org/10.1016/j.envpol.2018.07.036

International Organization for Standardization, 1996. ISO 8178-2 Reciprocating internal combustion engines -- Exhaust emission measurement -- Part 2: Measurement of gaseous and particulate exhaust emissions under field conditions. ISO: Geneva, Switzerland, Geneva, Switzerland.

IPCC, I.P.O.C.C., 2007. Climate Change 2007 - The Physical Science Basis: Working Group I Contribution to the Fourth Assessment Report of the IPCC.

Johnson, A.N., Bryant, R.A., Wong, T.M., Whetstone, J.R., Dietz, T., Giel, D., Elam Jr., D., Swiggard, S., Kang, W., Sohinder, I., Harman, E., Lee, H.-H., Zhang, L., Gillis, K., Grot, R., 2016. Measurement Challenges and Metrology for Monitoring CO2 Emissions from Smokestacks – Workshop Summary. Gaithersburg, MD. https://doi.org/10.6028/NIST.SP.1201

Khan, M.Y., Giordano, M., Gutierrez, J., Welch, W.A., Asa-Awuku, A., Miller, J.W., Cocker, D.R., 2012. Benefits of two mitigation strategies for container vessels: Cleaner engines and cleaner fuels. Environ. Sci. Technol. 46, 5049–5056. https://doi.org/10.1021/es2043646

Kristensen, P.G., 2007. Formaldehyde reduction by catalyst. Danish Gas Technology Centre. http://www.dgc.eu/sites/default/files/filarkiv/documents/R0703_formaldehyd_reduction.pdf.

Krzyzanowski, M., Quackenboss, J.J., Lebowitz, M.D., 1990. Chronic respiratory effects of indoor formaldehyde exposure. Environ. Res. https://doi.org/10.1016/S0013-9351(05)80247-6

Kutlar, O.A., Arslan, H., Calik, A.T., 2005. Methods to improve efficiency of four stroke, spark ignition engines at part load. Energy Convers. Manag. https://doi.org/10.1016/j.enconman.2005.03.008

Lashof, D.A., Ahuja, D.R., 1990. Relative contributions of greenhouse gas emissions to global warming. Nature. https://doi.org/10.1038/344529a0

Le Fevre, C., 2018. A review of demand prospects for LNG as a marine transport fuel. Oxford, United Kingdom. https://doi.org/10.26889/9781784671143

Lehtoranta, K., Aakko-Saksa, P., Murtonen, T., Vesala, H., Ntziachristos, L., Rönkkö, T., Karjalainen, P., Kuittinen, N., Timonen, H., 2019. Particulate Mass and Nonvolatile Particle Number Emissions from Marine Engines Using Low-Sulfur Fuels, Natural Gas, or Scrubbers. Environ. Sci. Technol. 53, 3315–3322. https://doi.org/10.1021/acs.est.8b05555

Lin, H., Tao, J., Qian, Z. (Min), Ruan, Z., Xu, Y., Hang, J., Xu, X., Liu, T., Guo, Y., Zeng, W., Xiao, J., Guo, L., Li, X., Ma, W., 2018. Shipping pollution emission associated with increased cardiovascular mortality: A time series study in Guangzhou, China. Environ. Pollut. https://doi.org/10.1016/j.envpol.2018.06.027

Liu, H., Fu, M., Jin, X., Shang, Y., Shindell, D., Faluvegi, G., Shindell, C., He, K., 2016. Health and climate impacts of ocean-going vessels in East Asia. Nat. Clim. Chang. https://doi.org/10.1038/nclimate3083

Liu, J., Yang, F., Wang, H., Ouyang, M., Hao, S., 2013. Effects of pilot fuel quantity on the emissions characteristics of a CNG/diesel dual fuel engine with optimized pilot injection timing. Appl. Energy 110, 201–206. https://doi.org/10.1016/j.apenergy.2013.03.024

MAN B&W, 2019. LNG as a marine fuel in the EU. https://www.transportenvironment.org/sites/te/files/LNG_as_a_marine_fuel_in_the_EU_UMAS_2018.pdf. Univ. Marit. Advis. Serv. 17pp.

Matthias, V., Bewersdorff, I., Aulinger, A., Quante, M., 2010. The contribution of ship emissions to air pollution in the North Sea regions. Environ. Pollut. 158, 2241–2250. https://doi.org/10.1016/j.envpol.2010.02.013

McGwin, G., Lienert, J., Kennedy, J.I., 2010. Formaldehyde exposure and asthma in children: A systematic review. Environ. Health Perspect. https://doi.org/10.1289/ehp.0901143

Miller, S.M., Matross, D.M., Andrews, A.E., Millet, D.B., Longo, M., Gottlieb, E.W., Hirsch, A.I., Gerbig, C., Lin, J.C., Daube, B.C., Hudman, R.C., Dias, P.L.S., Chow, V.Y., Wofsy, S.C., 2008. Sources of carbon monoxide and formaldehyde in North America determined from high-resolution atmospheric data. Atmos. Chem. Phys. https://doi.org/10.5194/acp-8-7673-2008

Monteiro, A., Russo, M., Gama, C., Borrego, C., 2018. How important are maritime emissions for the air quality: At European and national scale. Environ. Pollut. https://doi.org/10.1016/j.envpol.2018.07.011

Myhre, G., Shindell, D., Bréon, F.-M.F.-M., Collins, W., Fuglestvedt, J.S., Huang, J., Koch, D., Lamarque, J.-F.J.-F., Lee, D., Mendoza, B., Nakajima, T., Robock, A., Stephens, G., Takemura, T., Zhan, H., Zhang, H., 2013. Anthropogenic and Natural Radiative Forcing, in: Intergovernmental Panel on Climate Change (Ed.), Climate Change 2013 - The Physical Science Basis. Cambridge University Press, Cambridge, pp. 659–740. https://doi.org/10.1017/CBO9781107415324.018

Navarro, E., Leo, T.J., Corral, R., 2013. CO2 emissions from a spark ignition engine operating on natural gas-hydrogen blends (HCNG). Appl. Energy. https://doi.org/10.1016/j.apenergy.2012.02.046

Nielsen, G.D., Wolkoff, P., 2010. Cancer effects of formaldehyde: A proposal for an indoor air guideline value. Arch. Toxicol. https://doi.org/10.1007/s00204-010-0549-1

Olmer, N., Comer, B., Roy, B., Mao, X., Rutherford, D., 2017. Greenhouse Gas Emissions From Global Shipping, 2013-2015. https://theicct.org/sites/default/files/publications/Global-shipping-GHG-emissions-2013-

2015_ICCT-Report_17102017_vF.pdf, The International Council on Clean Transportation.

OSHA, 2003. Title 29. Chapter XVII. Part 1910.1048. Formaldehyde, OSHA. U.S. Code of Federal Regulations.

Pamler, P.I., Jacob, D.J., Fiore, A.M., Martin, R. V., Chance, K., Kurosu, T.P., 2003. Mapping isoprene emissions over North America using formaldehyde column observations from space. J. Geophys. Res. D Atmos. https://doi.org/10.1029/2002jd002153

Pavlenko, N., Comer, B., Zhou, Y., Clark, N., Rutherford, D., 2020. The climate implications of using LNG as a marine fuel. https://theicct.org/sites/default/files/publications/Climate_implications_LNG_marinefuel_01282020.pdf, ICCT Working Paper 2020-02.

Pope, A., Burnett, R., Thun, M., EE, C., D, K., I, K., GD, T., 2002. Long-term Exposure to Fine Particulate Air Pollution. Jama 287, 1192. https://doi.org/10.1001/jama.287.9.1132

Sebaei, A.S., Gomaa, A.M., El-Zwahry, A.A., Emara, E.A., 2018. Determination of Formaldehyde by HPLC with Stable Precolumn Derivatization in Egyptian Dairy Products. Int. J. Anal. Chem. https://doi.org/10.1155/2018/2757941

Seinfeld, J.H., 2015. TROPOSPHERIC CHEMISTRY AND COMPOSITION | Aerosols/Particles, in: Encyclopedia of Atmospheric Sciences. Elsevier. https://doi.org/https://doi.org/10.1016/B978-0-12-382225-3.00438-2

Shallcross, P., Kleinitz, U., Mueller, S., 2012. Marpol Annex VI. Superyacht Bus.

Sharafian, A., Blomerus, P., Mérida, W., 2019. Natural gas as a ship fuel: Assessment of greenhouse gas and air pollutant reduction potential. Energy Policy 131, 332–346. https://doi.org/10.1016/j.enpol.2019.05.015

Shine, K.P., Fuglestvedt, J.S., Hailemariam, K., Stuber, N., 2005. Alternatives to the Global Warming Potential for comparing climate impacts of emissions of greenhouse gases. Clim. Change 68, 281–302. https://doi.org/10.1007/s10584-005-1146-9

Sommer, D.E., Yeremi, M., Son, J., Corbin, J.C., Gagné, S., Lobo, P., Miller, J.W., Kirchen, P., 2019. Characterization and Reduction of In-Use CH 4 Emissions from a Dual Fuel Marine Engine Using Wavelength Modulation Spectroscopy. Environ. Sci. Technol. 53, 2892–2899. https://doi.org/10.1021/acs.est.8b04244

South Coast Air Quality Management District, 2017. RISK ASSESSMENT PROCEDURES for Rules 1401, 1401.1 and 212. Version 8.1.

http://www.aqmd.gov/docs/default-source/permitting/rule-1401-risk-assessment/riskassessproc-v8-1.pdf?sfvrsn=12.

Thomson, H., Corbett, J.J., Winebrake, J.J., 2015. Natural gas as a marine fuel. Energy Policy 87, 153–167. https://doi.org/10.1016/j.enpol.2015.08.027

Trivanovic, U., Corbin, J.C., Baldelli, A., Peng, W., Yang, J., Kirchen, P., Miller, J.W., Lobo, P., Gagné, S., Rogak, S.N., 2019. Size and morphology of soot produced by a dual-fuel marine engine. J. Aerosol Sci. https://doi.org/10.1016/j.jaerosci.2019.105448

UNCTAD, 2019. Review of Maritime Transport 2019. https://unctad.org/en/PublicationsLibrary/rmt2019_en.pdf.

United States Environmental Protection Agency, 2011. Title 40. Chapter I. Subchapter C. Part 60. Appendix A. Determination of Stack Gas Velocity and Volumetric Flow Rate (Type S Pitot). U.S. Code of Federal Regulations.

United States Environmental Protection Agency, 2010. Title 40. Chapter I. Subchapter U. Part 1065. Subpart G. Section 1065.672. Drift correction. U.S. Code of Federal Regulations.

United States Environmental Protection Agency, 1998. Title 40. Chapter I. Subchapter C. Part 50. Appendix L. Reference Method for the Determination of Fine Particulate Matter as PM2.5 in the Atmosphere. U.S. Code of Federal Regulations.

United States Environmental Protection Agency, 1994. Title 40. Chapter I. Subchapter C. Part 88. Subpart A. Emission Standards For Clean-Fuel Vehicles. U.S. Code of Federal Regulations.

Vos, K.R., Shaver, G.M., Ramesh, A.K., McCarthy, J., 2019. Impact of Cylinder Deactivation and Cylinder Cutout via Flexible Valve Actuation on Fuel Efficient Aftertreatment Thermal Management at Curb Idle. Front. Mech. Eng. https://doi.org/10.3389/fmech.2019.00052

WÄRTSILÄ Engines, 2016. WÄRTSILÄ 34DF PRODUCT GUIDE. https://www.wartsila.com/docs/default-source/product-files/engines/df-engine/product-guide-o-e-w34df.pdf?utm_source=engines&utm_medium=dfengines&utm_term=w34df&utm_content=productguide&utm_campaign=msleadscoring.

Woodyard, D., 2009. Pounder's Marine Diesel Engines and Gas Turbines. Elsevier. https://doi.org/10.1016/C2009-0-25444-4

Xiao, Q., Li, M., Liu, H., Fu, M., Deng, F., Lv, Z., Man, H., Jin, X., Liu, S., He, K., 2018. Characteristics of marine shipping emissions at berth: Profiles for particulate matter and

volatile organic compounds. Atmos. Chem. Phys. 18, 9527–9545. https://doi.org/10.5194/acp-18-9527-2018

Yang, L., Tyner, W.E., Sarica, K., 2013. Evaluation of the economics of conversion to compressed natural gas for a municipal bus fleet. Energy Sci. Eng. https://doi.org/10.1002/ese3.14

Zhang, X., Zhao, Y., Song, J., Yang, X., Zhang, J., Zhang, Y., Li, R., 2018. Differential Health Effects of Constant versus Intermittent Exposure to Formaldehyde in Mice: Implications for Building Ventilation Strategies. Environ. Sci. Technol. https://doi.org/10.1021/acs.est.7b05015

Chapter 3 : Secondary Organic Aerosol (SOA) Formation from Aromatic Compound at Very Low NO_x Conditions: The Dependence on RO_2+RO_2 Pathway

3.1 Introduction

Particulate matter (PM) has adverse effects on air quality, visibility, human health and climate change and up to 90% of sub-micro PM are organic aerosol (Corbin et al., 2020; Jimenez et al., 2009; Myhre et al., 2013; Zhao et al., 2013). Secondary organic aerosol (SOA) is estimated to account for a dominant fraction of atmospheric organic aerosol mass (Hallquist et al., 2009). Aromatic hydrocarbons, as a major anthropogenic SOA precursors, contribute to 50 – 70% of the SOA formation in urban regions (Kanakidou et al., 2005; Na et al., 2004).

In the atmosphere, the oxidation of aromatic volatile organic compounds (VOCs) can be initiated by hydroxyl (OH) radicals followed by the abstraction of a hydrogen atom and the addition of O_2, leading to the formation of alkylperoxyl (RO_2) radicals. The fate of RO_2 radicals plays an important role on aromatic SOA formation. It is generally believed that the reactions of RO_2 with hydroperxyl (HO_2) radicals and nitric oxide (NO) are the two major pathways that forms SOA in OH-initiated aromatic oxidation systems. SOA formation potential under high- and low-NO_x (no injection of NO_x) conditions in chamber studies are usually used to represent the products from RO_2+HO_2 and RO_2+NO pathways, respectively (Li et al., 2015; Ng et al., 2007; Pye et al., 2010; Song et al., 2007a). The corresponding SOA parameters for RO_2+HO_2 and RO_2+NO are used along with a branching ratio term (β) of RO_2+NO with respect to RO_2+HO_2 to estimate SOA

formation at different NO_x conditions (Carlton et al., 2010; Pye et al., 2010). The β is calculated with **Equation 3.1**, where k_{RO_2+NO} and $k_{RO_2+HO_2}$ are the reaction constants of RO_2 with NO and HO_2 respectively.

$$\beta = \frac{k_{RO_2+NO}[NO]}{k_{RO_2+HO_2}[HO_2]+k_{RO_2+NO}[NO]} \qquad \textbf{Equation 3.1}$$

A few studies have investigated SOA formation from aromatic at low NO_x conditions in chamber. Song *et al*. proposed that organic hydroperoxide compounds from HO_2+RO_2 pathway contribute to SOA formation and reported a 9% to 31% SOA yield from *m*-xylene in the absence of NO_x by introducing H_2O_2 as the OH source (Song et al., 2007a). Ng *et al*. reported a constant 36% yield of non-volatile products from *m*-xylene in the absence of NO_x (Ng et al., 2007). Later, Nakao *et al*. reported a 19 – 28%, 17 – 23%, and 10 – 32% SOA yield for benzene, toluene, and *m*-xylene with no injected NO_x (Nakao et al., 2011).

In the current global transport models, a constant yield of non-volatile products is used to represent the SOA yield of different aromatic compounds from HO_2 pathway as opposed to NO pathway: GEOS-Chem (30% to 37%) and CMAQ (37% to 48%) (Carlton et al., 2010; Ng et al., 2007; Pye et al., 2010). However, the large variance of the reported SOA yield shows that SOA yield may be impacted by other parameters in chamber, thus a constant yield may not be accurate to represent the SOA formation potential of aromatic compounds at low NO_x conditions. It is critical to understand what is driving the large variance of SOA yield as it can potentially explain the large uncertainties on anthropogenic SOA prediction from global transport models (Farina et al., 2010).

While RO_2+NO and RO_2+HO_2 are believed to be the most important pathways for SOA formation, RO_2 radicals can also compete with HO_2 and NO through self- and cross- reactions and this pathway becomes more important for regions with less NO_x and more RO_2 (Berndt et al., 2018; Kroll and Seinfeld, 2008; Kwan et al., 2012; Schervish and Donahue, 2020). There are three major pathways that represent RO_2 self- and cross-reactions (**R1**- **R3**) (Kroll and Seinfeld, 2008; Kwan et al., 2012): **R1** propagates RO radicals; **R2** forms carbonyl and alcohol products which are more volatile than the hydroxperoxide (ROOH) products from RO_2+HO_2 pathway; and through **R3**, the large RO_2 radicals undergo dimerization and form organic peroxides (ROOR') with very low vapor pressures. Currently the SOA from RO_2+RO_2 pathway is not well understood and not included in models. While under high NO_x conditions, RO_2+RO_2 is less important and RO_2+NO is the dominant pathway on SOA formation, it may be important under no or low NO_x conditions when RO_2+NO is not significant, depending on the competition between RO_2+RO_2 reactions and RO_2+HO_2 reactions. To the best of our knowledge, no studies have discussed the contribution the aromatic SOA from RO_2+RO_2 pathway. It is necessary to investigate this pathway under low NO_x conditions.

RO_2+R'CH_2O_2 → RO+R'CH_2O+O_2 **(R1)**

RO_2+ R'CH_2O_2 → ROH+R'CHO+O_2 **(R2)**

RO_2+RO_2→ ROOR'+O_2 **(R3)**

The ratio of HO_2/RO_2 can be an indicator on the competition between RO_2 and HO_2 that consumes RO_2 and form lower volatility products. A few studies investigated

the impacts of HO_2/RO_2 of SOA formation from alkene ozonolysis in chamber and suggested that increasing HO_2/RO_2 ratio increased SOA formation from alkene with an endocyclic double bond (e.g., α-pinene and cyclohexene), but decreased SOA formation from alkene with an exocyclic double bond (e.g., β-pinene) (Docherty and Ziemann, 2003; Henry and Donahue, 2011; Keywood et al., 2004). However, the contribution of RO_2+RO_2 pathway resulted from the HO_2/RO_2 change to SOA formation was not further discussed. To fill the gap from those studies, it is important to explore the impact on chamber aerosol yield from the contribution of the RO_2+RO_2 pathway.

Other parameters such as light-intensity and NO_x off-gassing from the chamber wall may also impact the SOA yield at low NO_x conditions. Studies showed that increasing light intensity could increase SOA formation from *m*-xylene (Warren et al., 2008) and α-pinene (Liu et al., 2009) with the presence of high NO_x in chamber, however, the impact may be different in low or no NO_x conditions. In addition, while the RO_2+HO_2 pathway is often represented by chamber experiments with no NO_x injected, it is almost impossible to achieve the absolute NO_x-free condition in a Teflon environmental chamber due to the wall effects such as NO_x off-gassing (Carter et al., 2005), thus the impact of NO_x off-gassing to gas-phase chemistry is more important for low NO_x conditions in chamber. The NO_x off-gassing difference from different chamber and different experiment may also be responsible for the SOA yield variance at low NO_x conditions.

In this study, the SOA formation from *m*-xylene with no injected NO_x in UCR/CECERT environmental chamber with different light intensities, NO_x off-gassing

from wall and H_2O_2 concentrations (HO_2/RO_2 ratios) was investigated. The impact of those factors on SOA formation and the contribution of RO_2+RO_2 pathway to SOA formation were evaluated. Three types of yield curves were observed under different HO_2/RO_2 conditions and the corresponding volatility basis set (VBS) parameters were developed. The HO_2/RO_2 – dependent parameters were fitted with real-time chamber data to predict real time SOA as compared with the parameters from GEOS-Chem. A reactive organic gases (ROG) surrogate mixture was added in several experiments to simulate the urban environments to investigate if the HO_2/RO_2 – dependent parameters still holds with the presence of other VOCs. A global average HO_2/RO_2 ratio for January and July and the impacts on SOA prediction from aromatic compounds when using different SOA yield curve at low NO_x conditions were estimated using GEOS-Chem. In addition, the suggestions on chamber experiment design were provided when studying SOA formation at low NO_x conditions.

3.2 Method

All 29 *m*-xylene photo-chemical experiments (**Table 3.1**) were conducted in the UC Riverside/CE-CERT 90 m^3 environmental chamber with the maximum of 272 115W Sylvania 350nm black-lights, where the temperature, pressure, humidity and light intensity are well controlled (Carter et al., 2005). *m*-Xylene (99%) and H_2O_2 (50%) from Sigma Aldrich were injected into the chamber before the photo-oxidation as SOA precursor and OH and HO_2 source. The initial concentration of *m*-xylene and H_2O_2 varied from 11 to 229 ppb and 0.4 to 4 ppm, respectively. Since no additional NO_x were added into any experiments and the only NO_x source was off-gassing from the chamber wall

with the rate varying from 0.8 to 2.5 ppt/min (Carter et al., 2005), all the experiments were defined as very low NO_x conditions. The wall effects from our chamber reactors were characterized on a regular basis by determining the magnitude of NO_x off-gassing rate so that the model could correctly predict ozone yields from a series of chamber characterization experiments, as described by Carter *et al*. (Carter et al., 2005). 1 ppm of a reactive organic gas (ROG) surrogate mixture (**Table 3.2**) was added into several experiments to simulate the environment of a regular urban atmosphere (Kacarab, 2013). Different number of black lights were used to simulate light intensities represented by NO_2 photolysis rate k_1 from 0.125 to 0.401 /min. All the experiments were run at 301 ± 1 K and dry condition (RH < 0.1%) in the absence of seeds.

A home-built scanning mobility particle sizer was used to obtain particle size distribution (27 to 686 nm) (Cocker et al., 2001a). A Kanomax aerosol particle mass analyzer (APM) was used to measure particle density (Malloy et al., 2009). An Agilent gas chromatography (Model 6890) with flame ion detectors (GC-FID) was used to measure the hydrocarbon concentrations. A gas-phase chemistry mechanism SAPRC11 was used to obtain the concentrations of radicals such as NO, OH, HO_2 and RO_2 (Carter and Heo, 2012). **Figure 3.1** shows a typical profile of the branching ratio of RO_2+NO pathway (β) when only considering competition with RO_2+HO_2 pathway, *m*-xylene, O_3 and NO_x from SAPRC11 mechanism and experiment measurements. The RO_2+NO pathway in very low NO_x experiments studied here is resulted from NO off-gassing from chamber wall and accounts for at most 3% of RO_2 branching for all experiments (mostly < 1%). The average OH concentrations (**Figure 3.2**) of all experiments studied here are

obtained from SAPRC11 mechanism and a typical method of calculating OH radical using *m*-xylene decay (Li et al., 2018). The great agreement of *m*-xylene decay, and O_3 formation between SAPRC11 and measurement and average OH concentrations between SAPRC11 and *m*-xylene decay method indicates the gas-phase chemistry in chamber is well estimated using SAPRC11.

The SOA yield (Y) was calculated using **Equation 3.2** where ΔM_o is the formed SOA mass and ΔHC is the consumed hydrocarbon (Odum et al., 1996a). The VBS parameters were developed using **Equation 3.3** (Donahue et al., 2006) where C_{OA} is the total SOA mass, C_i^* is the effect saturation concentration of each of the four products (0.1, 1, 10, 100 ug/m^3) and C_i is the total concentration of a product in gas- and particle-phase. A VBS chamber model considering real-time HO_2/RO_2 effect was developed to estimate SOA formation from *m*-xylene in chamber with *m*-xylene decay profile (10-minutes resolution) using the parameters from current models and those obtained from this study.

$$Y = \frac{\Delta M_o}{\Delta HC} \qquad \textbf{Equation 3.2}$$

$$C_{OA} = \sum_i^4 C_i * \left(1 + \frac{C_i^*}{C_{OA}}\right)^{-1} \qquad \textbf{Equation 3.3}$$

A global 3-d model (GEOS-Chem) of atmospheric chemistry driven by the assimilated meteorological data from the Goddard Earth Observing System (GEOS) was used in this study to estimate the global HO_2/RO_2 ratio. The *m*-xylene SOA parameters at

low-NO_x conditions were replaced with those obtained from this study to estimate the impact on *m*-xylene SOA when considering the impacts from RO_2+RO_2 pathway.

3.3 Results and Discussion

A large range of SOA yield (10% to 42%) was observed under different initial *m*-xylene and H_2O_2 concentrations, light intensity and wall off-gassing at the very low NO_x conditions (**Figure 3.3**). No clear single yield curve can be directly obtained from the scattered data points on **Figure 3.3** and the current applied yield parameter (36%) can only represent a small fraction experiments in this study. It is important to understand what drives the difference on SOA potential from *m*-xylene under very low NO_x conditions and provide more representative SOA parameters to improve the SOA prediction accuracy of models.

3.3.1 Light Intensity

Light intensity impacts the photolysis of H_2O_2 and the formation of OH and HO_2. In this study, three light intensity scenarios (k_1 of 0.125, 0.150 and 0.401 min^{-1}) were used. With similar initial *m*-xylene and H_2O_2 conditions, SOA formation and *m*-xylene consumption rates increased as k_1 increases (**Figure 3.4**) except that *m*-xylene consumption rate was the fastest for the run with the medium k_1 (0.15 /min) due to its largest initial *m*-xylene concentration. The product of HO_2 and RO_2 concentrations for those three k_1 scenarios is plotted in **Figure 3.4** and its value is higher for runs with higher k_1. This can be explained by the fact that the faster OH formation from the faster H_2O_2 photolysis with the higher light intensity leads to faster oxidation of *m*-xylene and

the formation of RO_2 and HO_2. The similar dependence of $[HO_2]*[RO_2]$ and SOA formation rate on k_1: SOA forms in a faster rate when $[HO_2]*[RO_2]$ is higher, further supports that HO_2+RO_2 reaction is the major pathway for *m*-xylene SOA formation at the very low NO_x conditions (Ng et al., 2007; Song et al., 2007a).

Before the SOA formation levels off, the experiment with the largest k_1 shows the fastest and highest SOA formation. However, the final SOA formation for the three cases are very similar (**Figure 3.4**), corresponding to the similar $[HO_2]*[RO_2]$ exposure (2 to 3 $*10^{24}$ $(molecules/cm^3)^2*s$). This indicates that the light intensity dose not significantly affect SOA potential from *m*-xylene at very low NO_x condition since the final SOA yields are similar for all three scenarios (~20%). **Figure 3.5** suggests no obvious k_1 dependence on SOA yield curves from all the experiments in this study. A Pearson correlation analysis (Swinscow, 1976) (**Table 3.3**) was performed between final SOA mass and *m*-xylene consumption and adding light intensity as the third variable did not significantly improve the correlation, indicating that the light intensity is not the key factor of the large variance of SOA yield.

3.3.2 Wall Off-gassing

While this study is focusing on the SOA formation in the absence of injected NO_x, the effects of NO_x off-gassing from wall still needs to be considered when simulating gas-phase chemistry in chamber with SAPRC11 mechanism. NO_x wall off-gassing is more important for very low NO_x experiments but can be ignored in high NO_x experiments due to its low magnitude. The NO_x off-gassing rate for all experiments in

this study was within 0.8 ppt/min to 2.5 ppt/min. However, a maximum range of 0.8 ppt/min to 7 ppt/min historically observed for this chamber was used for a sensitivity test with SAPRC11 mechanism to understand the maximum impact of NO_x off-gassing to gas-phase chemistry (**Figure 3.6**) assuming initial 80 ppb *m*-xylene and 2 ppm H_2O_2. The *m*-xylene profiles with the three off-gassing rates are almost identical. The average branching ratio of RO_2+NO compared with HO_2+RO_2 increases from 0.2% to 3%, indicating that an increasing fraction of *m*-xylene forms SOA through RO_2+NO pathway while still significantly smaller than the SOA formation from RO_2+HO_2 pathway. This extent of change on branching ratio would not likely change the SOA yield as significant as observed in **Figure 3.3**. The slight increase of HO_2 and decrease of RO_2 lead to the insignificant change of the product of average HO_2 and RO_2 in chamber when changing the NO_x off-gassing rate from the lower bound to upper bound. The gas-phase chemistry sensitivity test indicates NO_x off-gassing cannot explain the large variance on the SOA yield (10% to 42%) within the experiments conducted here and may only slightly affects the SOA formation from *m*-xylene in the absence of NO_x by changing the branching ratio of HO_2+RO_2 pathway. In addition, **Figure 3.7** indicates no obvious dependence of SOA yield curve on the NO_x off-gassing rate from all the experiments in this study. The insignificant change of the Pearson correlation coefficient (**Table 3.3**) between final SOA mass and *m*-xylene consumption after adding a third variable NO_x off-gassing rate also indicates that it is not the key factor of the large variance of SOA yield.

3.3.3 H_2O_2 Impacts

Although H_2O_2 has been popularly used in very low NO_x chamber studies, how its concentration impacts SOA formation is still not well understood. A series of experiments with ~100 ppb initial *m*-xylene and 0.4, 1, 2 and 4 ppm H_2O_2 were conducted. SOA forms faster and the final amount is larger for the run with higher initial H_2O_2 concentration (**Figure 3.8)** and the run with 4ppm H_2O_2 showed the largest SOA yield (42%). While *m*-xylene consumption was also increasing with H_2O_2, SOA formation reached the highest (~50 ug/m^3) for the run with 4ppm H_2O_2 and the lowest (~15 ug/m^3) for the run with 0.4 ppm H_2O_2, after 150 ug/m^3 of *m*-xylene was consumed in both cases. The OH exposure and the average of HO_2/RO_2 ratio increased as the initial H_2O_2 increased. This indicates that the impacts of H_2O_2 on SOA formation potential are likely due to the change of the OH exposure and HO_2/RO_2 ratio in chamber.

Figure 3.9 shows that the correlation between the total SOA formation and *m*-xylene consumption can be influenced by the initial H_2O_2 concentration for the runs with less than 400 ug/m^3 of *m*-xylene consumption. Increasing initial H_2O_2 concentration in chamber increases SOA formation: with ~300 ug/m^3 *m*-xylene consumption, SOA formation was about 50-70, ~90 and 110-130 ug/m^3 with 1, 2 and 4 ppm H_2O_2 injected. The H_2O_2 impacts observed here indicates the difference of SOA formation at low NO_x conditions from different chambers (Nakao et al., 2012; Ng et al., 2007; Song et al., 2007b) might related to different amount of H_2O_2 used. It is critical to understand how initial H_2O_2 concentration impacts *m*-xylene oxidation system and this must be considered when studying SOA formation from *m*-xylene and other aromatic compounds

in absence of NO_x. However, for the runs with higher *m*-xylene consumption, the SOA yield, represented by the slope in **Figure 3.9**, was lower than the cases where less *m*-xylene was consumed but with the same amount of initial H_2O_2. This indicates that H_2O_2 alone may not be sufficient to explain the variety of SOA yield from *m*-xylene at low NO_x – the impact of initial *m*-xylene might also need to be considered.

The increase of OH and HO_2/RO_2 as H_2O_2 increases is playing an important role in SOA formation at low NO_x condition. While SOA yield increases as initial H_2O_2 when similar *m*-xylene was present (**Figure 3.9**), **Figure 3.10** indicates no obvious dependence of SOA yield curve on OH exposure in chamber when initial *m*-xylene was varied. Similar to light intensity and NO_x off-gassing, the Pearson correlation analysis (**Table 3.3**) shows that the OH exposure is not the key factor of the large variance of SOA yield as well. Among all the experiments in this study, RO_2+HO_2 is always the dominant pathway compared with RO_2+NO as its branching ratio is about 30 – 550 times higher. While RO_2+HO_2 pathway is commonly used to represent low NO_x conditions, the self- and cross- reactions of RO_2 radicals can also contribute to the loss of RO_2 and impact the final SOA formation. The ratio of HO_2/RO_2 is used as the indicator of the impacts of RO_2+RO_2 pathway. Increasing the initial H_2O_2 increases the average HO_2/RO_2 with similar initial *m*-xylene, leading to higher SOA formation, further proving the importance of considering RO_2+RO_2 pathway in *m*-xylene + H_2O_2 oxidation systems.

Figure 3.11 shows the correlation between SOA mass and the average HO_2/RO_2 ratio with grouped by the *m*-xylene consumptions. The SOA mass increases drastically with HO_2/RO_2 in low HO_2/RO_2 region and tends to level off as HO_2/RO_2 ratio further

increases. This indicates that RO_2+RO_2 pathway has impacts on SOA formation but the products from this pathway is more volatile compared to those from RO_2+HO_2 pathway. The impacts from RO_2+RO_2 pathway are comparable with RO_2+HO_2 when the HO_2/RO_2 ratio is low, thus increasing HO_2/RO_2 ratio increases the branching ratio of HO_2 with RO_2 radicals and then results in an increased SOA formation. As HO_2/RO_2 ratio raise to a certain level when the RO_2+RO_2 pathway impacts are far less significant, increasing HO_2/RO_2 ratio is not able to change the HO_2+RO_2 branching ratio or boost the SOA formation as almost all RO_2 radicals react with HO_2. Having considered both HO_2+RO_2 and RO_2+RO_2 pathways in our study, the ratio of HO_2/RO_2 was used to represent the contribution from HO_2+RO_2 pathway. While the branching ratio of HO_2+RO_2 better represents the HO_2+RO_2 pathway, the large uncertainties of RO_2+RO_2 reaction constant (slow to fast, $8.8*10^{-13}$ to $1*10^{-11}$) (Orlando and Tyndall, 2012; Peng et al., 2019) create a large uncertainty on the branching ratio itself.

Three different yield curves of *m*-xylene at three different HO_2/RO_2 scenarios are presented in **Figure 3.12**: 0 to 0.75, 0.75 to 1.5 and >1.5 and developed VBS parameters for those three scenarios are presented in **Table 3.4**. A constant yield (36%) of non-volatile SOA from *m*-xylene in the absence of NO_x was reported and is applied in current models (e.g. GEOS-Chem) to represent the SOA yield of HO_2 pathway (Ng et al., 2007; Pye et al., 2010). The constant 36% yield is the closet to our SOA yield curve at HO_2/RO_2>1.5 and the branching of HO_2+RO_2 (**Table 3.4**) is the largest (97% to 99% for slow RO_2+RO_2 and 80% to 95% for fast RO_2+RO_2) where SOA yield levels off at ~40%. This indicates that the current-used yield curve is only representing SOA yield from

HO_2+RO_2 pathway for larger aerosol mass loadings and may overestimate the SOA formation at lower mass loadings. However, only one constant yield curve cannot represent SOA formation potential at low NO_x conditions. Two other yield curves at lower HO_2/RO_2 conditions (<1.5 and <0.75) lead to less SOA yield and indicate the lower SOA formation from RO_2+RO_2 pathway.

The hydroperoxide products from HO_2+RO_2 reactions are with quite low volatilities and are a major component of SOA from *m*-xylene oxidation, especially in the scenarios in the absence of NO_x. Although the SOA formation from RO_2+RO_2 pathway is not well understood, the self- and cross- reactions of RO_2 impact the SOA formation in *m*-xylene+H_2O_2 system where RO_2 concentrations are sufficient and their impact is not overwhelmed by the presence of NO_x (Kroll and Seinfeld, 2008; Schervish and Donahue, 2020). The alcohol and carbonyl products from pathway (**R2**) tend to be more volatile than HO_2+RO_2 reactions products in average thus contributing to less SOA mass. While the organic peroxides (ROOR) formed through pathway (**R3**) are likely in very low volatility and may contribute to more particle mass compared with HO_2+RO_2 reactions (Ziemann, 2002), the branching ratio of ROOR forming pathway (**R3**) is only about 3-4% thus that of carbonyl- and alcohol-forming pathway is much more dominant (59-77%) among those three RO_2+RO_2 pathways (**R1-R3**).

These SOA yield curves are obtained from experiments with only *m*-xylene presented and did not consider the impacts from the presence of other VOCs and their corresponding RO_2. In this study, a reactive organic gas (ROG) surrogate mixture (Kacarab, 2013) was used to simulate urban atmosphere in several *m*-xylene+H_2O_2

experiments. Without surrogate mixture added, the average HO_2/RO_2 ratios varied from 0.5 to 5 with the injection of 25-100 ppb *m*-xylene and 1ppm H_2O_2. With 1 ppm surrogate, the ratios dropped to a more constant level (0.19 to 0.30) (**Figure 3.13**), indicating that the presence of surrogate mixture could control the HO_2/RO_2 ratio to a relatively constant level with varied initial *m*-xylene. SOA yield of runs with surrogate is presented in **Figure 3.12** and they all agree with SOA yield curve at $HO_2/RO_2<0.75$ scenario. With the addition of the RO_2 from other VOCs, there are more RO_2 radicals competes with HO_2, leading to a lower final SOA formation.

3.3.4 SOA prediction in chamber experiments

A customized VBS model was developed to predict SOA formation with the real-time HO_2/RO_2 ratio and *m*-xylene profile. The SOA parameters currently used in GEOS-Chem (HO_2/RO_2- independent) (Pye et al., 2010) and those obtained from this study (HO_2/RO_2-dependent) were used in this model. **Figure 3.14** presents the comparison between the predicted SOA mass using the VBS model and measured SOA mass in chamber, colored by the average HO_2/RO_2 ratios during the chamber experiments. Experiments with the HO_2/RO_2 ratio >1.5 show a decent agreement but those with lower HO_2/RO_2 show large a SOA overestimation when using HO_2/RO_2-independent parameters. However, when using HO_2/RO_2-dependent parameters, a great agreement was observed between estimated and measured SOA in chamber, indicating a significant improvement on SOA prediction when different HO_2/RO_2 conditions apply. Noting that the HO_2/RO_2-dependent parameters were obtained from final SOA yield and average HO_2/RO_2 ratio of each chamber experiment, and were applied into the course of the

experiment during which, HO_2/RO_2 ratio and *m*-xylene consumption are different at each time segments (every 5 minutes), 100% agreement between the final measured and estimated SOA formation was not expected. This indicates that it is important to consider both RO_2+RO_2 and HO_2+RO_2 pathways when predicting SOA formation from aromatic in the absence of NO_x, especially for regions with lower HO_2/RO_2 ratios.

3.3.5 SOA prediction in GEOS-Chem model

As discussed previously, *m*-xylene SOA might be potentially overestimated in lower HO_2/RO_2 regions because RO_2+RO_2 pathway, which has relatively lower SOA formation potential, is not considered in current model and tend to be more important at these regions. **Figure 3.15** presents the average global HO_2/RO_2 ratio during a typical summer month (July 2013) and shows the lower HO_2/RO_2 ratios in higher-populated regions such as east coast of America, southeast China, and India, where higher aromatic emissions are expected. This indicates the necessity of considering RO_2+RO_2 pathway as it has the largest impact on *m*-xylene SOA for the regions discussed. **Figure 3.16** and **3.17** show the *m*-xylene SOA using current parameters and the absolute difference when applying the parameters for the low HO_2/RO_2 case ($HO_2/RO_2 < 0.75$) from this study. Up to 0.05 ug/m^3 of *m*-xylene overestimation (up to 100%) for these regions was observed where the global SOA was originally estimated as 0.1 to 0.3 ug/m^3. The fact that the *m*-xylene SOA alone shows such a large overestimation indicates the importance of applying HO_2/RO_2 impact to all the other aromatic compounds and possible biogenic compounds.

3.3.6 Implications on chamber experiment design

Since HO_2/RO_2 significantly affects the competition between HO_2+RO_2 and RO_2+RO_2 and may explain the SOA yield variance between chambers, it needs to be controlled within a certain scenario if one wants to obtain a SOA yield curve or compare SOA at low NO_x conditions from different chambers. The initial condition of *m*-xylene and H_2O_2 is the key to control HO_2/RO_2 ratio. As a wide concentration range of initial VOC and H_2O_2 was used in chamber studies to investigate SOA formation at low NO_x conditions, it is important to control the H_2O_2/VOC ratio to control the HO_2/RO_2 ratio when designing chamber experiments. **Figure 3.18** shows a colormap of simulated HO_2/RO_2 ratio when using different concentrations of *m*-xylene (0 to 200 ppb) and H_2O_2 (0 to 8 ppm) using SAPRC11 mechanism(Carter and Heo, 2012) and such ranges are commonly within chamber capabilities. The HO_2/RO_2 is constant when the slope of H_2O_2 to *m*-xylene is constant and such slope defines the HO_2/RO_2 scenario. The colormap saturates when HO_2/RO_2 ratio is larger than 3 as almost all RO_2 radicals go to RO_2+HO_2 pathway.

In most of the chamber studies, constant concentration of H_2O_2 with various initial concentrations of SOA precursor were typically used (Li et al., 2015; Nakao et al., 2011) (scenario a) when obtaining the SOA yield curve for RO_2+HO_2 pathway. In this scenario, increasing *m*-xylene leads to the drop of HO_2/RO_2 ratio, increasing the impact from RO_2+RO_2 pathway thus the SOA yield curve from this scenario may not correctly represent absolute RO_2+HO_2 SOA yield. In scenario b, increasing H_2O_2 while keeping the *m*-xylene constant provides a valid method to study the impacts from RO_2+RO_2 and

RO_2+HO_2 pathways for a specific amount VOC consumption. In order to obtain the SOA yield from each pathway, the control of the contribution of each pathway (scenario c) when changing the initial H_2O_2 and *m*-xylene concentration at the same time is necessary. Noting that it is important to control HO_2/RO_2 within a valid range as when HO_2/RO_2 reaches a certain level, increasing HO_2/RO_2 would not increase the branching of HO_2+RO_2 as it is close to 100%.

Another way to control the HO_2/RO_2 ratio in chamber is to apply the surrogate mixture. In simple *m*-xylene+H_2O_2 system, the initial concentrations of *m*-xylene being 25, 50, 100 ppb and H_2O_2 being 1 ppm could lead to three different HO_2/RO_2 scenarios (**Figure 3.13**) thus to different SOA formation potential regions. However, when initially adding 1ppm surrogate into the system, the average HO_2/RO_2 ratios were located within 0.19 to 0.30 as the presence of the surrogate dilutes the impacts of varying initial VOC conditions within a certain range.

3.4 Conclusion

This study investigated the driving forces of the variance of SOA formation from *m*-xylene at very low NO_x conditions by evaluating the impacts of light intensity, NO_x off-gassing from chamber wall and H_2O_2. SOA yield from *m*-xylene at very low NO_x conditions was found to be strongly depending on the HO_2/RO_2 ratio in chamber. As the HO_2/RO_2 ratio increases, the SOA yield increases since HO_2/RO_2 ratio decrease the branching ratio of RO_2+RO_2 pathway, which forms more volatile products compared with RO_2+HO_2 pathway lowering the final SOA formation. A ROG surrogate mixture

was used to simulate urban atmosphere and it controlled the HO_2/RO_2 ratio to a relatively constant lower level (0.2 to 0.3) while varying the initial *m*-xylene concentrations. The measured SOA yield data from surrogate runs was consistent with the SOA yield curve at the lowest HO_2/RO_2 ratio (< 0.75). The light intensity impact was also investigated that higher light intensity increases the SOA formation rate but does not affect the final SOA yield from *m*-xylene at very low NO_x condition. NO_x off-gassing from the chamber wall is the only major NO_x source in chamber at very low NO_x conditions but the level of NO_x would not significantly affect SOA formation according to the sensitivity test based on the gas-phase chemistry.

The global surface HO_2/RO_2 ratio was modelled using GEOS-Chem. It was found that the higher populated regions with higher aromatic emissions normally has lower HO_2/RO_2 ratio, where the weakening impact of SOA from RO_2+RO_2 pathway is the largest. The *m*-xylene SOA can be overestimated by up to 100% in those regions. This indicates the importance of including RO_2+RO_2 pathway in current models when predicting SOA formation *m*-xylene and potentially other aromatic compounds.

Suggestions on chamber experiment design are provided when investigating SOA at very low NO_x conditions. A simulated HO_2/RO_2 ratio colormap is presented when using varied initial H_2O_2 and VOC concentrations. The HO_2/RO_2 ratio can be constrained constant when controlling the initial H_2O_2/VOC ratio. It is important to set the HO_2/RO_2 ratio constant to rule out the HO_2/RO_2 impact if one wants to obtain the SOA yield curve at known contribution of RO_2+RO_2 and RO_2+HO_2 pathways.

Tables & Figures

Table 3.1: Summary of very low NO_x experiments

Run	Time	k_1	NO_x Off-gassing	Tempe-rature	Initial VOC	H_2O_2	Consumed VOC	SOA Mass	Yield	OH	RO_2	HO_2
	min	/min	ppt/min	K	ppb	ppm	ug/m^3	ug/m^3		molecules/cm^3		
471A	710	0.15	0.81	301.8	105.8	0.4	168.0	17.3	10%	3.9E+5	4.0E+9	6.4E+8
471B	764	0.15	0.81	301.8	102.4	0.4	175.7	23.9	14%	4.0E+5	3.9E+9	6.5E+8
472B	695	0.15	0.81	301.8	111.2	1.0	241.8	48.6	20%	7.2E+5	4.1E+9	1.3E+9
472A	695	0.15	0.81	301.8	118.5	1.0	255.4	44.4	17%	6.8E+5	4.4E+9	1.2E+9
473B	732	0.15	0.81	301.8	108.0	2.0	299.0	91.2	30%	1.1E+6	2.7E+9	2.8E+9
473A	732	0.15	0.81	301.8	108.0	2.0	281.5	85.4	30%	1.1E+6	2.7E+9	2.8E+9
474B	710	0.15	0.81	301.7	105.0	4.0	310.5	130.2	42%	1.4E+6	1.8E+9	5.4E+9
474A	710	0.15	0.81	301.7	105.0	4.0	302.2	114.8	38%	1.4E+6	1.8E+9	5.4E+9
476A	721	0.15	0.81	301.7	53.8	1.0	141.0	36.0	26%	1.1E+6	1.9E+9	2.0E+9
476B	721	0.15	0.81	301.7	54.9	1.0	153.4	38.7	25%	1.0E+6	2.0E+9	1.9E+9
478B	634	0.15	0.80	301.5	26.3	1.0	75.2	21.3	28%	1.4E+6	9.4E+8	2.6E+9
750A	889	0.12	1.25	300.5	74.8	1.0	227.6	44.0	19%	7.9E+5	2.2E+9	1.6E+9
1180B	296	0.40	2.48	303.8	234.0	4.0	621.0	192.8	31%	2.8E+6	6.6E+9	6.2E+9
1209A	371	0.40	2.48	300.6	229.0	2.0	656.0	126.0	19%	1.9E+6	9.3E+9	2.9E+9
1209B	371	0.40	2.48	300.6	177.0	2.0	509.0	95.0	19%	2.2E+6	7.4E+9	3.3E+9
1212B	348	0.40	2.48	300.8	52.0	2.0	188.9	65.8	35%	3.9E+6	1.9E+9	6.2E+9
1212A	348	0.40	2.48	300.8	114.0	2.0	385.1	126.0	33%	2.8E+6	4.5E+9	4.4E+9
1248B	281	0.40	2.48	299.9	121.3	1.0	305.2	67.9	22%	1.8E+6	6.6E+9	2.0E+9
1424B	365	0.40	2.48	300.3	101.0	1.0	300.4	56.5	19%	2.0E+6	5.7E+9	2.2E+9
1860A	570	0.40	2.48	301.3	60.7	1.0	207.9	50.6	24%	2.9E+6	2.8E+9	3.2E+9
1860B	570	0.40	2.48	301.3	109.6	1.0	433.4	98.7	23%	1.9E+6	5.1E+9	2.4E+9
2563B	422	0.40	2.48	300.7	81.5	1.0	277.0	49.7	18%	2.3E+6	4.4E+9	2.7E+9

Table 3.1: Experiment summary (continue).

Run	Time	k_1	NO_x Off-gassing	Tempe-rature	Initial VOC	H_2O_2	Consumed VOC	SOA Mass	Yield	OH	RO_2	HO_2
	min	/min	ppt/min	K	ppb	ppm	ug/m^3	ug/m^3		molecules/cm^3		
2567A	431	0.40	2.48	301.0	72.8	1.0	231.9	45.7	20%	2.5E+6	3.9E+9	2.8E+9
2567B	431	0.40	2.48	301.1	72.7	1.0	234.6	42.2	18%	2.5E+6	3.8E+9	2.8E+9
2568B	374	0.40	2.48	301.1	28.0	1.0	115.9	24.9	22%	3.5E+6	1.9E+9	3.9E+9
2569B	392	0.40	2.48	300.2	20.8	1.0	73.2	14.9	20%	4.3E+6	1.1E+9	4.6E+9
2569A	392	0.40	2.48	300.3	47.1	1.0	157.7	24.9	16%	3.1E+6	2.5E+9	3.5E+9
2570B	348	0.40	2.48	300.7	11.0	1.0	45.4	8.2	18%	5.0E+6	5.9E+8	5.1E+9

Table 3.2: ROG surrogate mixture composition

Compound	acet-aldehyde	*m*-xylene	1,2,4-trimethyl-benzene	n-butane	2-methyl-propene	trans-2-butene	toluene
ppb/ppmC	38.76	4.35	4.22	76.8	5.72	2.38	12.02
Compound	1-pentene	ethylene	methyl-ethyl-ketone	propylene	2-methyl-butane	methylcyclo-pentane	isoprene
ppb/ppmC	2.61	11.91	14.22	2.68	37.72	21.34	1.51

Table 3.3: The Pearson Coefficient between SOA mass and *m*-xylene consumption with and without a third variable.

Original	Adding A Third Variable			
	k_1	NO Off-gassing	OH Exposure	HO_2/RO_2
86%	88%	88%	90%	98%

Table 3.4: SOA yield VBS parameters at different HO_2/RO_2 conditions.

HO_2/RO_2	RO_2+HO_2 branching		C^* (ug/m^3)			
	Slow† RO_2	Fast† RO_2	0.1	1	10	100
<.75	>70%	>20%	0	0	0.1584	0.1436
<1.5	>90%	>50%	0	0	0.25	0.1441
>1.5	>96%	>80%	.0378	0	0.2681	0.2087

†: slow: $k_{RO2+RO2}=8.8*10^{-13}$; fast: $k_{RO2+RO2}=1*10^{-11}$.

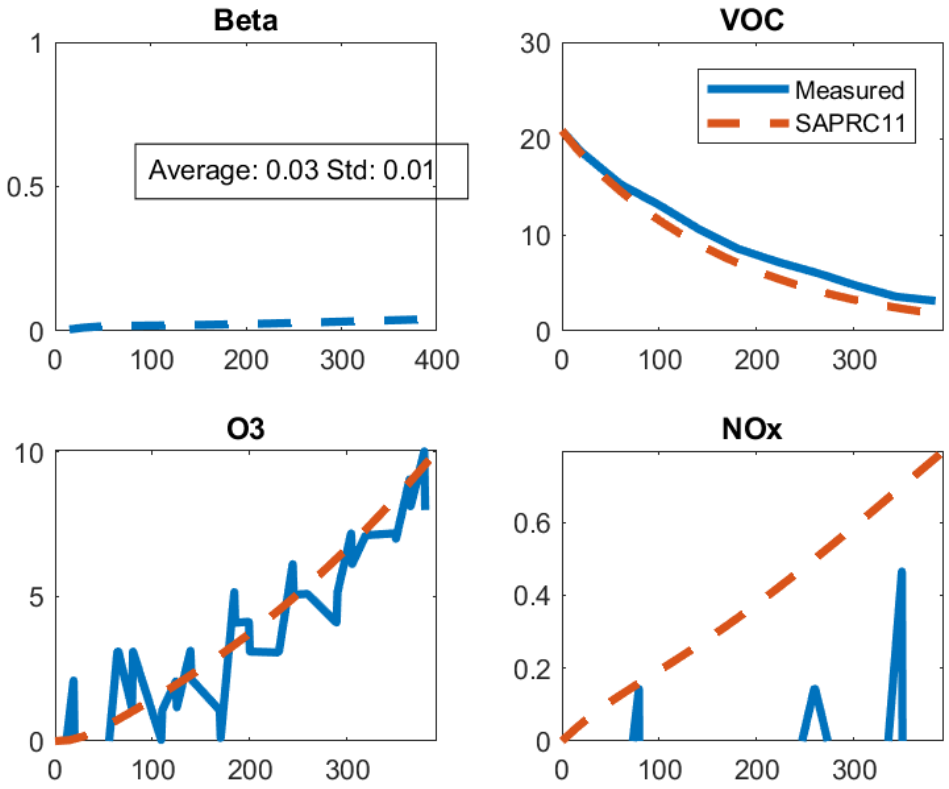

Figure 3.1: A typical profile of the branching ratio (beta) of RO_2+NO (considering RO_2+NO and RO_2+HO_2 pathways), VOC (ppb), O_3 (ppb) and NO_x (ppb) versus time (min) from SAPRC11 and experiment measurements

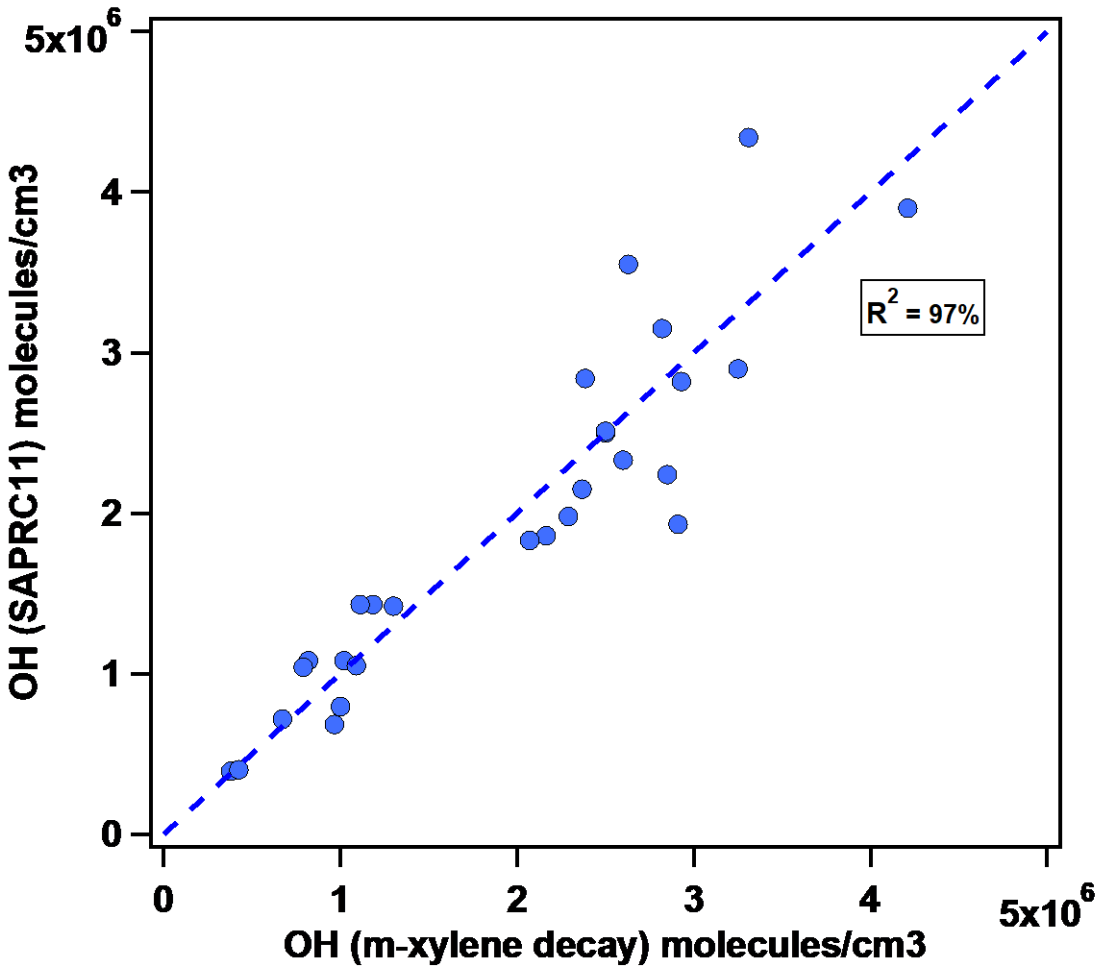

Figure 3.2: Averaged OH concentrations of each experiment from SAPRC11 and estimation of *m*-xylene decay

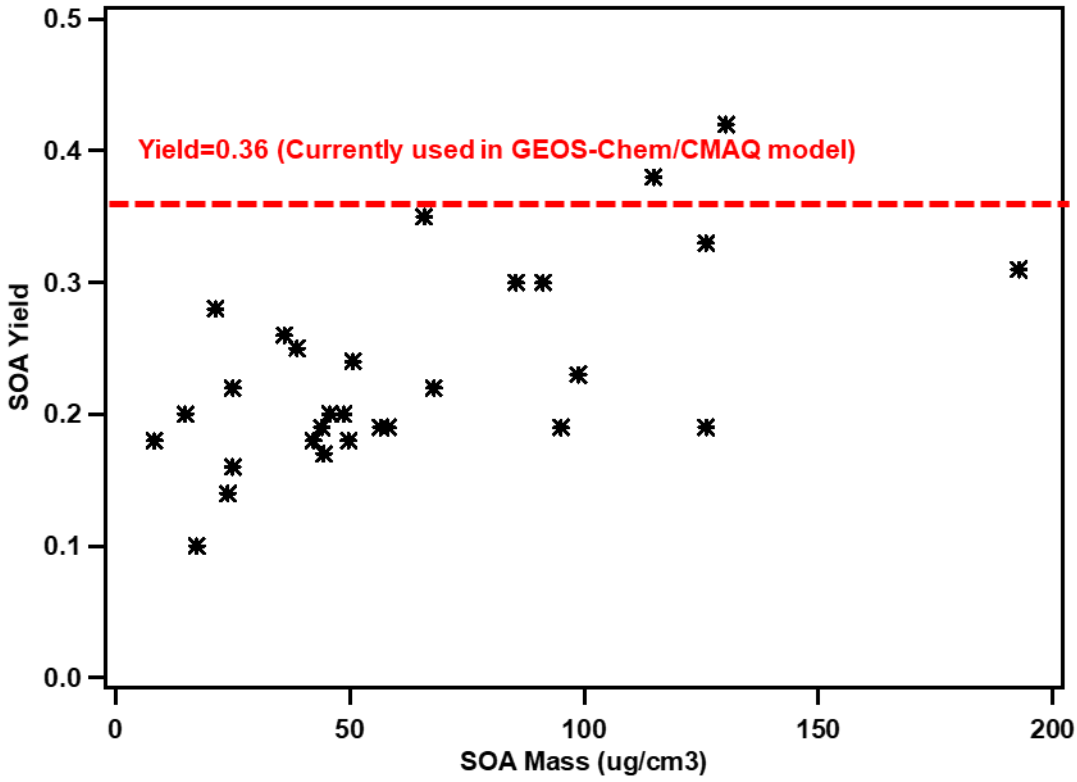

Figure 3.3: Final SOA Yields from *m*-xylene experiments at very low NO_x conditions

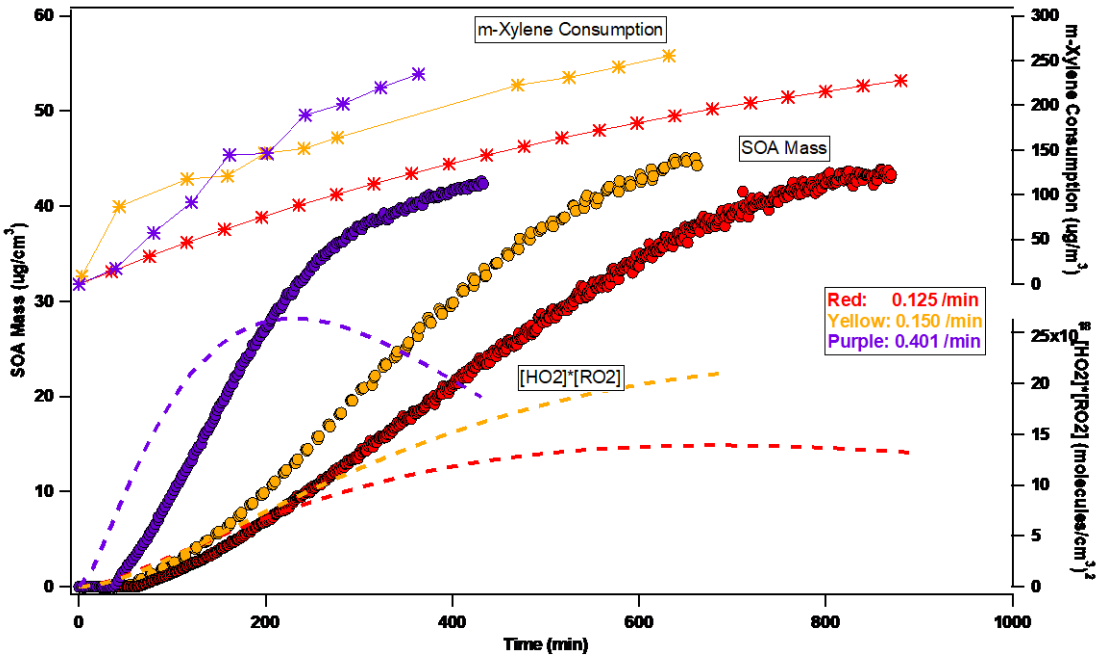

Figure 3.4: SOA formation, $[HO_2]^*[RO_2]$ and accumulative *m*-xylene consumption of three *m*-xylene experiments with different light intensities

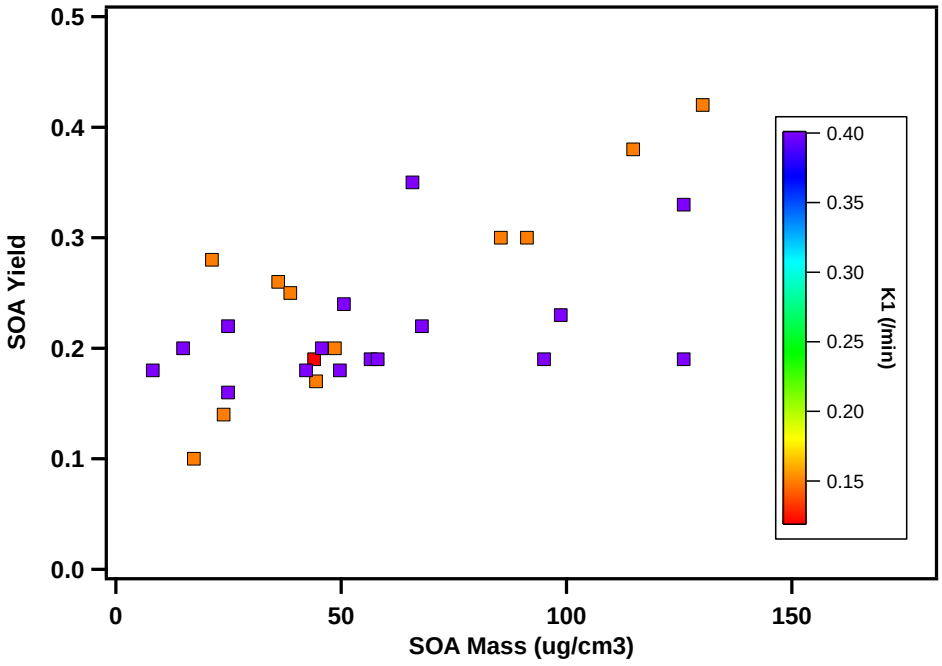

Figure 3.5: Final SOA yields from *m*-xylene experiments with no additional NO_x at different light intensities (represented by k_1)

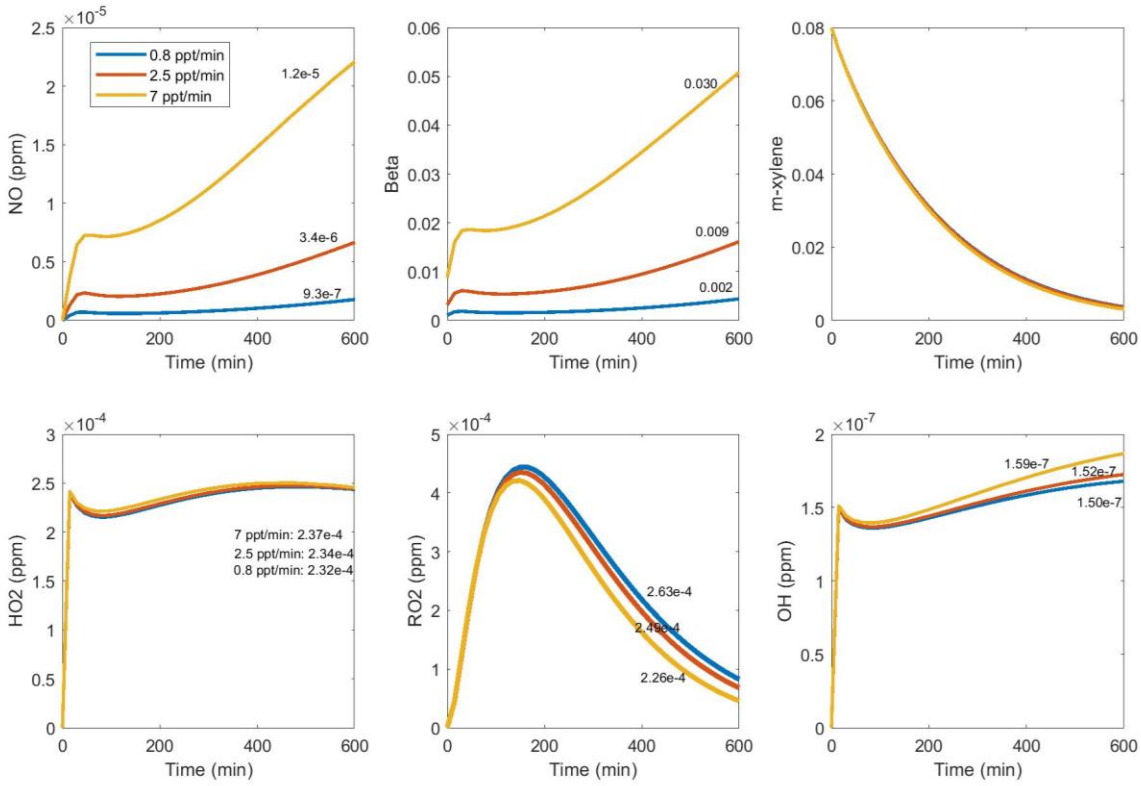

Figure 3.6: The sensitivity test of gas-phase chemistry simulation of a typical *m*-xylene and H_2O_2 experiment (80 ppb *m*-xylene and 2 ppm H_2O_2) with different NO_x off-gassing rates

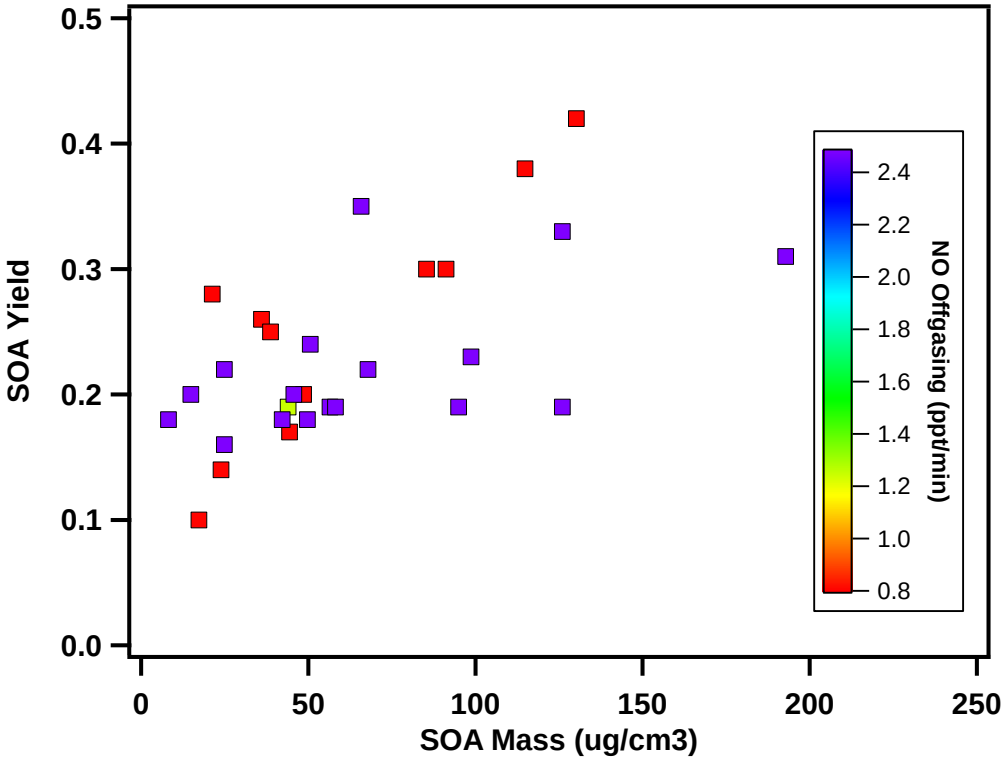

Figure 3.7: Final SOA yields from *m*-xylene experiments with no additional NO_x at different NO_x off-gassing from chamber wall (represented by NO_x off-gassing rate)

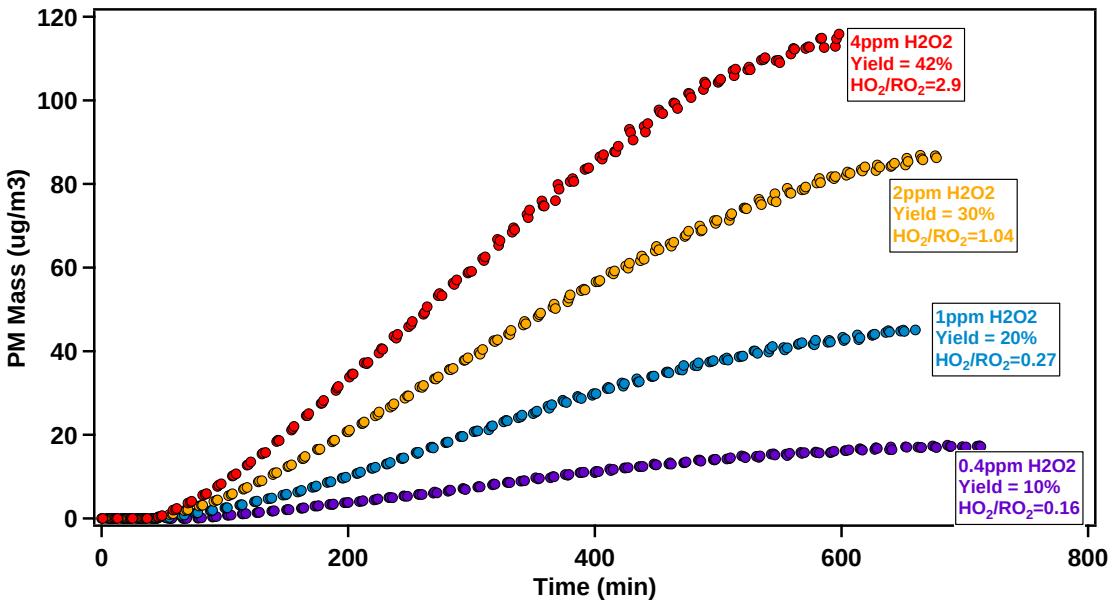

Figure 3.8: SOA formation from four *m*-xylene experiments with different initial concentrations of H_2O_2

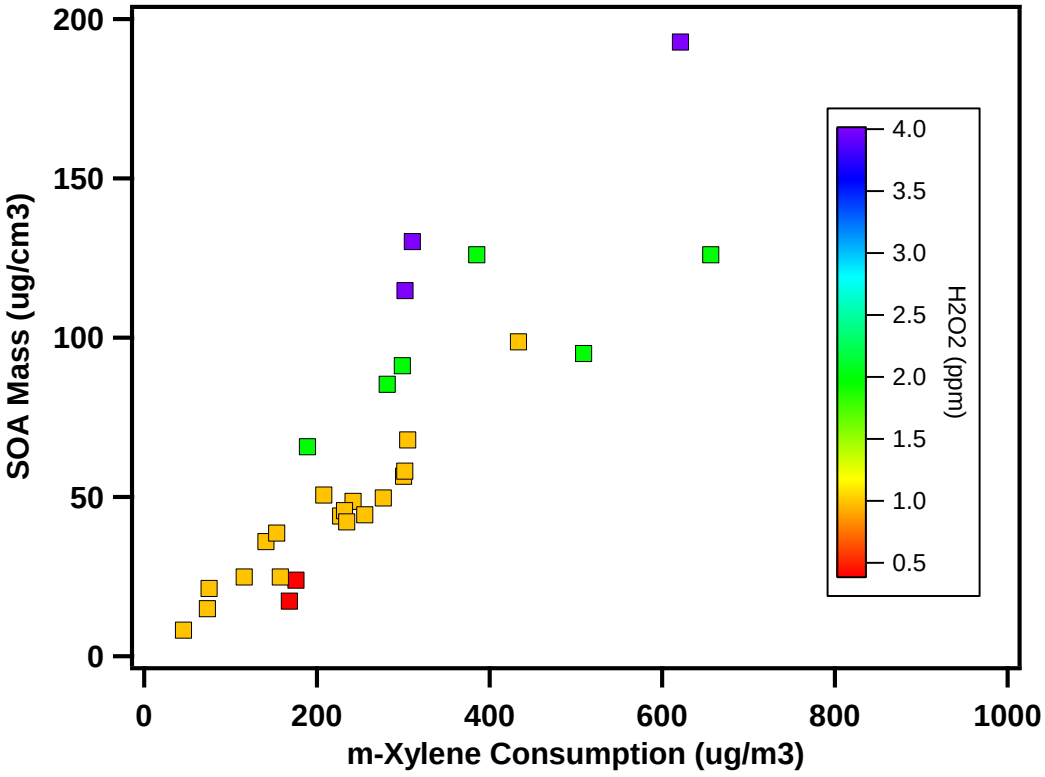

Figure 3.9: Final SOA mass and *m*-xylene consumption from *m*-xylene experiments with no additional NO_x with different initial H_2O_2

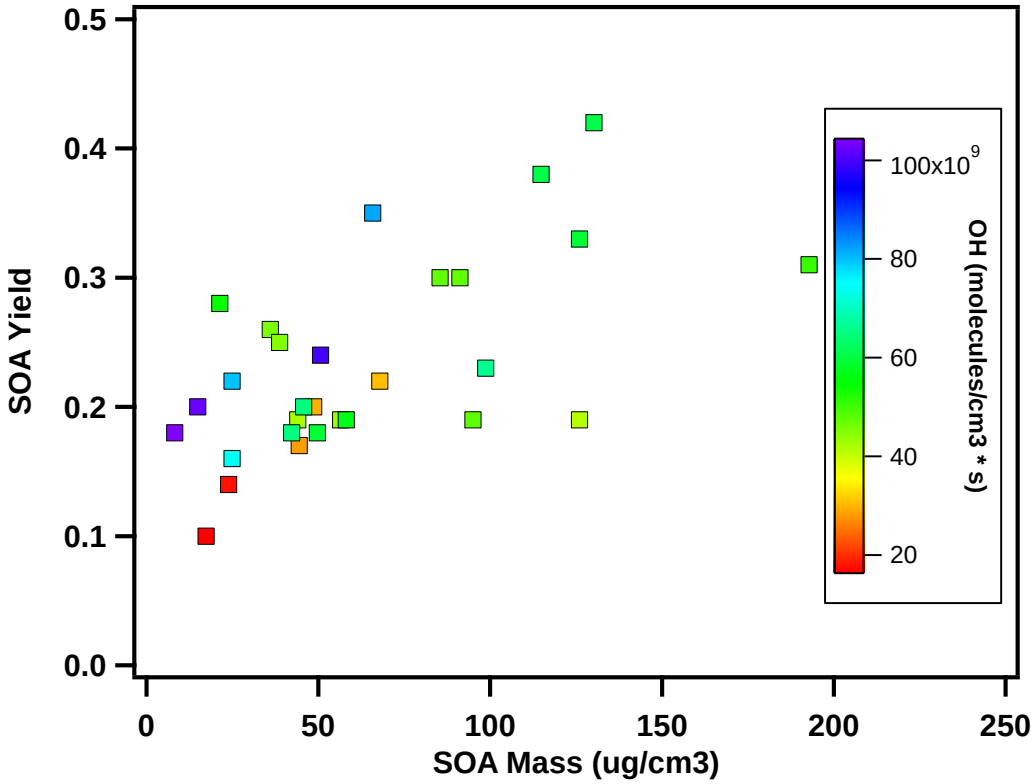

Figure 3.10: Final SOA yields from *m*-xylene experiments with no additional NO_x at different OH exposures (color represents OH exposure)

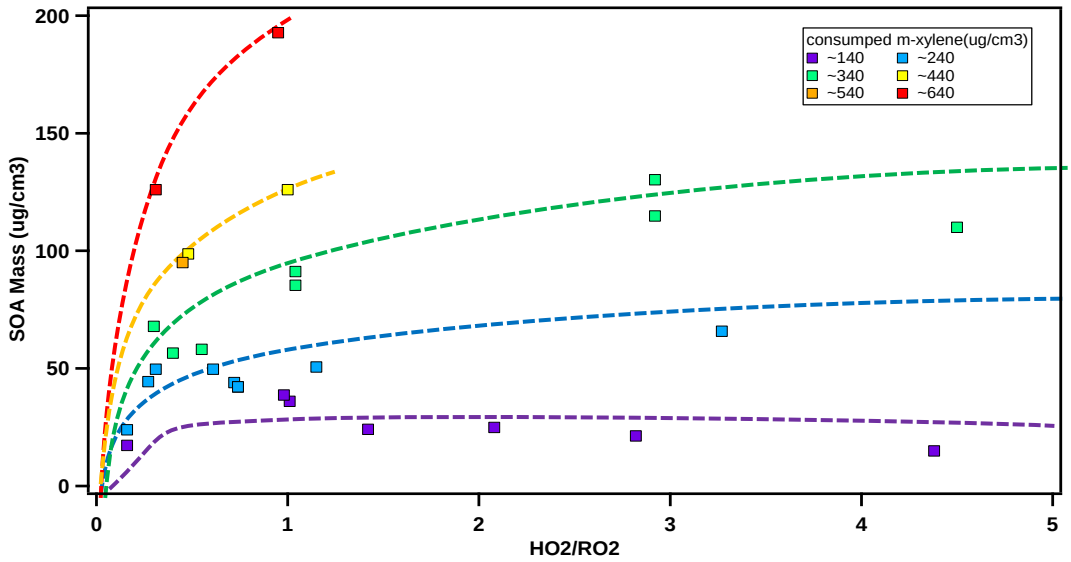

Figure 3.11: Final SOA formation with average HO_2/RO_2 for each experiment

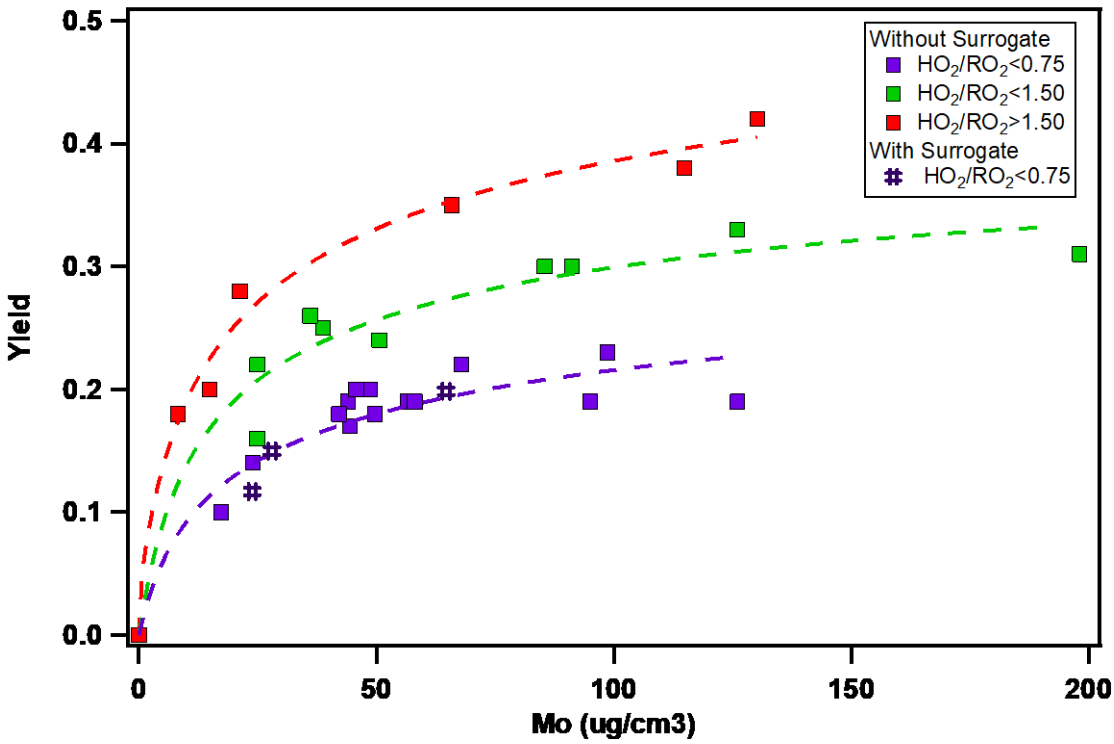

Figure 3.12: Final SOA yields from *m*-xylene experiments with no additional NO_x at different HO_2/RO_2

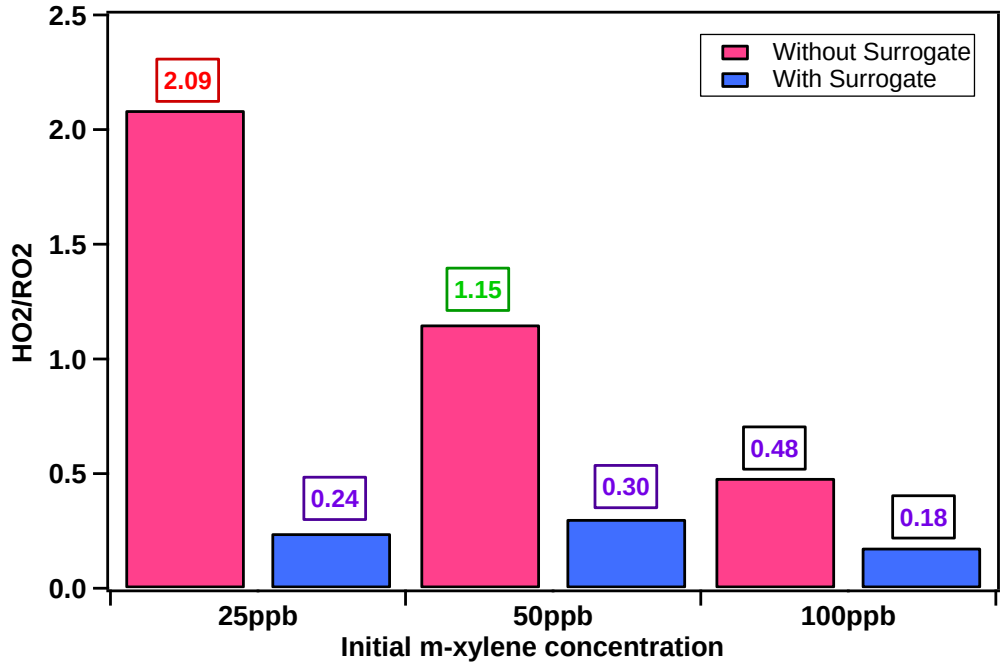

Figure 3.13: The average HO_2/RO_2 from *m*-xylene experiments with 1ppm H_2O_2 and 25, 50 and 100ppb initial *m*-xylene, with or without 1 ppmC surrogate mixture

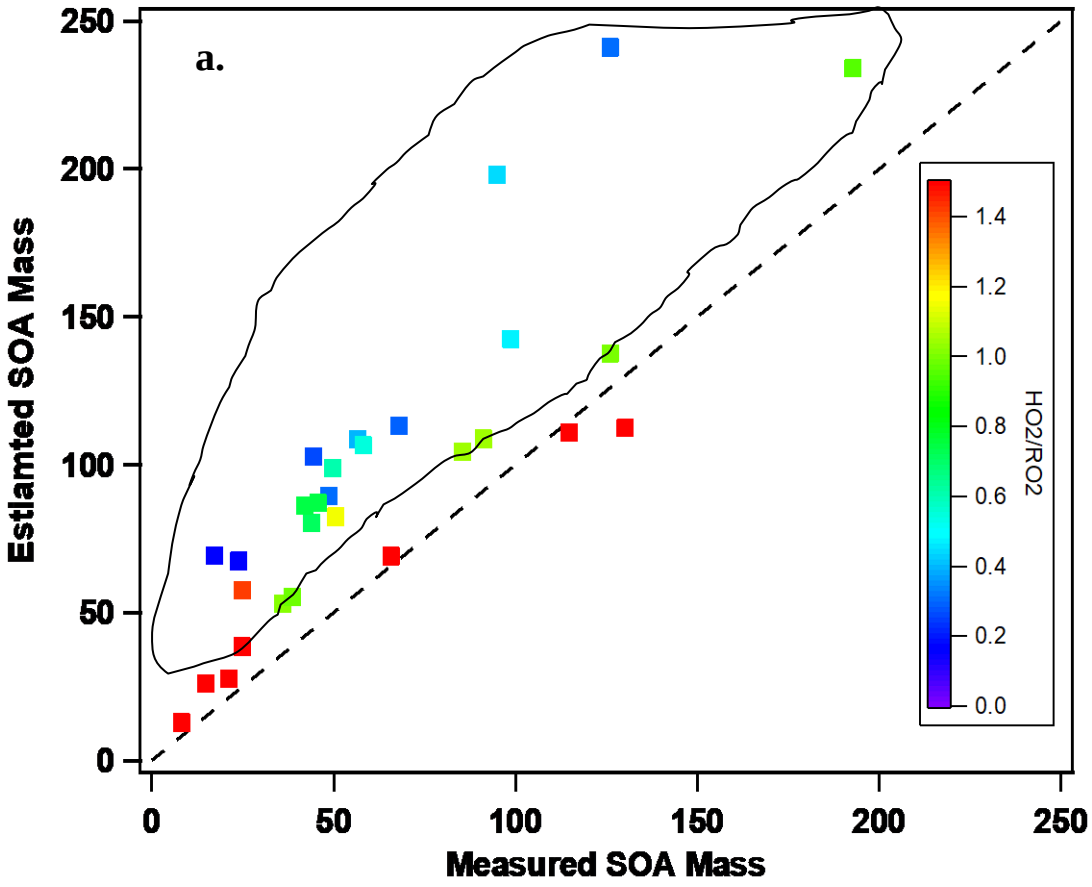

Figure 3.14: Estimated SOA using VBS parameters and measured SOA in chamber (a: HO_2/RO_2-independent parameters; b: HO_2/RO_2-dependent parameters)

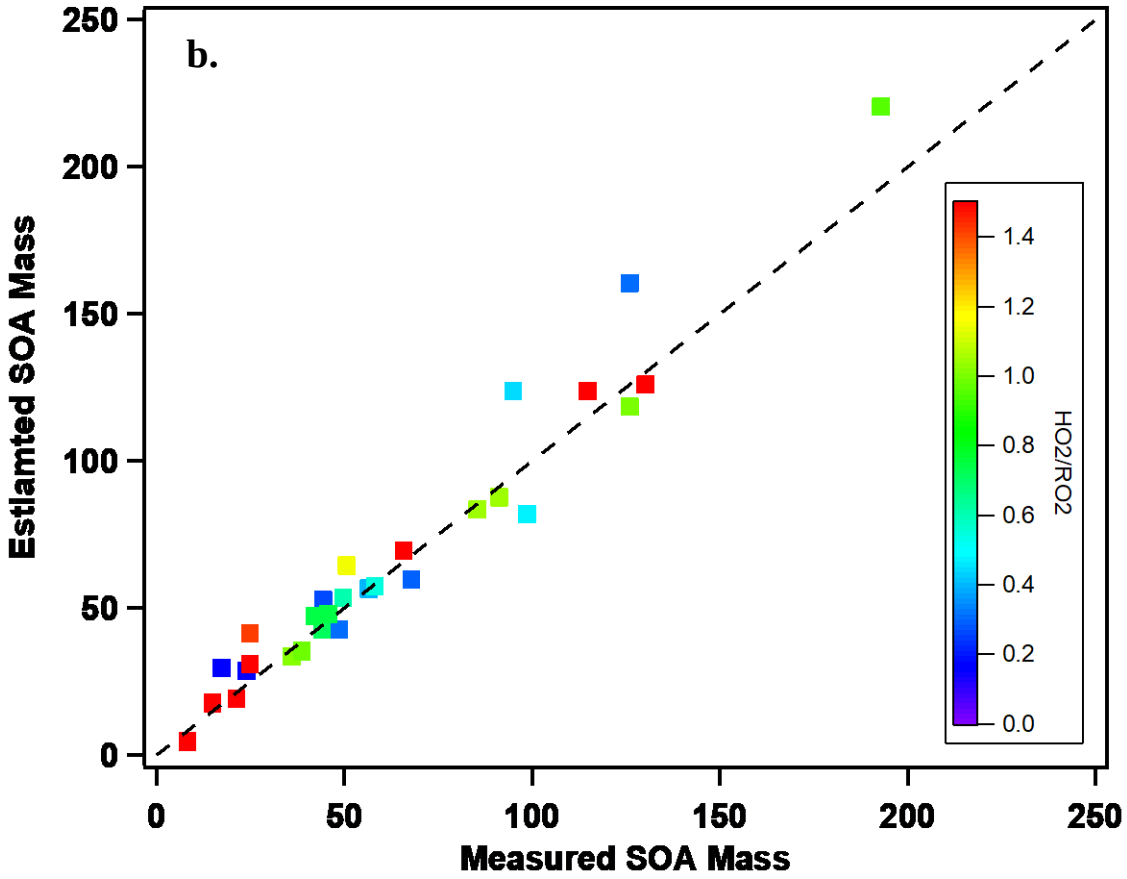

Figure 3.14: Estimated SOA using VBS parameters and measured SOA in chamber (continue.)

(a: HO_2/RO_2-independent parameters; b: HO_2/RO_2-dependent parameters)

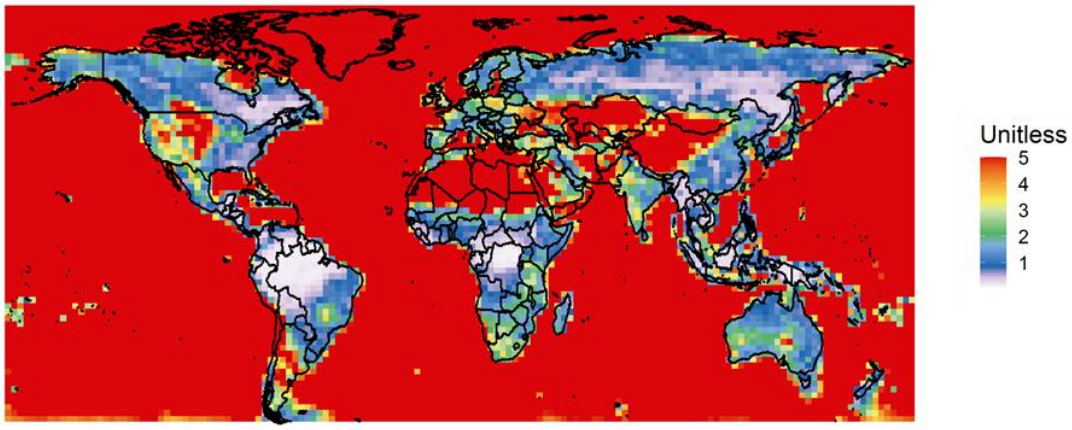

Figure 3.15: Monthly average global surface HO_2/RO_2

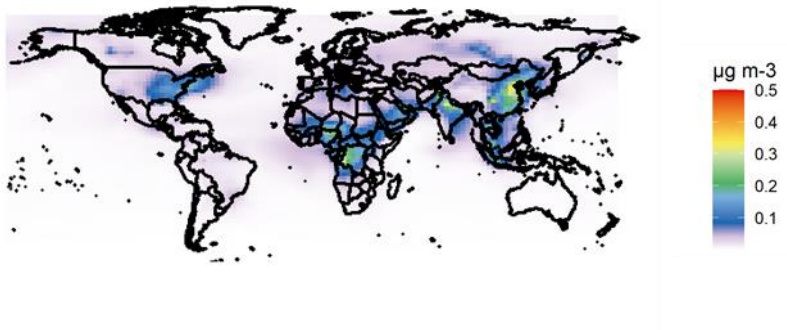

Figure 3.16: Monthly average global surface SOA from *m*-xylene from GEOS-Chem using previous low-NO_x parameters

Figure 3.17: Monthly average global surface SOA from *m*-xylene from GEOS-Chem using $HO_2/RO_2 < 0.75$ SOA parameters as low-NO_x parameters

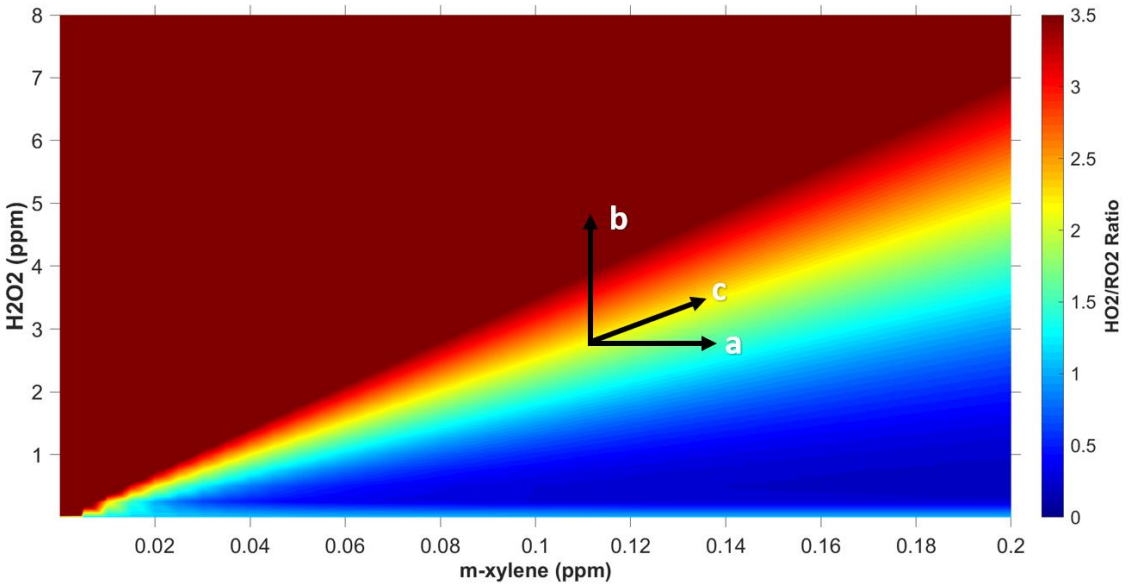

Figure 3.18: The average HO_2/RO_2 ratio heatmap with initial H_2O_2 (0 to 8 ppm) and *m*-xylene (0 to 200 ppb) in chamber

Reference

Berndt, T., Scholz, W., Mentler, B., Fischer, L., Herrmann, H., Kulmala, M., Hansel, A., 2018. Accretion Product Formation from Self- and Cross-Reactions of RO2 Radicals in the Atmosphere. Angew. Chemie - Int. Ed. 57, 3820–3824. https://doi.org/10.1002/anie.201710989

Carlton, A.G., Bhave, P. V., Napelenok, S.L., Edney, E.O., Sarwar, G., Pinder, R.W., Pouliot, G.A., Houyoux, M., 2010. Model representation of secondary organic aerosol in CMAQv4.7. Environ. Sci. Technol. 44, 8553–8560. https://doi.org/10.1021/es100636q

Carter, W.P.L., Cocker, D.R., Fitz, D.R., Malkina, I.L., Bumiller, K., Sauer, C.G., Pisano, J.T., Bufalino, C., Song, C., 2005. A new environmental chamber for evaluation of gas-phase chemical mechanisms and secondary aerosol formation. Atmos. Environ. https://doi.org/10.1016/j.atmosenv.2005.08.040

Carter, W.P.L., Heo, G., 2012. Development of revised SAPRC aromatics mechanisms 77, 404–414.

Cocker, D.R., Flagan, R.C., Seinfeld, J.H., 2001. State-of-the-art chamber facility for studying atmospheric aerosol chemistry. Environ. Sci. Technol. 35, 2594–2601. https://doi.org/10.1021/es0019169

Corbin, J.C., Peng, W., Yang, J., Sommer, D.E., Trivanovic, U., Kirchen, P., Miller, J.W., Rogak, S., Cocker, D.R., Smallwood, G.J., Lobo, P., Gagné, S., 2020. Characterization of particulate matter emitted by a marine engine operated with liquefied natural gas and diesel fuels. Atmos. Environ. 220. https://doi.org/10.1016/j.atmosenv.2019.117030

Docherty, K.S., Ziemann, P.J., 2003. Effects of Stabilized Criegee Intermediate and OH Radical Scavengers on Aerosol Formation from Reactions of β-Pinene with O3. Aerosol Sci. Technol. 37, 877–891. https://doi.org/10.1080/02786820300930

Donahue, N.M., Robinson, A.L., Stanier, C.O., Pandis, S.N., 2006. Coupled partitioning, dilution, and chemical aging of semivolatile organics. Environ. Sci. Technol. 40, 2635–2643. https://doi.org/10.1021/es052297c

Farina, S.C., Adams, P.J., Pandis, S.N., 2010. Modeling global secondary organic aerosol formation and processing with the volatility basis set: Implications for anthropogenic secondary organic aerosol. J. Geophys. Res. Atmos. 115. https://doi.org/10.1029/2009JD013046

Hallquist, M., Wenger, J.C., Baltensperger, U., Rudich, Y., Simpson, D., Claeys, M., Dommen, J., Donahue, N.M., George, C., Goldstein, A.H., Hamilton, J.F., Herrmann, H., Hoffmann, T., Iinuma, Y., Jang, M., Jenkin, M.E., Jimenez, J.L., Kiendler-Scharr, A., Maenhaut, W., McFiggans, G., Mentel, T.F., Monod, A., Prévôt, A.S.H.H., Seinfeld, J.H., Surratt, J.D., Szmigielski, R., Wildt, J., 2009. The formation, properties and impact of secondary organic aerosol: Current and emerging issues. Atmos. Chem. Phys. 9, 5155–5236. https://doi.org/10.5194/acp-9-5155-2009

Henry, K.M., Donahue, N.M., 2011. Effect of the OH radical scavenger hydrogen peroxide on secondary organic aerosol formation from α-pinene ozonolysis. Aerosol Sci. Technol. 45, 696–700. https://doi.org/10.1080/02786826.2011.552926

Jimenez, J.L., Canagaratna, M.R., Donahue, N.M., Prevot, A.S.H.H., Zhang, Q., Kroll, J.H., DeCarlo, P.F., Allan, J.D., Coe, H., Ng, N.L., Aiken, A.C., Docherty, K.S., Ulbrich, I.M., Grieshop, A.P., Robinson, A.L., Duplissy, J., Smith, J.D., Wilson, K.R., Lanz, V.A., Hueglin, C., Sun, Y.L., Tian, J., Laaksonen, A., Raatikainen, T., Rautiainen, J., Vaattovaara, P., Ehn, M., Kulmala, M., Tomlinson, J.M., Collins, D.R., Cubison, M.J., Dunlea, J., Huffman, J.A., Onasch, T.B., Alfarra, M.R., Williams, P.I., Bower, K., Kondo, Y., Schneider, J., Drewnick, F., Borrmann, S., Weimer, S., Demerjian, K., Salcedo, D., Cottrell, L., Griffin, R., Takami, A., Miyoshi, T., Hatakeyama, S., Shimono, A., Sun, J.Y., Zhang, Y.M., Dzepina, K., Kimmel, J.R., Sueper, D., Jayne, J.T., Herndon, S.C., Trimborn, A.M., Williams, L.R., Wood, E.C., Middlebrook, A.M., Kolb, C.E., Baltensperger, U., Worsnop, D.R., Dunlea, E.J., Huffman, J.A., Onasch, T.B., Alfarra, M.R., Williams, P.I., Bower, K., Kondo, Y., Schneider, J., Drewnick, F., Borrmann, S., Weimer, S., Demerjian, K., Salcedo, D., Cottrell, L., Griffin, R., Takami, A., Miyoshi, T., Hatakeyama, S., Shimono, A., Sun, J.Y., Zhang, Y.M., Dzepina, K., Kimmel, J.R., Sueper, D., Jayne, J.T., Herndon, S.C., Trimborn, A.M., Williams, L.R., Wood, E.C., Middlebrook, A.M., Kolb, C.E., Baltensperger, U., Worsnop, D.R., 2009. Evolution of Organic Aerosols in the Atmosphere. Science (80-.). 326, 1525–1529. https://doi.org/10.1126/science.1180353

Kacarab, M., 2013. Impacts of Controlling Reactivity and Temperature on Advanced Study of Secondary Organic Aerosol Formation. University of California, Riverside.

Kanakidou, M., Seinfeld, J.H., Pandis, S.N., Barnes, I., Dentener, F.J., Facchini, M.C., Van Dingenen, R., Ervens, B., Nenes, A., Nielsen, C.J., Swietlicki, E., Putaud, J.P., Balkanski, Y., Fuzzi, S., Horth, J., Moortgat, G.K., Winterhalter, R., Myhre, C.E.L., Tsigaridis, K., Vignati, E., Stephanou, E.G., Wilson, J., 2005. Organic aerosol and global climate modelling: a review. Atmos. Chem. Phys. 5, 1053–1123. https://doi.org/10.5194/acp-5-1053-2005

Keywood, M.D., Kroll, J.H., Varutbangkul, V., Bahreini, R., Flagan, R.C., Seinfeld, J.H., 2004. Secondary organic aerosol formation from cyclohexene ozonolysis: Effect of

OH scavenger and the role of radical chemistry. Environ. Sci. Technol. 38, 3343–3350. https://doi.org/10.1021/es049725j

Kroll, J.H., Seinfeld, J.H., 2008. Chemistry of secondary organic aerosol: Formation and evolution of low-volatility organics in the atmosphere. Atmos. Environ. 42, 3593–3624. https://doi.org/10.1016/j.atmosenv.2008.01.003

Kwan, A.J., Chan, A.W.H., Ng, N.L., Kjaergaard, H.G., Seinfeld, J.H., Wennberg, P.O., 2012. Peroxy radical chemistry and OH radical production during the NO3-initiated oxidation of isoprene. Atmos. Chem. Phys. 12, 7499–7515. https://doi.org/10.5194/acp-12-7499-2012

Li, L., Tang, P., Cocker, D.R., 2015. Instantaneous nitric oxide effect on secondary organic aerosol formation from m-xylene photooxidation. Atmos. Environ. 119, 144–155. https://doi.org/10.1016/j.atmosenv.2015.08.010

Li, W., Li, L., Chen, C.-L., Kacarab, M., Peng, W., Price, D., Xu, J., Cocker, D.R., 2018. Potential of select intermediate-volatility organic compounds and consumer products for secondary organic aerosol and ozone formation under relevant urban conditions. Atmos. Environ. 178. https://doi.org/10.1016/j.atmosenv.2017.12.019

Liu, X., Zhang, W., Huang, M., Wang, Z., Hao, L., Zhao, W., 2009. Effect of illumination intensity and light application time on secondary organic aerosol formation from the photooxidation of α-pinene. J. Environ. Sci. 21, 447–451. https://doi.org/10.1016/S1001-0742(08)62290-1

Malloy, Q.G.J., Nakao, S., Qi, L., Austin, R., Stothers, C., Hagino, H., Cocker, D.R., 2009. Real-Time aerosol density determination utilizing a modified scanning mobility particle sizer aerosol particle mass analyzer system. Aerosol Sci. Technol. https://doi.org/10.1080/02786820902832960

Myhre, G., Shindell, D., Bréon, F.-M.F.-M., Collins, W., Fuglestvedt, J.S., Huang, J., Koch, D., Lamarque, J.-F.J.-F., Lee, D., Mendoza, B., Nakajima, T., Robock, A., Stephens, G., Takemura, T., Zhan, H., Zhang, H., 2013. Anthropogenic and Natural Radiative Forcing, in: Intergovernmental Panel on Climate Change (Ed.), Climate Change 2013 - The Physical Science Basis. Cambridge University Press, Cambridge, pp. 659–740. https://doi.org/10.1017/CBO9781107415324.018

Na, K., Sawant, A.A., Song, C., Cocker, D.R., 2004. Primary and secondary carbonaceous species in the atmosphere of Western Riverside County, California. Atmos. Environ. https://doi.org/10.1016/j.atmosenv.2003.11.023

Nakao, S., Clark, C., Tang, P., Sato, K., Cocker, D., 2011. Secondary organic aerosol formation from phenolic compounds in the absence of NOx. Atmos. Chem. Phys. 11, 10649–10660. https://doi.org/10.5194/acp-11-10649-2011

Nakao, S., Liu, Y., Tang, P., Chen, C.L., Zhang, J., Cocker, D.R., 2012. Chamber studies of SOA formation from aromatic hydrocarbons: Observation of limited glyoxal uptake. Atmos. Chem. Phys. https://doi.org/10.5194/acp-12-3927-2012

Ng, N.L., Kroll, J.H., Chan, A.W.H., Chhabra, P.S., Flagan, R., Seinfeld, J.H., 2007. Secondary organic aerosol formation from m-xylene, toluene, and benzene. Atmos. Chem. Phys. 7, 3909–3922. https://doi.org/10.5194/acp-7-3909-2007

Odum, J.R., Hoffmann, T., Bowman, F., Collins, D., Flagan, R.C., Seinfeld, J.H., 1996. Gas/particle partitioning and secondary organic aerosol yields. Environ. Sci. Technol. https://doi.org/10.1021/es950943+

Orlando, J.J., Tyndall, G.S., 2012. Laboratory studies of organic peroxy radical chemistry: An overview with emphasis on recent issues of atmospheric significance. Chem. Soc. Rev. 41, 6294–6317. https://doi.org/10.1039/c2cs35166h

Peng, Z., Lee-Taylor, J., Orlando, J.J., Tyndall, G.S., Jimenez, J.L., 2019. Organic peroxy radical chemistry in oxidation flow reactors and environmental chambers and their atmospheric relevance. Atmos. Chem. Phys. 19, 813–834. https://doi.org/10.5194/acp-19-813-2019

Pye, H.O.T., Chan, A.W.H., Barkley, M.P., Seinfeld, J.H., 2010. Global modeling of organic aerosol: The importance of reactive nitrogen (NOx and NO3). Atmos. Chem. Phys. 10, 11261–11276. https://doi.org/10.5194/acp-10-11261-2010

Schervish, M., Donahue, N.M., 2020. Peroxy radical chemistry and the volatility basis set. Atmos. Chem. Phys. 20, 1183–1199. https://doi.org/10.5194/acp-20-1183-2020

Song, C., Na, K., Warren, B., Malloy, Q., Cocker, D.R., 2007a. Secondary organic aerosol formation from m-xylene in the absence of NOx. Environ. Sci. Technol. 41, 7409–7416. https://doi.org/10.1021/es070429r

Song, C., Na, K., Warren, B., Malloy, Q., Cocker, D.R., 2007b. Secondary organic aerosol formation from m-xylene in the absence of NOx. Environ. Sci. Technol. 41, 7409–7416. https://doi.org/10.1021/es070429r

Swinscow, T.D. V, 1976. Statistics at square one. Ninth Edition. Br. Med. J. https://doi.org/10.1136/bmj.1.6020.1262

Warren, B., Song, C., Cocker, D.R., 2008. Light intensity and light source influence on secondary organic aerosol formation for the m-xylene/NOx photooxidation system. Environ. Sci. Technol. 42, 5461–5466. https://doi.org/10.1021/es702985n

Zhao, H., Che, H., Zhang, X., Ma, Y., Wang, Yangfeng, Wang, H., Wang, Yaqiang, 2013. Characteristics of visibility and particulate matter (PM) in an urban area of Northeast China. Atmos. Pollut. Res. https://doi.org/10.5094/APR.2013.049

Ziemann, P.J., 2002. Evidence for low-volatility diacyl peroxides as a nucleating agent and major component of aerosol formed from reactions of O3 with cyclohexene and homologous compounds. J. Phys. Chem. A 106, 4390–4402. https://doi.org/10.1021/jp012925m

Chapter 4 : Organic Aerosol (SOA) Formation from Aromatic Compounds: The Dependence on The Branching Ratio (β) of RO_2+NO Pathway

4.1 Introduction

Organic aerosol (OA) accounts for 20% to 90% of sub-micro aerosol in the atmosphere. It plays an important role in environmental and health issues such as air quality, visibility, climate change and lung-related diseases (Corbin et al., 2020; Jimenez et al., 2009; Myhre et al., 2013; Zhao et al., 2013). Secondary organic aerosol (SOA), formed from atmospheric oxidation reactions of various volatile organic compounds, contributes up to 70% of the OA (Kanakidou et al., 2005). Aromatic compounds, as one category of the most important anthropogenic SOA precursors, were estimated to contribute up to 50% to 70% of total SOA formation in urban atmosphere (Na et al., 2004). It was modelled that the total annual emissions of BTX compounds (benzene, toluene and xylene) are about 18 Tg/yr and xylene emission accounts for about 30%.

The SOA formation in atmosphere is initiated by three major oxidants, hydroxyl radical (OH), nitrate radical (NO_3) and ozone (O_3) and it is influenced by different environmental parameters such as NO_x level, temperature, relative humidity and acidity (Cao and Jang, 2008; Li et al., 2015; Nakao et al., 2011; Ng et al., 2007; Qi et al., 2010; Song et al., 2005). It was shown that NO_x, which is another important anthropogenic emission, impacts SOA formation from the photo-oxidation of aromatic compounds. Higher SOA yield was observed in lower NO_x conditions. The reactions between organic peroxy radicals (RO_2) and hydroperoxyl radicals (HO_2) are believed to be the dominant

pathway on SOA formation in low NO_x condition thus the products, organic hydroperoxides, are less volatile than the organic nitrate from RO_2+NO pathway, which is the major pathway at high-NO_x conditions (Kroll and Seinfeld, 2008).

The two-product model and volatility basis set (VBS) are commonly used to characterize SOA formation from a precursor under certain conditions (Donahue et al., 2006; Odum et al., 1997, 1996). The SOA parameters for two-product model or VBS for RO_2+NO and RO_2+HO_2 pathways can be obtained from high- and low-NO_x chamber studies. Current global transport models use those parameters of the two pathways as well as the branching ratio of the RO_2+NO pathway (β) to account for the NO_x effects when predicting SOA formation from aromatic compounds (Carlton et al., 2010; Pye et al., 2010). The β is calculated with **Equation 4.1**, where k_{RO_2+NO} and $k_{RO_2+HO_2}$ are the reaction constants of RO_2 with NO and HO_2, respectively. A large range of anthropogenic SOA prediction (0.05 to 9.7 Tg/year) was reported (Farina et al., 2010; Guillaume et al., 2007; Tsigaridis and Kanakidou, 2003). The SOA parameters might contribute to such large uncertainties because the traditional high- and low-NO_x experiments may not accurately represent those two pathways and β needs to be evaluated for those experiments.

$$\beta = \frac{k_{RO_2+NO}[NO]}{k_{RO_2+HO_2}[HO_2]+k_{RO_2+NO}[NO]} \qquad \textbf{Equation 4.1}$$

Multiple chamber studies have investigated the SOA formation from aromatic compounds using different indicators to represent the NO_x conditions in chamber. Song *et al*. observed two distinct SOA yield trends from OH initiated *m*-xylene experiments

with different ratios of initial hydrocarbon (HC) to NO_x (high yield when $HC/NO_x > 8$ and low yield when $HC/NO_x < 5.5$). Ng *et al*. simulated high- and low-NO_x conditions in chamber with the injection of HONO and H_2O_2, respectively, and reported aromatic compounds SOA yield parameters for RO_2+NO and RO_2+HO_2 pathways using the two-product model. It was suggested that $[NO]/[HO_2]$ be a more appropriate measure of NO_x as it represents the fate of RO_2 which is important in SOA formation. However, the $[NO]/[HO_2]$ ratio does not explicitly show the competition of RO_2+NO and RO_2+HO_2 pathways and it needs to be combined with the reaction constants of those two pathways to obtain the branching ratio (β). While HONO or low initial HC/NO_x were used to represent high-NO_x conditions in chamber, it may not represent the absolute RO_2+NO pathway because RO_2+HO_2 may still contribute to SOA formation if β cannot be controlled at 1. Thus, more investigation is needed to evaluate the branching conditions in chamber for those experiments to verify the accuracy of the SOA parameters obtained from those experiments.

Besides the SOA parameters for those two pathways ($\beta = 1$ and $\beta = 0$), the method of estimating SOA parameters for intermediate β may also become one of the sources of the uncertainties in model predictions. Lane *et al*. proposed an approach of determining the mass yield coefficients, α, of four products for intermediate β by linearly combining the mass yield coefficients from each pathway with β for products with the same effective saturation pressure (Lane et al., 2008). This approach is also currently used in global models (e.g. GEOS-Chem) to represent NO_x impact on SOA (Henze et al., 2010; Pye et

al., 2019). However, no experimental data is available to verify this approach thus it is important to investigate the SOA yield parameters at different β in chamber.

To the best of my knowledge, there has not been any reported experimental study on the relationship between the SOA yield and branching ratio. In this study, a novel approach of controlling β at 1 during the whole course of chamber experiments was developed to simulate RO_2+NO pathway without the significant contribution from other pathways. The SOA yield parameters for this pathway were developed. Since β is an important indicator of NO_x conditions, the global surface β was estimated using GEOS-Chem and four β scenarios were observed. By controlling β to simulate the daytime β profile of the four scenarios, the *m*-xylene SOA formation was investigated.

4.2 Method

The University of California, Riverside (UCR) dual-90m^3 Teflon indoor smog chambers (details were described elsewhere (Carter et al., 2005)) were used for both traditional and controlled-β chamber experiments (**Table 4.1**), which were conducted at dry conditions (RH < 0.1%), 300 ± 1 K with no inorganic- or organic-seed presence. The chamber reactors were maintained at a positive differential pressure of ~0.015" H_2O compared to the enclosure to avoid the dilution. 272 UV black lights (115W Sylvania 350BL, NO_2 photolysis rate at 0.4 min^{-1}) were used for photooxidation. For controlled-β experiments, *m*-xylene and H_2O_2 were injected before the black lights were turned on and NO was continuously injected throughout the experiments at different rates to maintain β at a constant value. The atmosphere chemistry mechanism, SAPRC11, was used to simulate gas-phase chemistry in the chamber (Carter et al., 2012). It was used to design

the NO injection rate before experiments and to estimate the concentration of gas-phase species such as HO_2, RO_2 and NO after experiments. *m*-Xylene concentration was measured with an Agilent 6980 (Palo Alto, CA) gas chromatographs equipped with flame ionization detectors (GC-FID). NO_x and O_3 concentrations were measured with a Thermal Environmental Instruments Model 42C chemiluminescence NO_x analyzer and a Dasibi Environmental Corp. Model 1003-AH O_3 analyzer. Particle concentration was measured using a home-built dual scanning mobility particle sizer and particle wall loss was corrected using the method as described by (Cocker et al., 2001). A Kanomax aerosol particle mass analyzer (APM) (described in Malloy *et al*. (Malloy et al., 2009)) was used to measure the density of SOA.

The volatility basis set (VBS) parameters using **Equation 4.2** (Donahue et al., 2006) were developed for β = 1 condition, to represent the RO_2+NO pathway. C_{OA} is the total SOA mass, C_i^* is the effect saturation concentration of each of the four products (0.1, 1, 10, 100 ug/m^3) and C_i is the total concentration of a product in gas- and particle-phase,. For β = 0 scenario, the three sets HO_2/RO_2-dependent parameters discussed in Chapter 3 to represent the combination of RO_2+HO_2 and RO_2+RO_2 pathways. For intermediate β, the amount of hydrocarbon reacting through RO_2+HO_2 and RO_2+RO_2 pathways (low NO_x) and RO_2+NO pathway (high-NO_x) were calculated using **Equation 4.3** and **4.4**. The mass coefficient α_i were calculated using **Equation 4.5** (modified from (Henry and Donahue, 2011; Lane et al., 2008; Presto and Donahue, 2006)) when considering the contribution of all three pathways, where $\alpha_{NO,i}$ is the mass coefficient of compound *i* from RO_2+NO pathway and $\alpha_{HO_2 \text{ and } RO_2,i}$ is the mass coefficient of compound *i* from the combination of

RO_2+RO_2 and RO_2+HO_2 pathways, which is dependent on HO_2/RO_2 ratio. The theoretic SOA yields at intermediate β were obtained using the mass coefficients and effective saturation pressure of the four products.

$$C_{OA} = \sum_i^4 C_i * \left(1 + \frac{C_i^*}{C_{OA}}\right)^{-1} \quad \textbf{Equation 4.2}$$

$$\Delta HC_{HO_2 \text{ and } RO_2} = \Delta HC * (1 - \beta) \quad \textbf{Equation 4.3}$$

$$\Delta HC_{NO} = \Delta HC * \beta \quad \textbf{Equation 4.4}$$

$$\alpha_i(\beta, HO_2/RO_2) = \beta * \alpha_{NO,i} + (1 - \beta) * \alpha_{HO_2 \text{ and } RO_2,i}(HO_2/RO_2) \quad \textbf{Equation 4.5}$$

A global 3-d model of atmospheric chemistry driven by the assimilated meteorological data from the Goddard Earth Observing System (GEOS-Chem) was used in this chapter to estimate the daily profile and average of global surface β.

4.3 Results and discussion

4.3.1 Traditional chamber experiments

The average branching ratio of 105 traditional chamber experiments with varied initial *m*-xylene (11 to 291 ppb) and NO_x (0 to 282 ppb) was calculated with the average concentration of HO_2 and RO_2 using **Equation 4.1** where $k_{RO_2+HO_2}$ and k_{RO_2+NO} are 1.5 * 10^{-11} cm^3/(molecule * s) and 8.5 * 10^{-12} cm^3/(molecule * s). The average branching ratio for each chamber experiment varies from 0 to 1 depending on the initial VOC and NO_x conditions. **Figure 4.1** and **4.2** show the final SOA mass and total *m*-xylene consumption, and final SOA yield and SOA mass from each experiment, grouped by the average branching ratio. While the data points are scattered, the runs with lower branching ratio are

above the runs with higher branching ratio in both figures, suggesting the negative impacts of branching ratio on SOA formation from *m*-xylene. This agrees with the previous studies on NO_x impact on aromatic SOA formation (Li et al., 2015; Ng et al., 2007; Song et al., 2007). For the runs with similar final SOA mass loadings or total *m*-xylene consumption (**Figure 4.3**), SOA yield decreases with β, further suggesting the negative impact of β. However, the scattered data points show large uncertainties when using average branching ratio for a chamber experiment since the branching ratio may not hold constant in those experiments.

Figure 4.4 shows the branching ratio profiles of typical high- and low-NO_x chamber experiments. For the chamber runs with initial NO injections, β started at 1 because the injected NO is significant compared to HO_2 at the beginning of the experiment. After the photo-oxidation started, β dropped drastically as NO decreased to sub-ppb level (**Figure 4.5**) from the NO_x photolysis cycle. A delay effect was observed that the β drops slower compared with NO. This is resulted from the fact that while NO drops drastically, it is still significant and competitive against HO_2 at the beginning of the experiment. When β dropped to a certain level, it leveled off and stayed at a relative constant value for the rest of the experiment.

Traditional high-NO_x methods, with high initial NO_x or initial NO_x/HC, have been widely used to simulate RO_2+NO pathway in chambers. The SOA parameters derived from those chamber experiments are used in current global transport models to represent the SOA yield for the RO_2+NO pathway. However, the β profiles of those experiments shows that those experiments do not represent RO_2+NO pathway alone and the contribution of

RO_2+HO_2 pathway may be significant, especially for the later part of the experiments when β levelled off at a constant low value (**Figure 4.4**). Thus, using SOA parameters from those experiments may lead to bias in SOA prediction. Traditional low-NO_x experiments have their β values constantly maintained at close to 0. As discussed in Chapter 3, β is slightly above 0 because it is impossible to achieve the absolute NO_x-free condition in chamber due to the wall off-gassing. Noting that while β is close to 0, SOA formed may not represent RO_2+HO_2 pathway alone and RO_2+RO_2 pathway can also contribute depending on the HO_2/RO_2 ratio.

4.3.2 Controlled-β chamber experiments

As β changes drastically for a traditional NO_x chamber experiment, the contribution of each pathway may be very different at different times during the experiment. For the run with 12.5 ppb initial NO_x (**Figure 4.4**), for example, RO_2+NO pathway accounts for 55% at 15 minutes after the blacklights were turned on, and this fraction was lowered to 15% at 100 minutes. This suggests that it is necessary to keep β constant so the contribution of RO_2+NO pathway is known and constant throughout the experiment. By controlling β at one, one can simulate and obtain the SOA parameters from RO_2+NO pathway.

The fact that the initial NO is often consumed to sub-ppb level right after the blacklights were turned on suggests that continuously injecting NO throughout the experiment keep β from dropping that fast in chamber. NO was injected continuously in our chamber and the rate was changed step-wisely in order to maintain β in a relatively constant value. **Figure 4.6** and **4.7** show that the β was maintained at a relatively constant

level (0.9 to 1) compared with a traditional high-NO_x experiment. The gas-species such as NO, O_3 and *m*-xylene were measured and estimated using SAPRC11. A descent agreement between measurement and simulation suggests the confidence of gas-phase chemistry simulated by SAPRC11.

4.3.3 RO_2+NO pathway (β = 1)

In order to understand the difference between SOA formation in traditional high-NO_x experiments and β = 1 experiments, as shown in **Figure 4.8**, the two types of experiments were conducted with similar initial *m*-xylene concentration (100 ppb). The initial HC/NO_x ratio was 12 for the traditional high-NO_x experiment and the NO injection rate was adjusted in the range of 20 to 200 ppb/hr throughout the controlled-β high-NO_x experiment to maintain β at 1. For the traditional high-NO_x experiment, β dropped from 1 to 0.4 in the first 100 minutes of photo-oxidation and levelled off at 0.4 for the rest of the experiment, while β was controlled at 1 in the controlled-β high-NO_x experiment. Starting from the similar initial *m*-xylene concentration, the controlled-β high-NO_x experiment shows that *m*-xylene was consumed faster compared to the traditional high-NO_x experiment, indicating a higher OH level when NO was injected continuously. This agrees with previous findings that OH level could be enhanced when low levels (sub-ppb) of NO were artificially maintained (Li et al., 2015). In Figure **4.8**, for the first 45 minutes when β was similar, the enhanced OH increased the *m*-xylene consumption and SOA formation in controlled-β high-β experiment; however, when β started to drop and more RO_2 started reacting with HO_2 for the traditional experiment, SOA yield started increasing and levelled off at more than twice as much as that from controlled-β high β

experiment. This observation agrees with the fact that RO_2+HO_2 pathway has a higher SOA formation potential compared to the RO_2+NO pathway. More importantly, it suggests that the traditional high-NO_x experiments do not accurately represent SOA formation from RO_2+NO pathway. One needs to force β at 1 for chamber experiments in order to obtain the SOA parameters for RO_2+NO pathway.

A set of controlled-β high-NO_x experiments where β were continuously maintained at ~1 was conducted, and the SOA yields are shown in **Figure 4.9**. Noting that it is difficult to reach absolute β = 1 condition since HO_2 cannot be eliminated in chamber, all of the high-NO_x (β = 1) experiments are defined as β being maintained at >0.97. The RO_2+RO_2 pathway only accounts for <1% for all β = 1 experiments. **Figure 4.9** shows two SOA yield curves where higher SOA yield was observed for the runs with smaller NO/RO_2 ratio (< 200). This suggests that other factors such as NO/RO_2 may impact the SOA formation, when almost all of the RO_2 reacts through the RO_2+NO pathway (other pathways such as RO_2+HO_2, RO_2+RO_2 or RO_2+NO_3 were insignificant). In order to understand the impact of NO/RO_2 on SOA formation, one should note that RO_2 is a general term for all of the organic peroxyl radicals here. It includes highly oxygenated RO_2 radicals formed through the intramolecular hydrogen migration and O_2 addition processes on primary RO_2 radicals, as known as RO_2 auto-oxidation. While highly oxygenated RO_2 cannot be clearly speciated in this study, it has been suggested in recent studies that those RO_2 radicals play an important role in SOA formation due to its high oxygen content (Molteni et al., 2018; Praske et al., 2018; Pye et al., 2019; Wang et al., 2020, 2017). As an important sink for RO_2 at β = 1 scenario, the presence of NO

terminates the RO_2 auto-oxidation to form highly oxygenated RO_2. It is proposed here that the observation of lower SOA yield at higher NO/RO_2 ratio may be caused by less highly oxygenated RO_2 formed due to the higher NO. It was observed that the runs with higher NO/RO_2 ratio and similar initial *m*-xylene tend to have lower RO_2 ratio in general, suggesting that more RO_2 was terminated with in RO_2+NO pathway. The lifetime of RO_2 in those runs tend to be shorter.

To investigate the NO effect on RO_2 auto-oxidation, the biomolecular (with NO and other radicals) lifetime of RO_2 ($\tau_{\mathrm{bimolecular}}$) were calculated for the two NO/RO_2 scenarios using **Equation 4.6** (Praske et al., 2018), as comparison with unimolecular (auto-oxidation) lifetime ($\tau_{\mathrm{unimolecular}}$). The runs with NO/RO_2 ratio > 200 show larger $\tau_{\mathrm{bimolecular}}$ (1 to 3s) compared to the runs with lower NO/RO_2 ratio (<1s). While the $\tau_{\mathrm{unimolecular}}$ data is limited, a theoretical study reported $\tau_{\mathrm{unimolecular}}$ for aromatic RO_2 of 7s to 14s (Wang et al., 2017). This further suggests that the $\tau_{\mathrm{bimolecular}}$ under both NO/RO_2 scenarios would affect the extent of RO_2 auto-oxidation. Recent studies have also showed the negative NO effects on RO_2 auto-oxidation from biogenic SOA precursors in chamber studies and field measurements (Praske et al., 2018; Pye et al., 2019; Schervish and Donahue, 2020; Wang et al., 2020; Yan et al., 2020), further investigation on aromatic system in the aspect of aerosol composition is suggested.

$$\tau_{\mathrm{bimolecular}} = \frac{1}{k_{RO_2+HO_2}[HO_2]+k_{RO_2+RO_2}[RO_2]+k_{RO_2+NO}[NO]} \qquad \textbf{Equation 4.6}$$

In order to understand which one of the SOA yields curves (β = 1) can better represent the SOA formation in the atmosphere, the bimolecular RO_2 lifetime was used as

an indicator of RO_2 auto-oxidation in chamber. The bimolecular RO_2 lifetime ($\tau_{bimolecular}$) of the lower-NO/RO_2 runs falls into atmosphere range (1 to 100s) (Praske et al., 2018) thus it better represents the auto-oxidation condition and SOA formation in the atmosphere compared to the higher-NO/RO_2 runs. Noting that even though the lower-NO/RO_2 only covers the lower bound of RO_2 lifetime in atmosphere and the current chamber study may not represent regions with higher RO_2 lifetime and more RO_2 auto-oxidation, the results still suggest that auto-oxidation is a source of underprediction of SOA in current models. Further investigation on SOA at even lower NO/RO_2 is needed to simulate the SOA formation and RO_2 auto-oxidation on the regions with higher RO_2 lifetime.

4.3.4 Intermediate β

The global surface β in a typical summer month (July) was modelled and categorized based on its value and daily profile into four categories (**Figure 4.10** and **Figure 4.11**). Categories "long" (daytime β: 0.6 to 0.8) and "short" (daytime β: 0.4 to 0.6) represent more and less populated continents, respectively. Categories "high" (daytime β: 0.5) and "low" (daytime β: 0.2) represent the Arctic, the Antarctic and the ocean regions with less impacts from human-activities. Noting that the category "high" shows a constant β at 0.5 throughout the whole day and the category "low" shows that β only maintains at 0.2 for a short period of the day. This is because the longer daytime is expected in the Northern hemisphere (midnight sun in the Arctic) and the sunlight maintains NO and β at a certain level due to the NO_2 photolysis. **Figure 4.11** shows that the β value for all categories is relatively constant during the daytime when the sunlight

was available compared with the traditional chamber experiments, further suggesting the important of controlling β in chamber experiments.

Figure 4.12 shows the comparison between a traditional NO_x experiment and an intermediate controlled-β (β = 0.4) experiment. During the first 100 minutes when β dropped from 1 to 0.4 for the traditional experiment, β in the controlled-β experiment was maintained at 0.4. While less *m*-xylene was consumed for the controlled-β experiment during this period, the SOA formation was more because β was smaller (0.4) and more fraction of RO_2 was expected to be consumed in RO_2+ HO_2 pathway compared with RO_2+NO pathway. After the first 100 minutes, β was almost constant at 0.4 for both experiments, the larger amount of *m*-xylene available leads the higher final SOA formation. The final SOA yield was larger from the traditional chamber experiment. Controlling β during chamber experiment constrains the contribution from each pathway at a fixed fraction throughout the experiment and provides a useful measure to characterize the SOA yield parameters from each pathway.

SOA formation from *m*-xylene was investigated when controlling β constantly at four different levels (0, 0.4, 0.8 and 1) (**Figure 4.13**). It was shown that for the runs with higher β values in chamber, *m*-xylene decreased in a faster rate, suggesting the higher OH available for higher β runs. However, the lower SOA formation was observed for those runs due to the higher fraction of RO_2+NO pathway. While it is generally believed that the value of β negatively impacts the SOA formation from aromatic compounds as the products from RO_2+NO pathway are more volatile than those from RO_2+HO_2 pathway, no experimental data was available on intermediate β. **Figure 4.13** presents the SOA

formation at different β conditions including intermediate β and further confirms the negative β impact on SOA. In order to understand the β impacts on SOA yield, **Figure 4.14** shows three controlled-β experiments (β = 0, 0.4 and 1) with similar SOA mass loading (~25 ug/m^3). It is shown that when ruling out the organic material absorbing effects by comparing the runs with similar mass loading, the SOA yield decreased with β (**Figure 4.15**).

The SOA yields of controlled-β experiments with β ranging from 0 to 1 are shown in **Figure 4.16**. Since most experiments with β > 0 showed the HO_2/RO_2 > 1.5, only those runs are presented in **Figure 4.17** to reduce the complexity of the figure. The SOA yield curves for β = 0 (HO_2/RO_2 > 1.5) and β = 1 (NO/RO_2 < 200) were fitted with measured data. A linear combination approach of VBS parameters based on β has been used to estimate the SOA at intermediate betas (Lane et al., 2008; Pye et al., 2010). In order to verify if the linear combination approach represents the actual SOA formation condition, the theoretical SOA yield parameters were calculated using **Equation 4.5** with the three sets of SOA yield parameters at β = 0 and one set of parameters at β = 1. **Figure 4.17** shows a disagreement between the measured SOA yield and theoretical prediction for the intermediate β runs and the measured SOA yields were lower. This suggests that the linear combination approach may not represent the complicated chemistry for the SOA formation from aromatic oxidation and the SOA yield parameters for intermediate β need to be obtained experimentally.

4.4 Conclusion

This study evaluated the current approach of estimating SOA formation from aromatics with different levels of NO_x. The branching ratio of RO_2+NO pathway (β) profile of traditional high NO_x experiments suggests that those experiments do not fully represent RO_2+NO pathway and the contribution of RO_2+HO_2 pathway maybe significant. A novel approach of controlling the branching ratio of RO_2+NO pathway (β) in chamber experiments was developed to obtain the SOA yield parameters for this pathway. When almost all RO_2 was forced to react in RO_2+NO pathway (β = 1), multiple SOA yield curves were observed and more NO led to lower SOA yield. The analysis of RO_2 lifetime under β = 1 condition suggests the presence of NO may suppress the extent of RO_2 auto-oxidation and lead to lower SOA formation. While similar NO impacts on RO_2 auto-oxidation was reported in other chamber and field studies on biogenic SOA precursors (Praske et al., 2018; Pye et al., 2019; Schervish and Donahue, 2020; Wang et al., 2020; Yan et al., 2020), further investigation on aromatic system is suggested. The controlling-β approach is also used for intermediate β conditions. It was shown that the current linear combination approach using yield parameters at β = 0 and β = 1 with β do not accurately estimate SOA yield for intermediate β and those parameters need to be obtained experimentally.

Tables & Figures

Table 4.1: Summary of controlled-β experiments

Run	Time	β	H_2O_2	Consumed VOC	SOA Mass	Yield	OH	RO_2	HO_2	NO	NO_3
	min		ppm	ug/m^3	ug/m^3		molecules/cm^3				
474B	710	0.0	4.0	310.50	130.20	42%	1.43E+06	1.84E+09	5.36E+09	1.66E+07	6.44E+02
474A	710	0.0	4.0	302.22	114.80	38%	1.43E+06	1.84E+09	5.37E+09	1.67E+07	7.14E+02
1180B	296	0.0	4.0	621.00	194.60	31%	2.84E+06	6.57E+09	6.22E+09	2.06E+07	8.30E+02
473A	732	0.0	2.0	281.52	85.40	30%	1.08E+06	2.71E+09	2.82E+09	1.77E+07	7.98E+02
473B	732	0.0	2.0	298.96	91.18	30%	1.08E+06	2.71E+09	2.82E+09	1.76E+07	7.87E+02
1209A	371	0.0	2.0	656.00	126.00	19%	1.86E+06	9.30E+09	2.88E+09	1.86E+07	1.96E+03
1209B	371	0.0	2.0	509.00	95.00	19%	2.15E+06	7.42E+09	3.32E+09	2.32E+07	1.48E+03
1212A	348	0.0	2.0	385.10	126.00	33%	2.83E+06	4.45E+09	4.44E+09	3.71E+07	2.56E+03
1212B	348	0.0	2.0	188.91	65.80	35%	3.91E+06	1.89E+09	6.16E+09	7.99E+07	6.73E+03
472A	695	0.0	1.0	255.38	44.42	17%	6.83E+05	4.39E+09	1.20E+09	1.62E+07	1.04E+03
472B	695	0.0	1.0	241.77	48.58	20%	7.17E+05	4.06E+09	1.26E+09	1.75E+07	1.46E+03
1248B	281	0.0	1.0	305.25	67.87	22%	1.83E+06	6.63E+09	1.99E+09	3.43E+07	2.43E+03
476B	721	0.0	1.0	153.42	38.65	25%	1.04E+06	1.98E+09	1.95E+09	3.44E+07	2.25E+03
1424B	365	0.0	1.0	300.37	56.47	19%	1.98E+06	5.66E+09	2.24E+09	4.01E+07	4.45E+03
476A	721	0.0	1.0	140.96	36.04	26%	1.06E+06	1.94E+09	1.97E+09	3.51E+07	2.11E+03
2563A	422	0.0	1.0	301.79	58.09	19%	2.24E+06	4.65E+09	2.56E+09	5.19E+07	5.23E+03
2563B	422	0.0	1.0	277.00	49.67	18%	2.33E+06	4.37E+09	2.65E+09	5.54E+07	5.82E+03
2567A	431	0.0	1.0	231.92	45.70	20%	2.50E+06	3.86E+09	2.84E+09	6.32E+07	9.87E+03
2567B	431	0.0	1.0	234.62	41.92	18%	2.51E+06	3.85E+09	2.84E+09	6.34E+07	6.42E+03
750A	889	0.0	1.0	228.14	43.98	19%	7.95E+05	2.20E+09	1.58E+09	4.00E+07	2.97E+03
478B	634	0.0	1.0	75.42	21.26	28%	1.42E+06	9.37E+08	2.65E+09	6.72E+07	4.95E+03
2569A	392	0.0	1.0	157.69	24.13	15%	3.15E+06	2.48E+09	3.52E+09	9.67E+07	9.71E+03

Table 4.1: Experiment summary (continue)

Run	Time	β	H_2O_2	Consumed VOC	SOA Mass	Yield	OH	RO_2	HO_2	NO	NO_3
	min		ppm	ug/m^3	ug/m^3		molecules/cm^3				
1860B	570	0.0	1.0	434.44	100.52	23%	1.94E+06	5.08E+09	2.44E+09	8.29E+07	9.16E+03
2568B	374	0.0	1.0	115.88	24.94	22%	3.55E+06	1.88E+09	3.92E+09	1.24E+08	1.47E+04
1860A	570	0.0	1.0	208.37	51.94	25%	2.90E+06	2.82E+09	3.25E+09	1.49E+08	2.80E+04
2569B	392	0.0	1.0	73.24	14.92	20%	4.34E+06	1.05E+09	4.61E+09	2.10E+08	4.57E+04
471A	710	0.0	0.4	168.39	17.28	10%	3.91E+05	3.99E+09	6.40E+08	3.34E+07	3.73E+03
471B	764	0.0	0.4	176.13	23.93	14%	4.02E+05	3.92E+09	6.46E+08	3.37E+07	2.82E+03
2570B	348	0.0	1.0	45.42	7.92	17%	4.98E+06	5.88E+08	5.11E+09	3.01E+08	1.11E+05
2574B	349	0.2	1.0	465.30	52.66	11%	2.28E+06	3.59E+09	3.45E+09	1.78E+09	3.54E+05
2582B	369	0.2	1.0	471.95	56.09	12%	2.25E+06	3.64E+09	3.41E+09	1.86E+09	3.85E+05
2600B	400	0.2	2.0	592.01	85.12	14%	3.95E+06	3.27E+09	5.46E+09	2.99E+09	6.06E+06
2581B	351	0.3	1.0	66.61	8.67	13%	8.06E+06	6.65E+08	4.80E+09	3.29E+09	1.68E+07
2580B	292	0.3	1.0	95.22	13.54	14%	6.63E+06	9.87E+08	4.63E+09	2.74E+09	6.75E+06
2571A	309	0.3	1.0	97.29	11.22	12%	7.27E+06	9.43E+08	4.62E+09	3.34E+09	1.25E+07
2570A	348	0.4	1.0	162.75	23.58	14%	6.77E+06	1.32E+09	4.31E+09	4.01E+09	2.02E+07
2572A	303	0.4	1.0	365.78	39.89	11%	4.02E+06	2.48E+09	3.92E+09	4.07E+09	3.96E+06
2599B	370	0.7	0.0	910.79	64.68	7%	2.56E+06	2.15E+09	2.76E+09	1.08E+10	5.83E+07
2575B	358	0.7	0.0	201.51	12.67	6%	3.32E+06	1.13E+09	1.46E+09	6.22E+09	5.72E+06
2576B	340	0.8	0.0	402.88	29.07	7%	5.05E+06	1.22E+09	1.75E+09	1.42E+10	5.67E+07
2573B	371	0.9	0.0	393.61	27.38	7%	5.79E+06	6.26E+08	9.38E+08	4.83E+10	8.99E+07
2546A	486	1.0	0.0	361.42	33.00	9%	5.03E+06	5.21E+08	7.84E+08	8.99E+10	8.70E+07
2564A	392	1.0	0.0	356.12	21.62	6%	5.43E+06	5.33E+08	7.93E+08	7.19E+10	7.16E+07
2565A	362	1.0	0.0	357.19	20.02	6%	5.60E+06	5.31E+08	7.86E+08	7.06E+10	6.59E+07

Table 4.1: Experiment summary (continue)

Run	Time	β	H_2O_2	Consumed VOC	SOA Mass	Yield	OH	RO_2	HO_2	NO	NO_3
	min		ppm	ug/m^3	ug/m^3		molecules/cm^3				
2596B	348	1.0	1.0	1014.29	33.08	3%	6.33E+06	4.60E+08	9.48E+08	1.68E+11	4.36E+08
2566A	337	1.0	0.0	372.89	18.15	5%	5.67E+06	4.42E+08	6.54E+08	8.18E+10	6.67E+07
2591B	377	1.0	1.0	687.23	22.98	3%	7.18E+06	4.75E+08	1.05E+09	1.16E+11	3.21E+08
2568A	374	1.0	0.0	160.81	5.81	4%	5.89E+06	2.85E+08	4.17E+08	9.94E+10	2.40E+07
2598B	369	1.0	1.0	1568.83	67.08	4%	5.23E+06	4.06E+08	7.51E+08	3.60E+11	3.02E+08
2590B	310	1.0	1.0	409.86	7.06	2%	8.27E+06	1.87E+08	5.28E+08	1.48E+11	1.64E+08
2597B	378	1.0	0.0	629.18	11.38	2%	4.61E+06	2.01E+08	3.21E+08	2.44E+11	1.10E+08

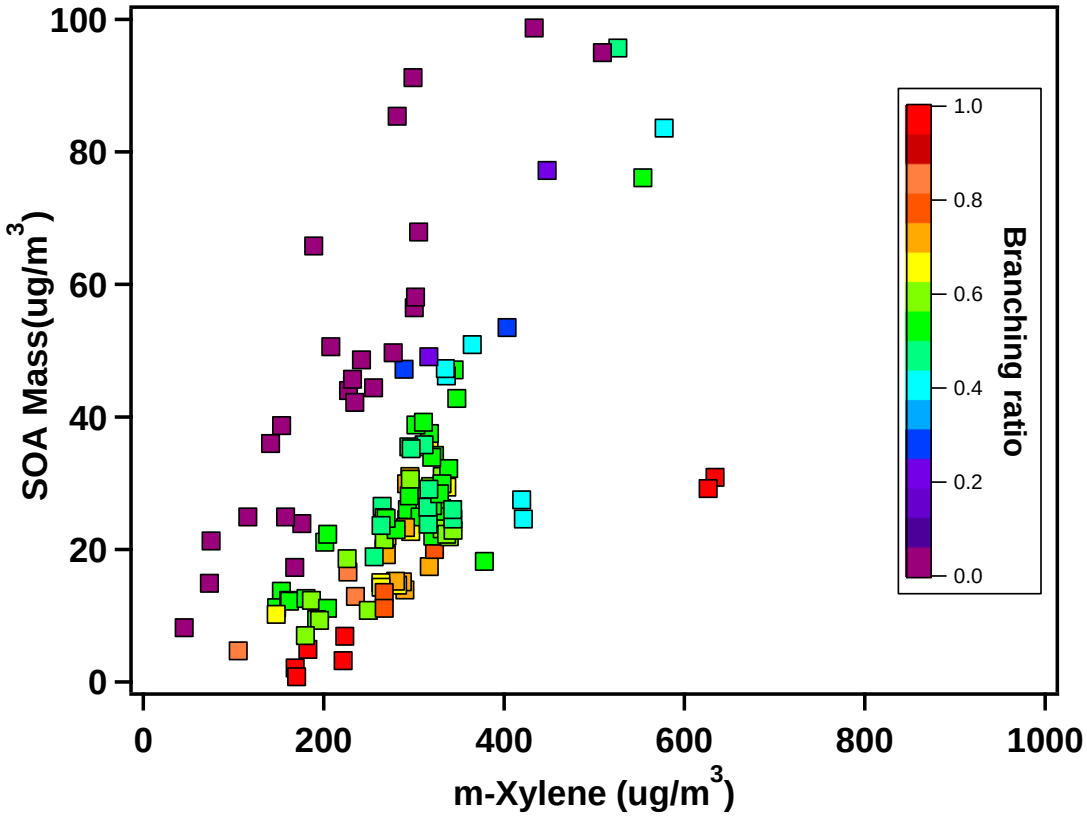

Figure 4.1: Final SOA mass and total *m*-xylene consumption of traditional chamber experiments grouped by the average branching ratio

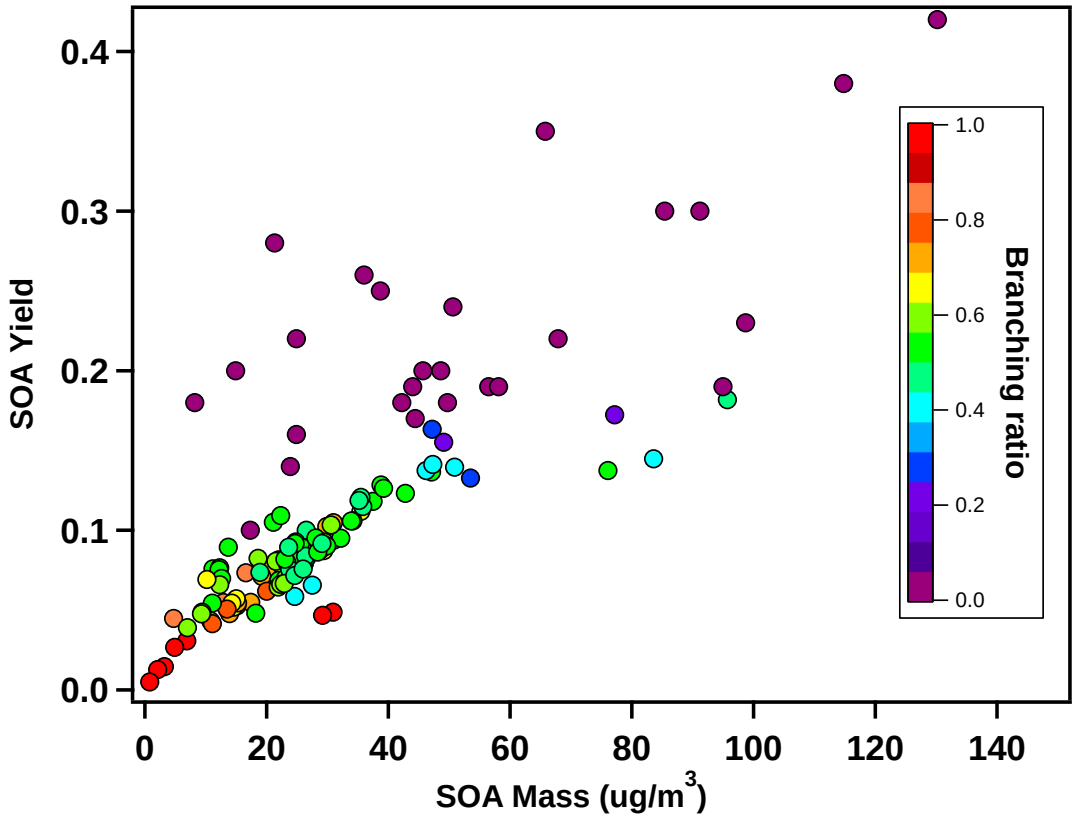

Figure 4.2: Final SOA yield and mass of traditional chamber experiments grouped by the average branching ratio.

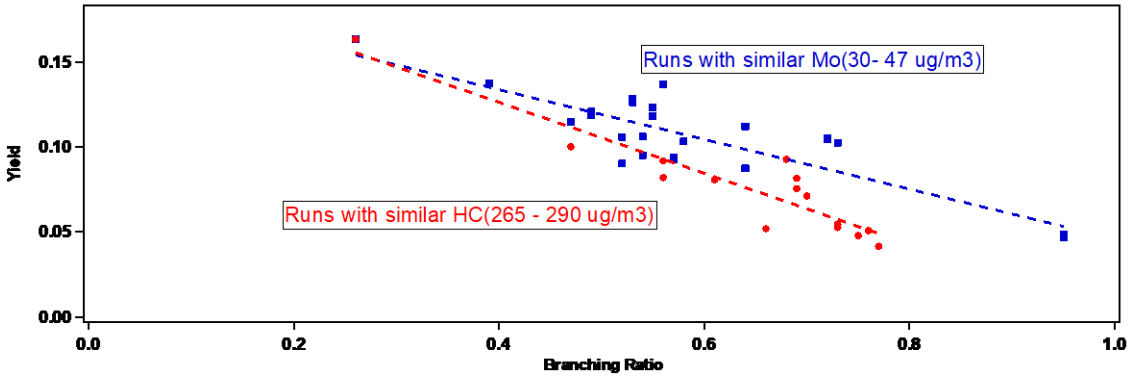

Figure 4.3: Final SOA yield and mass of traditional chamber experiments with (blue) similar final mass (30 to 47 ug/m^3) and (red) similar *m*-xylene consumption (265 to 290 ug/m^3)

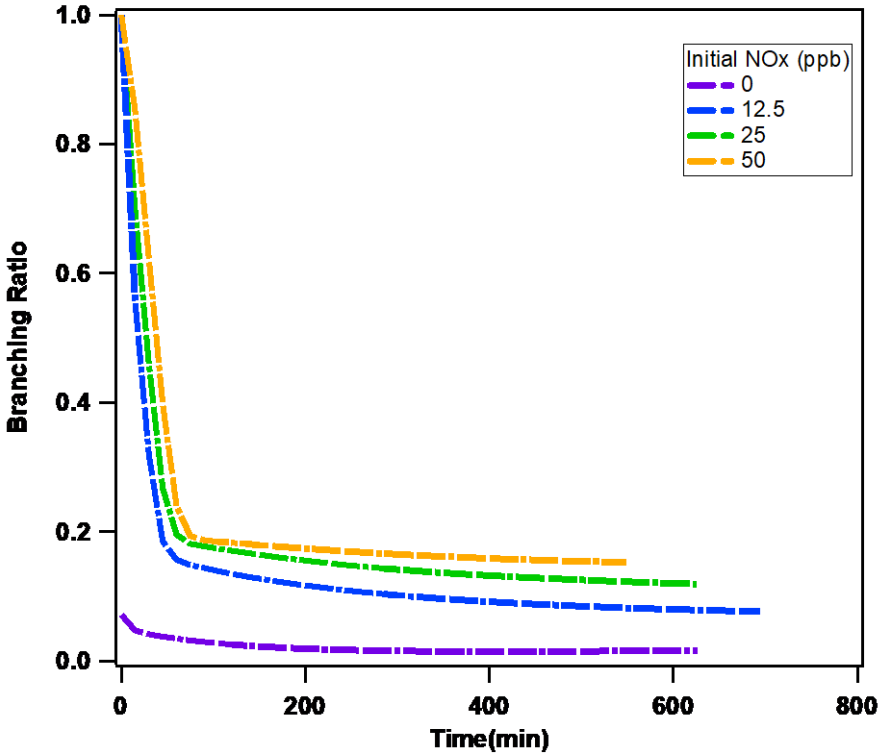

Figure 4.4: The branching ratio of RO_2+NO pathway for four traditional chamber experiments with 80 ppb of initial *m*-xylene, 1 ppm of initial H_2O_2 and 0, 12.5, 25 and 50 ppb of initial NO_x

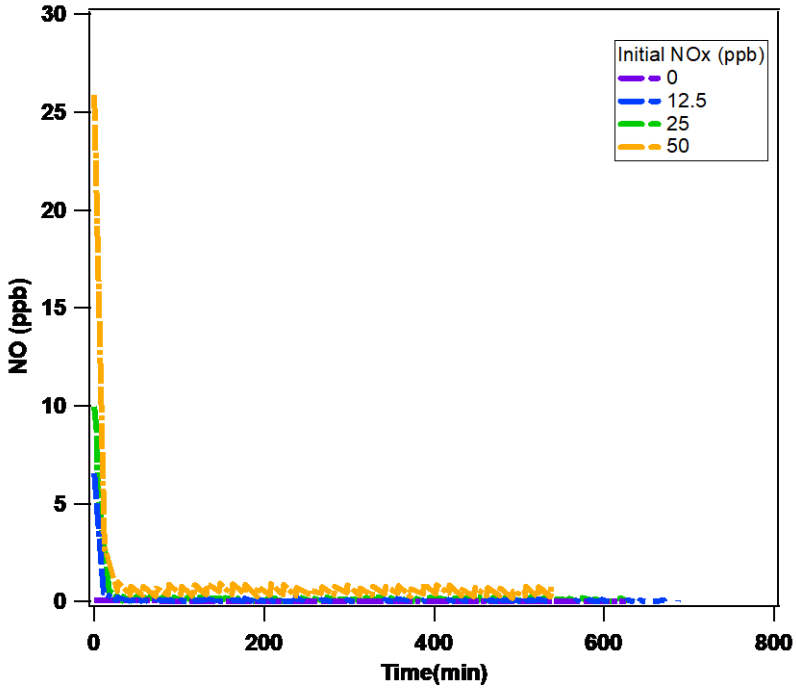

Figure 4.5: The measured NO concentration for four traditional chamber experiments with 80 ppb of initial *m*-xylene, 1 ppm of initial H_2O_2 and 0, 12.5, 25 and 50 ppb of initial NO_x

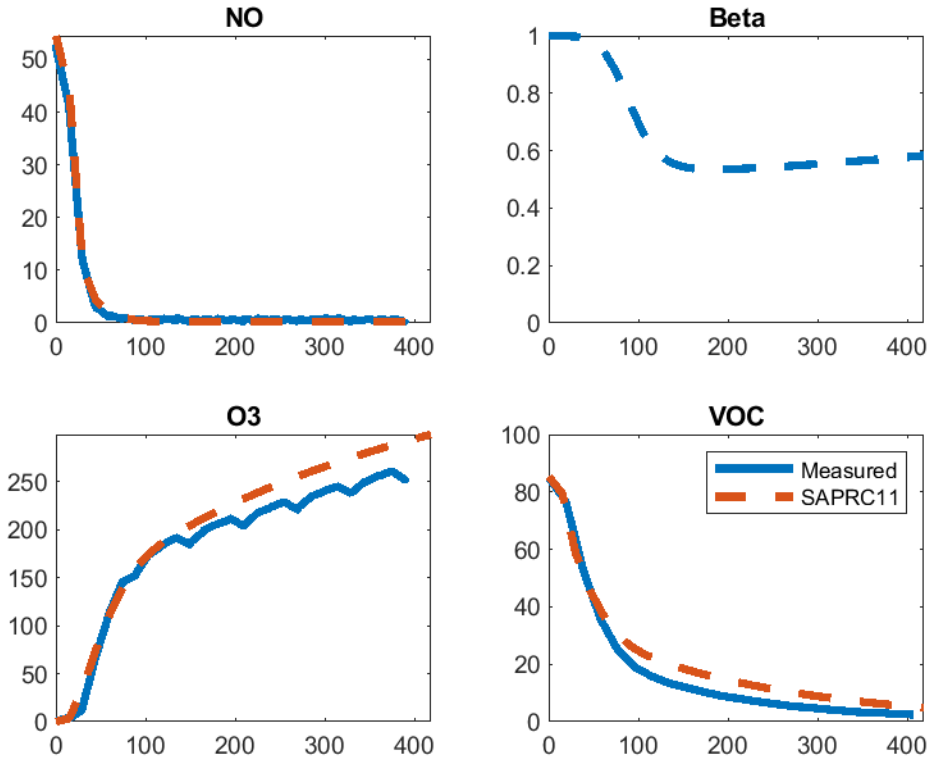

Figure 4.6: Comparison between SAPRC11 simulation and experimental measurements for the profile of NO_x (ppb), the branching ratio (β) of RO_2+NO (considering RO_2+NO and RO_2+HO_2 pathways), O_3 (ppb) and VOC (ppb) versus time (min) from a typical traditional high-NO_x experiment

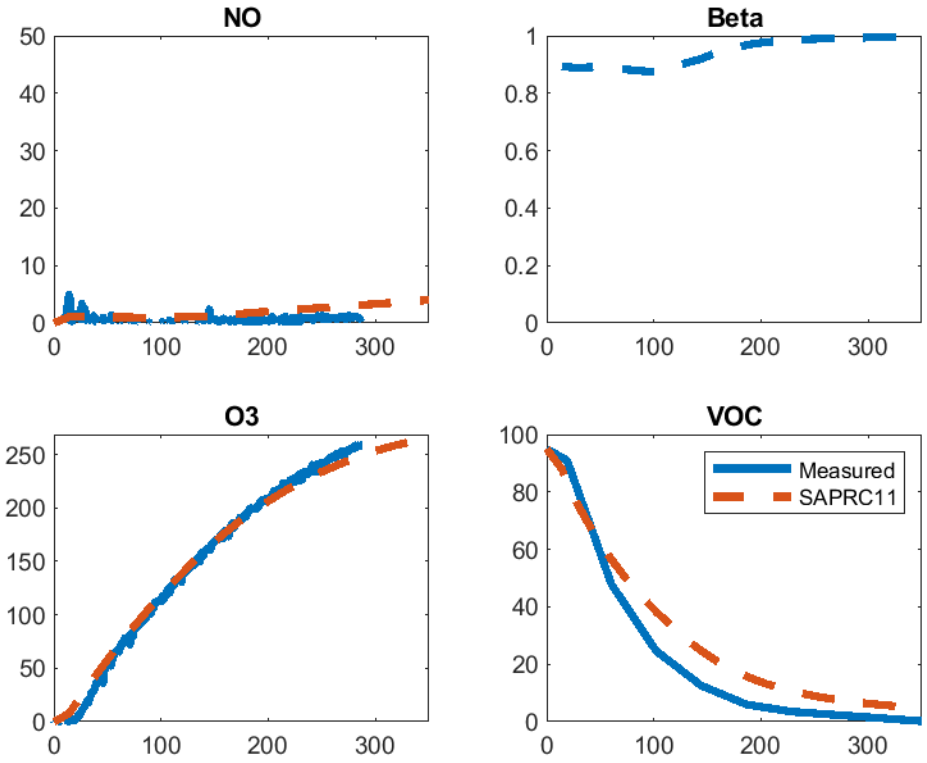

Figure 4.7: Comparison between SAPRC11 simulation and experimental measurements for the profile of NO_x (ppb), the branching ratio (β) of RO_2+NO (considering RO_2+NO and RO_2+HO_2 pathways), O_3 (ppb) and VOC (ppb) versus time (min) from a typical β-controlled (β = 1) experiment

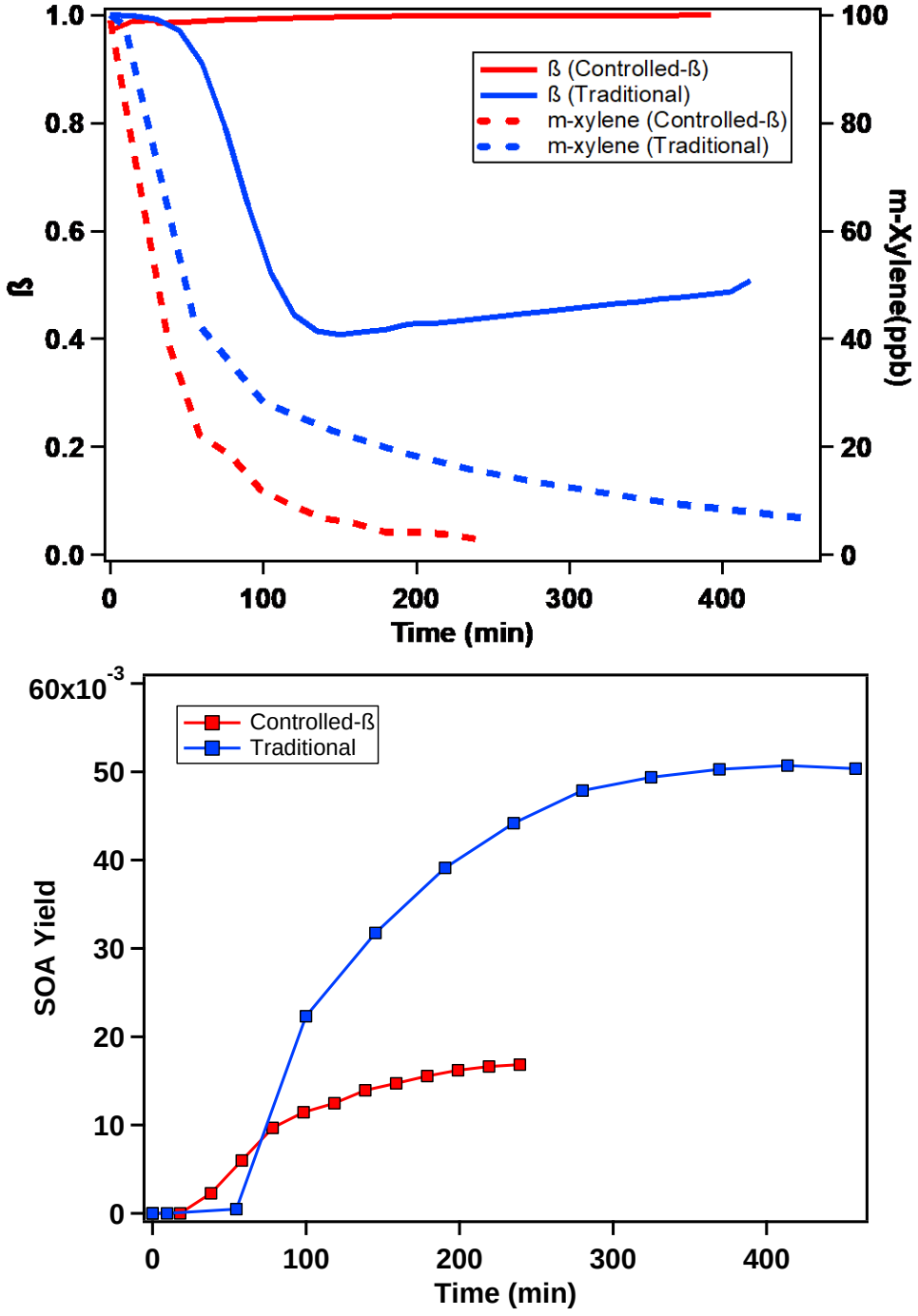

Figure 4.8: β, *m*-xylene (top) and SOA yield (bottom) profiles from a typical traditional high-NO_x experiment and a typical controlled- β high-NO_x experiment (β = 1)

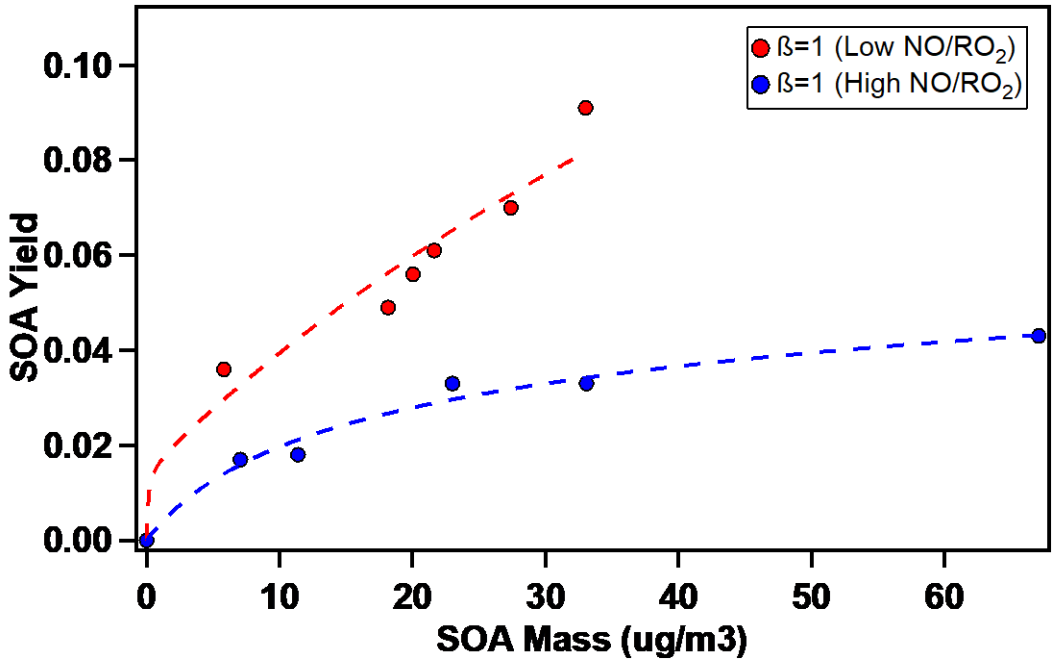

Figure 4.9: SOA yield of controlled-β high-NO_x experiments (β = 1)

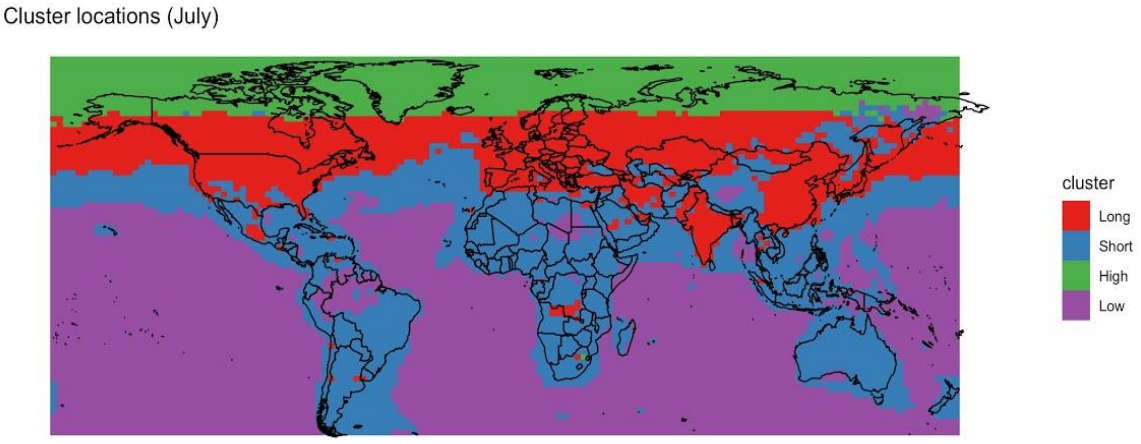

Figure 4.10: Global surface β (four categories) patterns modelled from GEOS-Chem

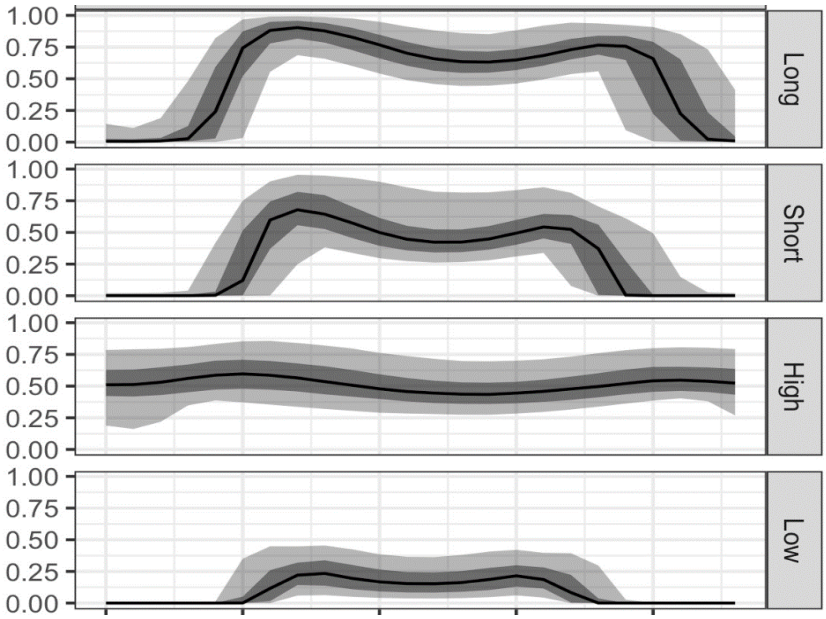

Figure 4.11: The average daily profile of the global surface β (four categories) modelled from GEOS-Chem

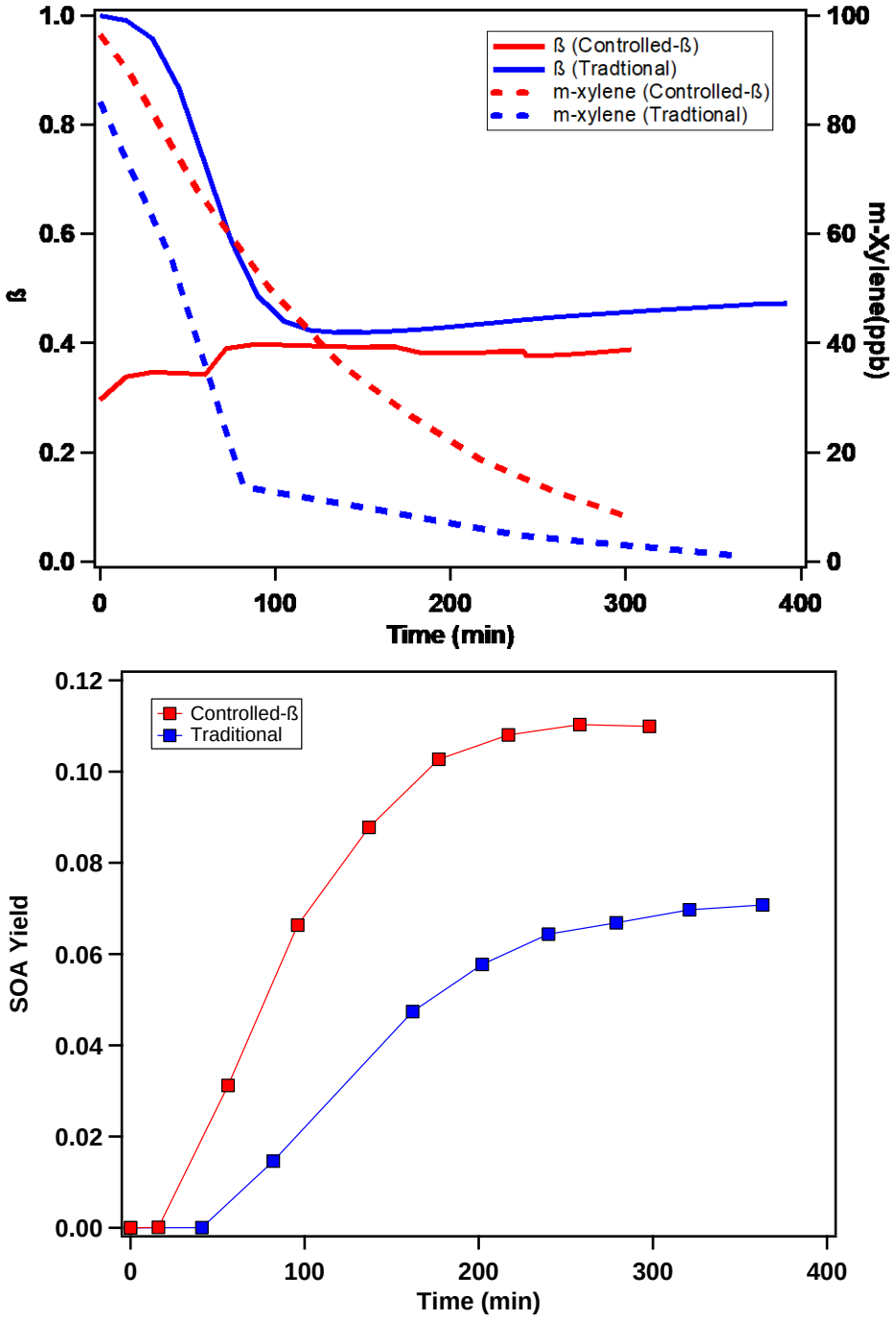

Figure 4.12: β, *m*-xylene (top) and SOA yield (bottom) profiles from a typical traditional high-NO_x experiment and a typical controlled-β high-NO_x experiment (β = 0.4)

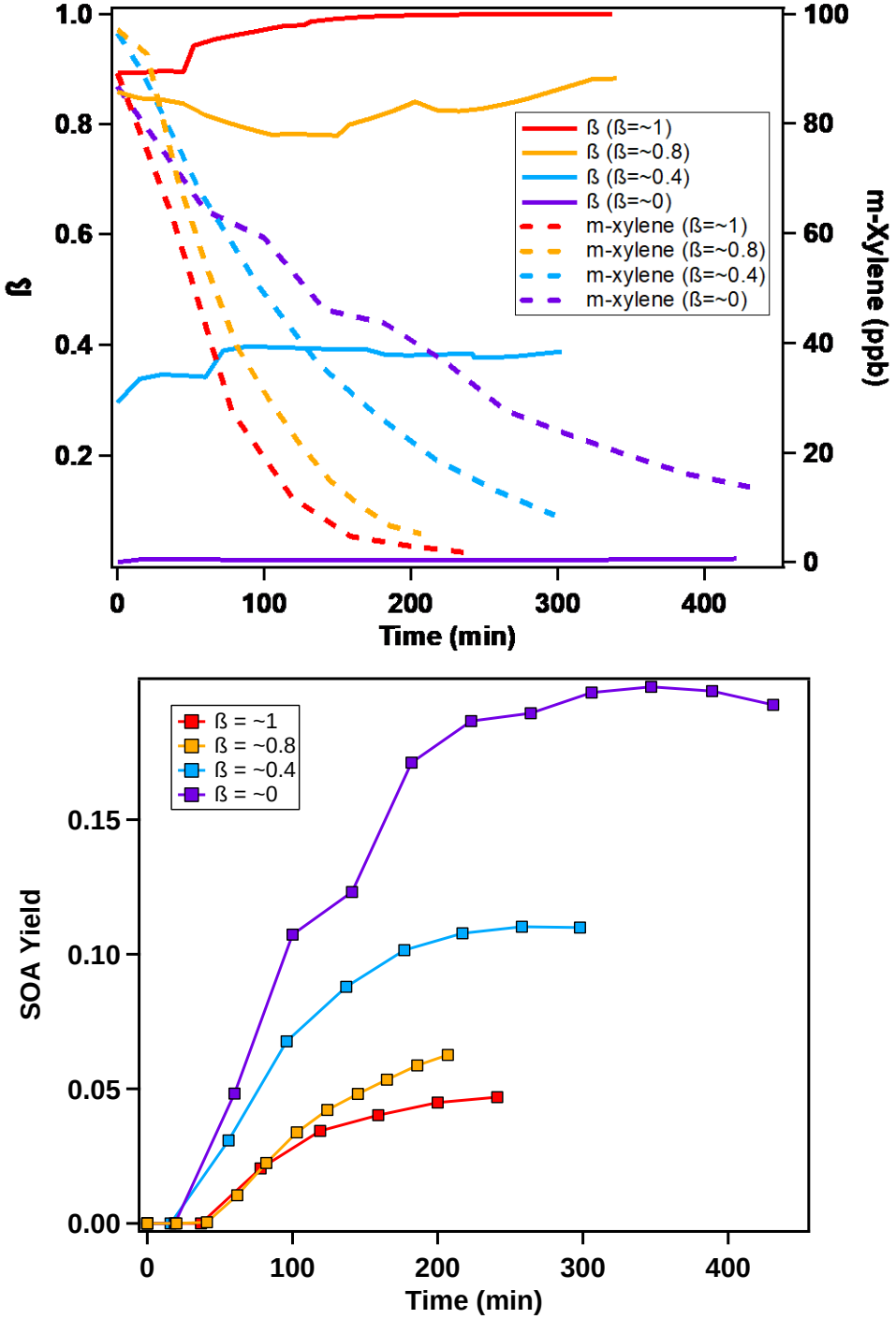

Figure 4.13: β, *m*-xylene (top) and SOA yield (bottom) profiles of four controlled-β experiments (β = 0, 0.4, 0.8 and 1) with similar initial *m*-xylene concentrations (~100 ppb)

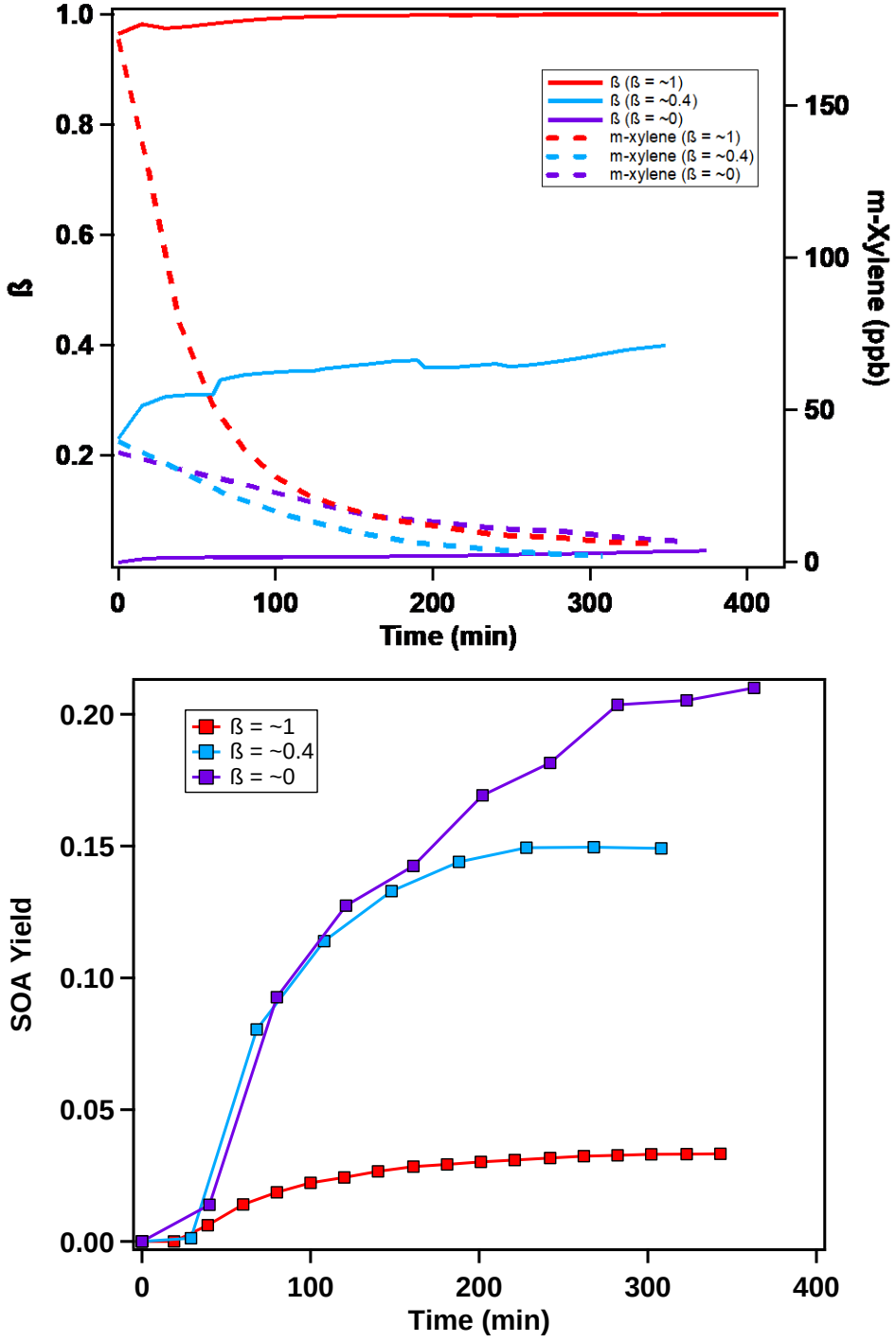

Figure 4.14: β, *m*-xylene (top) and SOA yield (bottom) profiles of three controlled-β experiments (β = 0, 0.4 and 1) with similar final SOA mass loading (~25 ug/m^3)

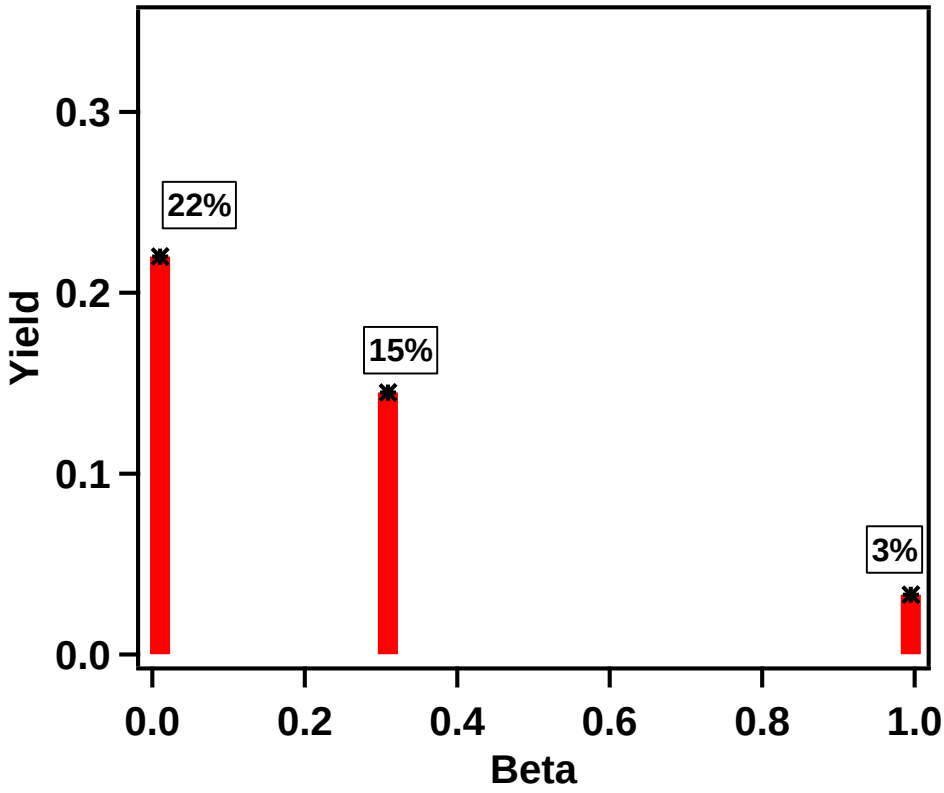

Figure 4.15: SOA yields of three controlled-β experiments (β = 0, 0.4 and 1) with similar SOA mass loading (~25 ug/m^3)

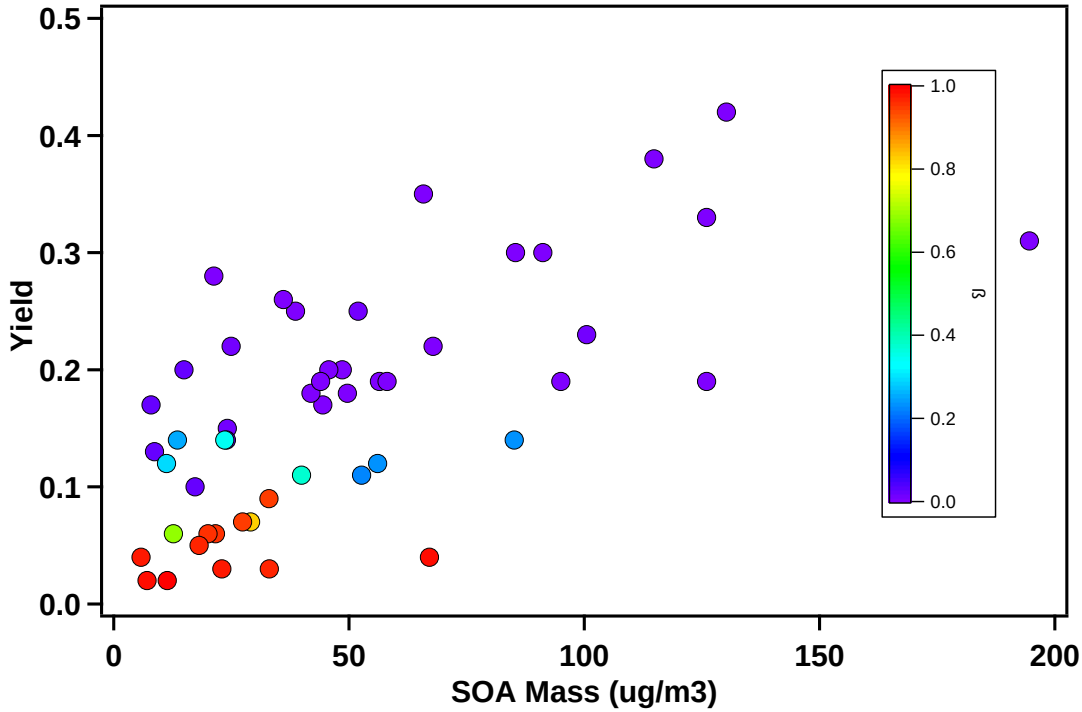

Figure 4.16: Final SOA yields from controlled-β *m*-xylene experiments at different β

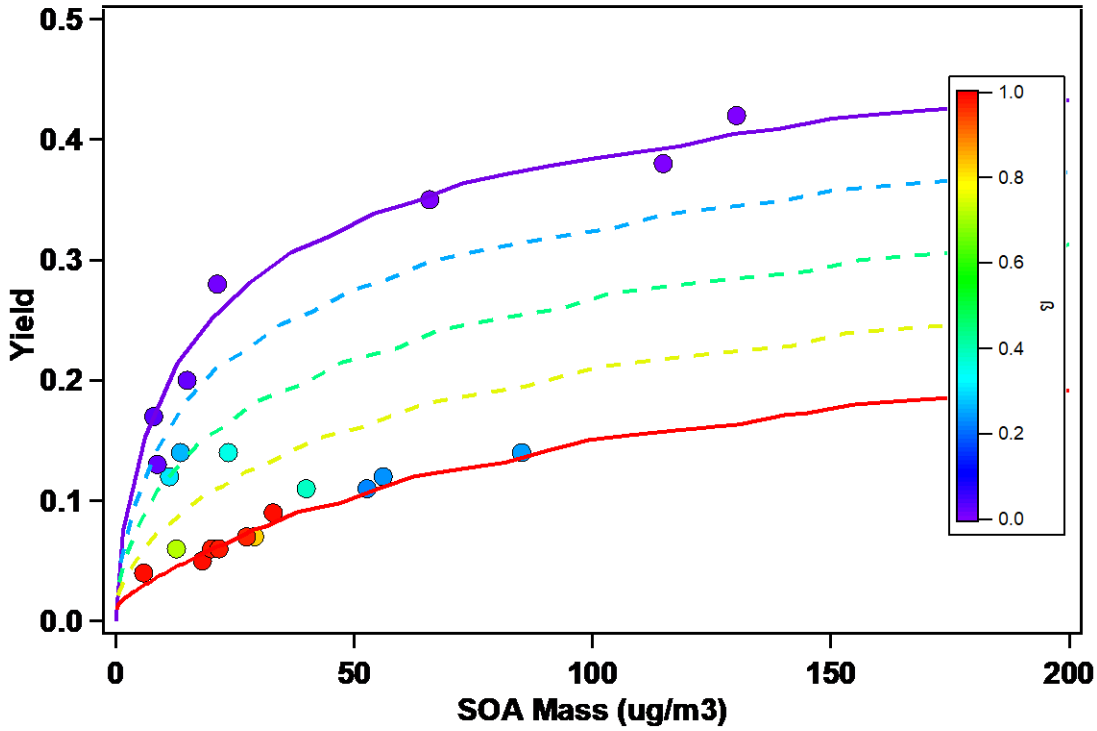

Figure 4.17: Final SOA yields from β-controlled *m*-xylene experiments at different β assuming RO_2+RO_2 accounts for < 3% and the theoretical SOA yield calculated using parameters for RO_2+NO pathway (NO/HO_2 < 200) and RO_2+HO_2 pathway (HO_2/RO_2 > 1.5)

Reference

Cao, G., Jang, M., 2008. Secondary organic aerosol formation from toluene photooxidation under various NO_x conditions and particle acidity. Atmos. Chem. Phys. Discuss. 8, 14467–14495. https://doi.org/10.5194/acpd-8-14467-2008

Carlton, A.G., Bhave, P. V., Napelenok, S.L., Edney, E.O., Sarwar, G., Pinder, R.W., Pouliot, G.A., Houyoux, M., 2010. Model representation of secondary organic aerosol in CMAQv4.7. Environ. Sci. Technol. 44, 8553–8560. https://doi.org/10.1021/es100636q

Carter, W.P.L., Cocker, D.R., Fitz, D.R., Malkina, I.L., Bumiller, K., Sauer, C.G., Pisano, J.T., Bufalino, C., Song, C., 2005. A new environmental chamber for evaluation of gas-phase chemical mechanisms and secondary aerosol formation. Atmos. Environ. https://doi.org/10.1016/j.atmosenv.2005.08.040

Carter, W.P.L., Heo, G., Cocker III, D.R., Nakao, S., Cocker, D.R., Nakao, S., 2012. Soa Formation : Chamber Study and MODEL DEVELOPMENT.

Cocker, D.R., Flagan, R.C., Seinfeld, J.H., 2001. State-of-the-art chamber facility for studying atmospheric aerosol chemistry. Environ. Sci. Technol. 35, 2594–2601. https://doi.org/10.1021/es0019169

Corbin, J.C., Peng, W., Yang, J., Sommer, D.E., Trivanovic, U., Kirchen, P., Miller, J.W., Rogak, S., Cocker, D.R., Smallwood, G.J., Lobo, P., Gagné, S., 2020. Characterization of particulate matter emitted by a marine engine operated with liquefied natural gas and diesel fuels. Atmos. Environ. 220. https://doi.org/10.1016/j.atmosenv.2019.117030

Donahue, N.M., Robinson, A.L., Stanier, C.O., Pandis, S.N., 2006. Coupled partitioning, dilution, and chemical aging of semivolatile organics. Environ. Sci. Technol. 40, 2635–2643. https://doi.org/10.1021/es052297c

Farina, S.C., Adams, P.J., Pandis, S.N., 2010. Modeling global secondary organic aerosol formation and processing with the volatility basis set: Implications for anthropogenic secondary organic aerosol. J. Geophys. Res. Atmos. 115. https://doi.org/10.1029/2009JD013046

Guillaume, B., Liousse, C., Rosset, R., Cachier, H., Van Velthoven, P., Bessagnet, B., Poisson, N., 2007. ORISAM-TM4: A new global sectional multi-component aerosol model including SOA formation - Focus on carbonaceous BC and OC aerosols, in: Tellus, Series B: Chemical and Physical Meteorology. https://doi.org/10.1111/j.1600-0889.2006.00246.x

Henry, K.M., Donahue, N.M., 2011. Effect of the OH radical scavenger hydrogen peroxide on secondary organic aerosol formation from α-pinene ozonolysis. Aerosol Sci. Technol. 45, 696–700. https://doi.org/10.1080/02786826.2011.552926

Henze, D.K., Fu, T.-M., Jacob, D.J., Heald, C.L., Ng, N.L., Seinfeld, J.H., Kroll, J.H., 2010. Global modeling of secondary organic aerosol formation from aromatic hydrocarbons: high- vs low-yield pathways. Atmos. Chem. Phys. Discuss. 7, 14569–14601. https://doi.org/10.5194/acpd-7-14569-2007

Jimenez, J.L., Canagaratna, M.R., Donahue, N.M., Prevot, A.S.H.H., Zhang, Q., Kroll, J.H., DeCarlo, P.F., Allan, J.D., Coe, H., Ng, N.L., Aiken, A.C., Docherty, K.S., Ulbrich, I.M., Grieshop, A.P., Robinson, A.L., Duplissy, J., Smith, J.D., Wilson, K.R., Lanz, V.A., Hueglin, C., Sun, Y.L., Tian, J., Laaksonen, A., Raatikainen, T., Rautiainen, J., Vaattovaara, P., Ehn, M., Kulmala, M., Tomlinson, J.M., Collins, D.R., Cubison, M.J., Dunlea, J., Huffman, J.A., Onasch, T.B., Alfarra, M.R., Williams, P.I., Bower, K., Kondo, Y., Schneider, J., Drewnick, F., Borrmann, S., Weimer, S., Demerjian, K., Salcedo, D., Cottrell, L., Griffin, R., Takami, A., Miyoshi, T., Hatakeyama, S., Shimono, A., Sun, J.Y., Zhang, Y.M., Dzepina, K., Kimmel, J.R., Sueper, D., Jayne, J.T., Herndon, S.C., Trimborn, A.M., Williams, L.R., Wood, E.C., Middlebrook, A.M., Kolb, C.E., Baltensperger, U., Worsnop, D.R., Dunlea, E.J., Huffman, J.A., Onasch, T.B., Alfarra, M.R., Williams, P.I., Bower, K., Kondo, Y., Schneider, J., Drewnick, F., Borrmann, S., Weimer, S., Demerjian, K., Salcedo, D., Cottrell, L., Griffin, R., Takami, A., Miyoshi, T., Hatakeyama, S., Shimono, A., Sun, J.Y., Zhang, Y.M., Dzepina, K., Kimmel, J.R., Sueper, D., Jayne, J.T., Herndon, S.C., Trimborn, A.M., Williams, L.R., Wood, E.C., Middlebrook, A.M., Kolb, C.E., Baltensperger, U., Worsnop, D.R., 2009. Evolution of Organic Aerosols in the Atmosphere. Science (80-.). 326, 1525–1529. https://doi.org/10.1126/science.1180353

Kanakidou, M., Seinfeld, J.H., Pandis, S.N., Barnes, I., Dentener, F.J., Facchini, M.C., Van Dingenen, R., Ervens, B., Nenes, A., Nielsen, C.J., Swietlicki, E., Putaud, J.P., Balkanski, Y., Fuzzi, S., Horth, J., Moortgat, G.K., Winterhalter, R., Myhre, C.E.L., Tsigaridis, K., Vignati, E., Stephanou, E.G., Wilson, J., 2005. Organic aerosol and global climate modelling: a review. Atmos. Chem. Phys. 5, 1053–1123. https://doi.org/10.5194/acp-5-1053-2005

Kroll, J.H., Seinfeld, J.H., 2008. Chemistry of secondary organic aerosol: Formation and evolution of low-volatility organics in the atmosphere. Atmos. Environ. 42, 3593–3624. https://doi.org/10.1016/j.atmosenv.2008.01.003

Lane, T.E., Donahue, N.M., Pandis, S.N., 2008. Effect of NOx on secondary organic aerosol concentrations. Environ. Sci. Technol. 42, 6022–6027. https://doi.org/10.1021/es703225a

Li, L., Tang, P., Cocker, D.R., 2015. Instantaneous nitric oxide effect on secondary organic aerosol formation from m-xylene photooxidation. Atmos. Environ. 119, 144–155. https://doi.org/10.1016/j.atmosenv.2015.08.010

Malloy, Q.G.J., Nakao, S., Qi, L., Austin, R., Stothers, C., Hagino, H., Cocker, D.R., 2009. Real-Time aerosol density determination utilizing a modified scanning mobility particle sizer aerosol particle mass analyzer system. Aerosol Sci. Technol. https://doi.org/10.1080/02786820902832960

Molteni, U., Bianchi, F., Klein, F., El Haddad, I., Frege, C., Rossi, M.J., Dommen, J., Baltensperger, U., 2018. Formation of highly oxygenated organic molecules from aromatic compounds. Atmos. Chem. Phys. 18, 1909–1921. https://doi.org/10.5194/acp-18-1909-2018

Myhre, G., Shindell, D., Bréon, F.-M.F.-M., Collins, W., Fuglestvedt, J.S., Huang, J., Koch, D., Lamarque, J.-F.J.-F., Lee, D., Mendoza, B., Nakajima, T., Robock, A., Stephens, G., Takemura, T., Zhan, H., Zhang, H., 2013. Anthropogenic and Natural Radiative Forcing, in: Intergovernmental Panel on Climate Change (Ed.), Climate Change 2013 - The Physical Science Basis. Cambridge University Press, Cambridge, pp. 659–740. https://doi.org/10.1017/CBO9781107415324.018

Na, K., Sawant, A.A., Song, C., Cocker, D.R., 2004. Primary and secondary carbonaceous species in the atmosphere of Western Riverside County, California. Atmos. Environ. https://doi.org/10.1016/j.atmosenv.2003.11.023

Nakao, S., Clark, C., Tang, P., Sato, K., Cocker, D., 2011. Secondary organic aerosol formation from phenolic compounds in the absence of NOx. Atmos. Chem. Phys. 11, 10649–10660. https://doi.org/10.5194/acp-11-10649-2011

Ng, N.L., Kroll, J.H., Chan, A.W.H., Chhabra, P.S., Flagan, R., Seinfeld, J.H., 2007. Secondary organic aerosol formation from m-xylene, toluene, and benzene. Atmos. Chem. Phys. 7, 3909–3922. https://doi.org/10.5194/acp-7-3909-2007

Odum, J.R., Hoffmann, T., Bowman, F., Collins, D., Flagan, R.C., Seinfeld, J.H., 1996. Gas/particle partitioning and secondary organic aerosol yields. Environ. Sci. Technol. 30, 2580–2585. https://doi.org/10.1021/es950943+

Odum, J.R., Jungkamp, T.P.W., Griffin, R.J., Forstner, H.J.L., Flagan, R.C., Seinfeld, J.H., Aromatics, 1997. Aromatics, Reformulated Gasoline, and Atmospheric Organic Aerosol Formation. Environ.Sci.Technol. 31, 1890. https://doi.org/10.1021/es960535l

Praske, E., Otkjær, R. V., Crounse, J.D., Hethcox, J.C., Stoltz, B.M., Kjaergaard, H.G., Wennberg, P.O., 2018. Atmospheric autoxidation is increasingly important in urban and suburban North America. Proc. Natl. Acad. Sci. U. S. A. 115, 64–69. https://doi.org/10.1073/pnas.1715540115

Presto, A.A., Donahue, N.M., 2006. Investigation of α-pinene + ozone secondary organic aerosol formation at low total aerosol mass. Environ. Sci. Technol. 40, 3536–3543. https://doi.org/10.1021/es052203z

Pye, H.O.T., Chan, A.W.H., Barkley, M.P., Seinfeld, J.H., 2010. Global modeling of organic aerosol: The importance of reactive nitrogen (NOx and NO3). Atmos. Chem. Phys. 10, 11261–11276. https://doi.org/10.5194/acp-10-11261-2010

Pye, H.O.T., D'Ambro, E.L., Lee, B.H., Schobesberger, S., Takeuchi, M., Zhao, Y., Lopez-Hilfiker, F., Liu, J., Shilling, J.E., Xing, J., Mathur, R., Middlebrook, A.M., Liao, J., Welti, A., Graus, M., Warneke, C., de Gouw, J.A., Holloway, J.S., Ryerson, T.B., Pollack, I.B., Thornton, J.A., 2019. Anthropogenic enhancements to production of highly oxygenated molecules from autoxidation. Proc. Natl. Acad. Sci. U. S. A. 116, 6641–6646. https://doi.org/10.1073/pnas.1810774116

Qi, L., Nakao, S., Tang, P., Cocker, D.R., 2010. Temperature effect on physical and chemical properties of secondary organic aerosol from m-xylene photooxidation. Atmos. Chem. Phys. https://doi.org/10.5194/acp-10-3847-2010

Schervish, M., Donahue, N.M., 2020. Peroxy radical chemistry and the volatility basis set. Atmos. Chem. Phys. 20, 1183–1199. https://doi.org/10.5194/acp-20-1183-2020

Song, C., Na, K., Cocker, D.R., 2005. Impact of the hydrocarbon to NOx ratio on secondary organic aerosol formation. Environ. Sci. Technol. 39, 3143–3149. https://doi.org/10.1021/es0493244

Song, C., Na, K., Warren, B., Malloy, Q., Cocker, D.R., 2007. Secondary organic aerosol formation from m-xylene in the absence of NOx. Environ. Sci. Technol. 41, 7409–7416. https://doi.org/10.1021/es070429r

Tsigaridis, K., Kanakidou, M., 2003. Global modelling of secondary organic aerosol in the troposphere: A sensitivity analysis. Atmos. Chem. Phys. Discuss. https://doi.org/10.5194/acpd-3-2879-2003

Wang, M., Chen, D., Xiao, M., Ye, Q., Stolzenburg, D., Hofbauer, V., Ye, P., Vogel, A.L., Mauldin, R.L., Amorim, A., Baccarini, A., Baumgartner, B., Brilke, S., Dada, L., Dias, A., Duplissy, J., Finkenzeller, H., Garmash, O., He, X.-C., Hoyle, C.R., Kim, C., Kvashnin, A., Lehtipalo, K., Fischer, L., Molteni, U., Petäjä, T., Pospisilova, V., Quéléver, L.L.J., Rissanen, M., Simon, M., Tauber, C., Tomé, A., Wagner, A.C., Weitz, L., Volkamer, R., Winkler, P.M., Kirkby, J., Worsnop, D.R.,

Kulmala, M., Baltensperger, U., Dommen, J., El-Haddad, I., Donahue, N.M., 2020. Photo-oxidation of Aromatic Hydrocarbons Produces Low-Volatility Organic Compounds. Environ. Sci. Technol. https://doi.org/10.1021/acs.est.0c02100

Wang, S., Wu, R., Berndt, T., Ehn, M., Wang, L., 2017. Formation of Highly Oxidized Radicals and Multifunctional Products from the Atmospheric Oxidation of Alkylbenzenes. Environ. Sci. Technol. 51, 8442–8449. https://doi.org/10.1021/acs.est.7b02374

Yan, C., Nie, W., Vogel, A.L., Dada, L., Lehtipalo, K., Stolzenburg, D., Wagner, R., Rissanen, M.P., Xiao, M., Ahonen, L., Fischer, L., Rose, C., Bianchi, F., Gordon, H., Simon, M., Heinritzi, M., Garmash, O., Roldin, P., Dias, A., Ye, P., Hofbauer, V., Amorim, A., Bauer, P.S., Bergen, A., Bernhammer, A.K., Breitenlechner, M., Brilke, S., Buchholz, A., Mazon, S.B., Canagaratna, M.R., Chen, X., Ding, A., Dommen, J., Draper, D.C., Duplissy, J., Frege, C., Heyn, C., Guida, R., Hakala, J., Heikkinen, L., Hoyle, C.R., Jokinen, T., Kangasluoma, J., Kirkby, J., Kontkanen, J., Kürten, A., Lawler, M.J., Mai, H., Mathot, S., Mauldin, R.L., Molteni, U., Nichman, L., Nieminen, T., Nowak, J., Ojdanic, A., Onnela, A., Pajunoja, A., Petäjä, T., Piel, F., Quéléver, L.L.J., Sarnela, N., Schallhart, S., Sengupta, K., Sipilä, M., Tomé, A., Tröstl, J., Väisänen, O., Wagner, A.C., Ylisirniö, A., Zha, Q., Baltensperger, U., Carslaw, K.S., Curtius, J., Flagan, R.C., Hansel, A., Riipinen, I., Smith, J.N., Virtanen, A., Winkler, P.M., Donahue, N.M., Kerminen, V.M., Kulmala, M., Ehn, M., Worsnop, D.R., 2020. Size-dependent influence of NOx on the growth rates of organic aerosol particles. Sci. Adv. 6, eaay4945. https://doi.org/10.1126/sciadv.aay4945

Zhao, H., Che, H., Zhang, X., Ma, Y., Wang, Yangfeng, Wang, H., Wang, Yaqiang, 2013. Characteristics of visibility and particulate matter (PM) in an urban area of Northeast China. Atmos. Pollut. Res. https://doi.org/10.5094/APR.2013.049

Chapter 5 : Conclusion & Future Work

Overall, this thesis has sought to improve the understanding of anthropogenic air pollutant in the aspects of primary marine emissions and secondary organic aerosol formation. Valuable field emission, chamber experiment and model simulation data, and chemical mechanism investigation as well as insights and suggestions on marine emission regulation, chamber experiment design and global modelling are provided.

This thesis conducted a comprehensive analysis on the air quality, health effects and climate change impacts of switching from diesel to NG by measuring and analysis the data of emissions from a marine vessel when operated at either fuel and engine load from idling to 90%. Particulate matter ($PM_{2.5}$, black carbon and organic carbon), criteria gases (NO_x, SO_x and CO), greenhouse gases (CO_2 and CH_4) and toxic gas (formaldehyde (HCHO)) were measured. The engine activity was calculated from the two-week routine activity of the vessel. The overall activity weighted emission factors showed that $PM_{2.5}$, BC, NO_x, CO_2 were reduced by about 93%, 97%, 92% and 18%, respectively. However, HCHO and CH_4 increased several-fold. A worst-case health risk assessment, when considering the $PM_{2.5}$ and HCHO emission when vessel was at berth, showed the diesel plume increased long-term health risk and the NG plume increased short-term health risk. A global warming potential (GWP) analysis was performed using the overall emission factors of CO_2, CH_4 and BC and it revealed that the average NG exhaust GWP was increased by 38%. A detailed engine load specific GWP analysis is provided. Mitigation strategies for further reducing pollutants from NG exhaust are discussed and showed potential for reducing short-term health risks and climate impacts.

SOA formation from aromatics was further investigated at different NO_x level to evaluate the SOA parameters that represent the two major chemical pathways, RO_2+NO and RO_2+HO_2. Three SOA yield curves were observed at very low NO_x condition. While the highest SOA yield curve is similar to the one currently being used in GEOS-Chem model for the higher mass loading scenario, the observed multiple curves indicates that other factors may affect SOA formation in very low NO_x condition and it is important to understand what drives the difference since very low NO_x conditions are typically used to simulate RO_2+HO_2 pathway in chamber. This work found that the *m*-xylene SOA strongly depends on the HO_2/RO_2 ratio at very low NO_x condition and suggested that a third pathway RO_2+RO_2 cannot be ignored at very low NO_x condition and it showed a lower SOA formation potential compared with RO_2+HO_2 pathway. Three sets VBS parameters were developed and applied with real-time chamber HO_2/RO_2 ratio to estimate SOA formed in chamber. It showed a significant improvement compared with the estimation using current GEOS-Chem *m*-xylene SOA parameters. In addition, GEOS-Chem simulation shows for the regions with lower HO_2/RO_2 ratio and higher aromatic emissions such as east coast of US and southeast of China, the *m*-xylene SOA can be over-predicted by 100%. Suggestions are provided that the initial VOC and H_2O_2 should be maintained same when designing a set of very low NO_x experiments in order to obtain a single SOA yield curve that represent the SOA formation from known contribution of RO_2+HO_2 and RO_2+RO_2 pathways.

The NO_x impacts on SOA formation were investigated the branching ratio (β) of RO_2+NO pathway. The highly variable β in traditional high NO_x chamber experiments

suggests that those experiments may not accurately represent RO_2+NO pathway. A novel approach was developed to maintain the β constantly at 1 to simulate RO_2+NO pathway without the significant interferences from other pathways. Two SOA yield curves were observed at β = 1 condition. While β was maintained at 1, the runs with higher NO/RO_2 ratio showed lower SOA yield. One possibility is that auto-oxidation may play an important role, and the presence of NO suppresses the extent of highly oxygenated RO_2 formation, leading to a lower SOA yield. However, further investigation is needed to verify this hypothesis.

The global surface β was modelled using GEOS-Chem. It showed that the β ranges from 0.2 to 0.8 around the world and stays in a relative constant level during daytime with sunlight. The intermediate β was firstly simulated constantly in chamber study and the *m*-xylene SOA formation at constant intermediate β was investigated. SOA formation decreased as β increased. However, the SOA yield at intermediate β did not agree with that estimated form the linear combination of products from RO_2+HO_2 and RO_2+NO pathways. This indicates that the current approach of estimating SOA yield directly from two pathway is not accurate enough and the SOA yield parameters representing the intermediate β condition need to be experimentally obtained.

This thesis provides valuable data and analysis on using natural gas on a single marine vessel and future work on evaluating the impacts on a global level is recommended. Other forms of NG have been discussed and implemented as a marine fuel, such as renewable NG or NG+H_2 mixture, due to their potential of less

environmental impacts. The on-board emissions of those fuels need to be investigated. The NO_x impacts SOA formation from *m*-xylene was investigated in this thesis using a novel approach of controlling β. The same approach should be applied to other aromatic compounds as well as biogenic SOA precursors in the future work.